Challenge Journal of STRUCTURAL MECHANICS

Vol.10 No.2 (2024)

auxetic buckling load building codes
compressive strength dynamic analysis
earthquake finite element method
girder bridge Jaya algorithm metaheuristic
algorithms modal analysis optimization
prestresing pushover analysis reinforced
concrete seismic design shallow foundations
smart concrete stability static analysis
steel structures structural dynamics
temperature effects thick plate wind

ISSN 2149-8024

TULPAR ACADEMIC PUBLISHING

Challenge Journal of Structural Mechanics

E-mail: *cjsmec@challengejournal.com*

Web page: *cjsmec.challengejournal.com*

Tulpar Academic Publishing
www.tulparpublishing.com

Challenge Journal of Structural Mechanics

CONTENTS

Research Articles

TULPAR ACADEMIC PUBLISHING

Challenge Journal of Structural Mechanics

Research Article

Ultimate drift ratio prediction of steel plate shear wall systems: a machine learning approach

Muhammed Gürbüz [a,*], İlker Kazaz [a]

[a] *Department of Civil Engineering, Erzurum Technical University, 25050 Erzurum, Türkiye*

ABSTRACT

Predicting the ultimate drift ratio of steel plate shear wall (SPSW) systems is important for ensuring the structural integrity and performance of these systems under lateral loads. In this study, machine learning models are developed for predicting the ultimate drift ratio based on various design parameters using data from previous research on SPSW systems. These design parameters include the panel aspect ratio, column flexibility parameter, axial load ratio, web plate thickness and stiffness of horizontal and vertical boundary elements. A range of machine learning models is considered, including Random Forest, Lasso, Gradient Boosting, XGBoost, Adaboost, Artificial Neural Network and a stacked regressor. The models are trained and evaluated using data from 292 different SPSW models, and their performance is compared based on the R-squared value, root mean squared error (RMSE), and evaluation time. The results of this study demonstrate the effectiveness of machine learning techniques for predicting the ultimate drift ratio of SPSW systems. The results of this study show that machine learning techniques effectively predict the ultimate drift ratio of SPSW systems. Among the models considered, the ANN model achieved the highest R^2 value, with a value of 0.94.

ARTICLE INFO

Article history:
Received 13 September 2023
Revised 2 November 2023
Accepted 25 November 2023

Keywords:
Steel plate shear walls
Finite element analysis
Machine learning
Artificial neural network
Stacked regressor

1. Introduction

Structural engineering involves the analysis and design of load-bearing structures that can be particularly challenging in complex structural systems under extreme actions exhibiting highly nonlinear behavior. Traditional structural analysis and design methods involve the study and application of mathematical and physical principles to evaluate the performance and behavior of load-bearing structures. These methods are used to predict the response of structures to various types of loads, such as gravity, wind, and earthquakes, and to design safe and efficient structures. However, these methods may require a time-consuming calibration process to accurately predict the behavior of systems under extreme loading conditions, particularly for those that exhibit highly nonlinear behavior. Additionally, the complexity and uncertainty in these methods can make them challenging to implement in practice, particularly for complex structural systems. However, machine learning (ML) allows for the creation of computer models that can learn and identify patterns from a set of data, potentially offering more efficient and effective solutions for structural engineering problems.

Artificial intelligence (AI) is a computer science field aiming to replicate human cognition and reasoning capabilities through symbol manipulation and structured knowledge bases. Machine learning (ML) is a subfield of AI that focuses on teaching computers to make predictions from data and algorithms without being explicitly programmed. ML algorithms can be classified into unsupervised and supervised learning. Unsupervised learning is a type of ML in which an algorithm is trained on an unlabeled dataset. It is used to discover patterns and relationships in the data without prior knowledge of the output. Clustering, a subcategory of unsupervised learning, involves grouping data points into clusters based on similarity. Dimensionality reduction, another subcate-

* *Corresponding author*. E-mail address: muhammed.gurbuz@erzurum.edu.tr (M. Gürbüz)
ISSN: 2149-8024 / DOI: https://doi.org/10.20528/cjsmec.2024.02.001

gory of unsupervised learning, involves reducing the number of variables in a dataset while preserving the important information. These techniques can be useful in structural engineering tasks such as identifying similar structures or simplifying complex models. Supervised learning is a type of ML in which an algorithm is trained on a labelled dataset. It is commonly used for regression and classification problems in which the output is continuous or discrete. Regression analysis, a subcategory of supervised learning, involves predicting a continuous output based on one or more input variables. It is widely used in various fields, including structural engineering, to make predictions about structural behavior, such as strength and stiffness, or to identify relationships between variables.

In structural engineering, various ML algorithms have been applied to multiple tasks, including predicting building responses to seismic loads, analyzing structural behavior under extreme actions, and optimizing structural design parameters. These algorithms include neural networks (NN), which use artificial neural connections to model relationships between input and output data; decision trees (DT), which use a tree-like model of decisions to identify the most appropriate course of action; regression analysis (RA), which is used to predict continuous values based on a given set of input variables; support vector machines (SVM), which classify data by finding the hyperplane that maximally separates different classes; random forests (RF), which are ensembles of decision trees that use random sampling to improve the prediction accuracy of the model; and boosting algorithms (BA), which combine multiple weak models to create a more accurate and robust model.

Many pioneering works in structural engineering, including structural analysis and design, have effectively employed the machine learning technique. Adeli and Yeh (1989) completed one of the first examples of structural design work on beam design. Hajela and Berke (1991) used neural networks to study force-displacement relationships in static structural analysis in the following years. They applied two different network algorithms to the problem and examined the effects of parameters such as learning rate on the results. Xu et al. (1992) created neural network-based methods for autonomously detecting structural damage caused by a variety of variables such as routine operations, accidents, deterioration, or natural events. They concluded that the use of the neural network is promising for structural damage assessment.

Large experimental or numerical datasets are often required to confirm machine learning's performance in estimating the behavior of structural systems. One of the reasons why machine learning is becoming more popular in structural engineering is because the needed datasets are considerably larger than in the past. The survey by Thai (2022) provides a comprehensive review of the growing applications of machine learning algorithms. The research investigates how machine learning can be applied to ascertain the mechanical characteristics and mix design of concrete. It delves into examining both individual elements and entire structures constructed from steel, concrete, and composite materials. Sun et al. (2021) review the application of machine learning in structural design and performance assessment. The paper also discusses the challenges and future opportunities for integrating machine learning into structural engineering practice. Xie et al. (2020) studied the progress and challenges of implementing machine learning in earthquake engineering. The review encompasses the utilization of machine learning across four primary domains system identification, seismic analysis, earthquake engineering and damage detection, seismic fragility assessment, and structural control for earthquake mitigation. The study also discusses the challenges and future research needs for machine learning in earthquake engineering, including embracing new data sharing and sensor technologies, implementing advanced machine learning techniques, and developing physics-guided machine learning models.

There are also studies to predict structural drift limits using machine learning methods. Inel (2007) used experimental data from 237 rectangular columns to create an artificial neural network (ANN) model and compared the ultimate displacement estimates from the model to existing semi-empirical and empirical models. The results showed that the ANN model performed well and proved the feasibility of using ANN models for estimating the deformation of RC columns. Darain et al. (2015) investigated the deflection behavior of strengthened RC beams using adaptive neuro-fuzzy prediction. According to the study, the projected deflection and crack width nearly match the outcomes of the experiments, confirming the accuracy of the model. Another study by Kalman et al. (2013) evaluated the earthquake performance of RC frames with masonry wall infill using NN (neural network). The study results showed that neural networks trained on the database could be utilized to estimate the seismic behavior of framed-masonry structural elements. Luo and Paal (2019) proposed a local machine-learning model for predicting the drift capacity of reinforced concrete (RC) columns. The model was trained and tested using a database comprising 160 circular reinforced concrete columns. It was then contrasted with well-known existing global and local learning methods as well as a conventional empirical equation. The outcomes indicated that the suggested model is a prospective method for improving the predicting of drift capacity. Nguyen et al. (2021) studied the seismic drift behavior of planar steel moment frames using ANN and Extreme Gradient Boosting (XGboost). The authors stated that the XGboost algorithm better predicted the responses of steel frames than the ANN model. The authors also designed a user interface to predict steel frame drift response using XGboost.

In this study, the performance of different machine learning-based regression models in predicting the drift capacity of steel plate shear walls (SPSW) is evaluated using data from a previous study (Gürbüz and Kazaz 2022a). SPSW systems are widely used in the construction of high-rise buildings and other structures subjected to lateral loads such as earthquakes and wind. Steel web shear walls have a more sophisticated system mechanism than conventional steel frames. A steel web plate in

such systems transfers additional loads on the horizontal and vertical boundary members (beams and columns). The lower and higher-level steel panels transmit opposing loads to the beam members between adjacent floors. As a result, the top anchor beam experiences an unbalanced load. Moreover, the steel panel imposes an inward pull on the columns, possibly leading to unexpected column buckling. Steel panel-induced loads have resulted in various steel frame collapse mechanisms. These collapse processes under monotonic and cyclic loading cases were investigated by Gürbüz and Kazaz (2022a, 2022b). The performance of these systems under lateral loads depends on various design parameters, including the panel aspect ratio, column flexibility parameter, axial load ratio, web plate thickness, and more. Previously, 292 different SPSW models were designed and analyzed by Gürbüz and Kazaz (2022a) using the finite element method to explore the interactive effect of various design parameters on the drift capacity and shear force distribution of SPSW systems. Accurate prediction of the ultimate drift ratio of SPSW systems is essential for ensuring the safety and reliability of these structures. Various past studies have investigated the interactive effect of design parameters on the drift capacity and shear force distribution of SPSW systems using analytical and experimental methods. However, these studies often examined only a few design parameters at a time, making it difficult to fully understand the complex interaction of all the parameters on the behavior of SPSW systems. The design parameters included panel aspect ratio, column flexibility factor (a measure of the stiffness of the columns), axial load ratio, web plate thickness, stiffness of horizontal and vertical boundary elements. The ultimate drift ratio of each model was used as the response variable in the machine-learning models. The ultimate drift ratio is a measure of the maximum displacement of the structure under lateral load and is an essential consideration in the design of SPSW systems as it affects the overall stability and performance of the structure.

This study aims to fill the gap in the literature by developing machine learning model algorithms to predict the ultimate drift ratio of SPSW systems based on the design parameters. Many machine learning models, including Random Forest, Lasso, Gradient Boosting, XGBoost, Adaboost, and a stacked regressor, are considered. In addition, the performance of an artificial neural network (ANN) model is also investigated. ANNs are a type of machine learning algorithm that mimics the structure and function of the human brain and can be used for both regression and classification tasks. By comparing the performance of these different models, the researchers can determine the most effective approach for predicting the behavior of these types of structures.

The details of the algorithms used in this study are given in the following sections. The performance of these models is compared in terms of the R^2 value, root-mean-squared error (RMSE), and evaluation time. The results of this study provide a comprehensive understanding of the behavior of SPSW systems and may be useful for predicting the ultimate drift ratio of these systems in the design process.

2. Data

Gürbüz and Kazaz (2022a) used a verified finite element modeling technique to investigate the behavior of the 3-story and moment-framed steel plate shear walls. 292 models were created by changing design parameters within specific ranges and analyzed under monotonic loading using the finite element analysis software ANSYS (2016).

To create variations of SPSW models, plate thickness, panel aspect ratio, stiffness of boundary elements, and axial load ratio on vertical boundary element (VBE) were considered. The models contained both geometric and material non-linearities. Fig. 1 shows a typical three-story SPSW model that illustrates and summarizes the study's main parameters. In the model, to increase the resistance of the top beam against the bending action of internal steel plate forces, an additional beam was attached to the top beam, and the beams were assumed to be constrained (share the same nodes) along the adjoining beam flanges as shown in Fig. 1(a). The horizontal load was applied at the top left nodes of the models as shown in Fig. 1(b).

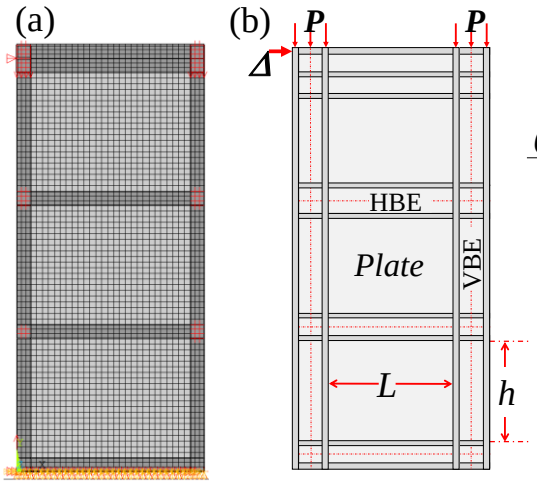

h (mm)	L (mm)	t_w (mm)	I_c / I_b	P / P_{cr}
3000	2000	2	1	0.1
	3000	3	2	0.2
	4000	4	3	0.3
	5000	5	4	
	6000	6	5	

Fig. 1. (a) A representative finite element model of SPSWs used in the study; (b) Typical steel plate shear wall configuration.

All story-level intersections of beams and columns were defined as the locations for lateral support. At all story levels, out-of-plane displacements of the nodes in intersection regions were constrained.

The chosen panel lengths are 2000, 3000, 4000, 5000, and 6000 mm, and the steel panel height h_s is constant at 3000 mm in all variants. In this manner, plate aspect ratios - the ratio of panel length to height L/h - between 0.67 and 2 were considered. As previously observed, narrow steel plate shear walls functioned adequately and displayed ductile hysteric behavior, which can be compared to those with larger aspect ratios (Li and Tsai 2008). Thus, models with a low panel aspect ratio of 0.67 were also examined. The chosen plate thicknesses t_w are 3, 4, 5, and 6.

The SPSW behavior was investigated using parameters plate thickness, column flexibility parameter (ω_i), the moment of inertia ratio of beam and column (I_c/I_b), panel aspect ratio(L/h), axial load ratio on columns(P/P_{cr}), beam flange width–beam height ratio (b/h_b) the beam flange width to beam height ratio (b_f/h_b), the beam flange width-to-thickness ratio ($b_f/2t_f$), beam web area and column web area.

Seven different types of failure modes were identified for SPSWs. These failure modes were studied in terms of variables, including the column flexibility factor, plate thickness, and L/h in general. Fig. 2 displays the identified SPSW failure modes and a representative force-drift curve for each group. Each group was carefully analyzed in the relevant research, and an investigation on the parameters that lead to failure and the failure sequence was conducted.

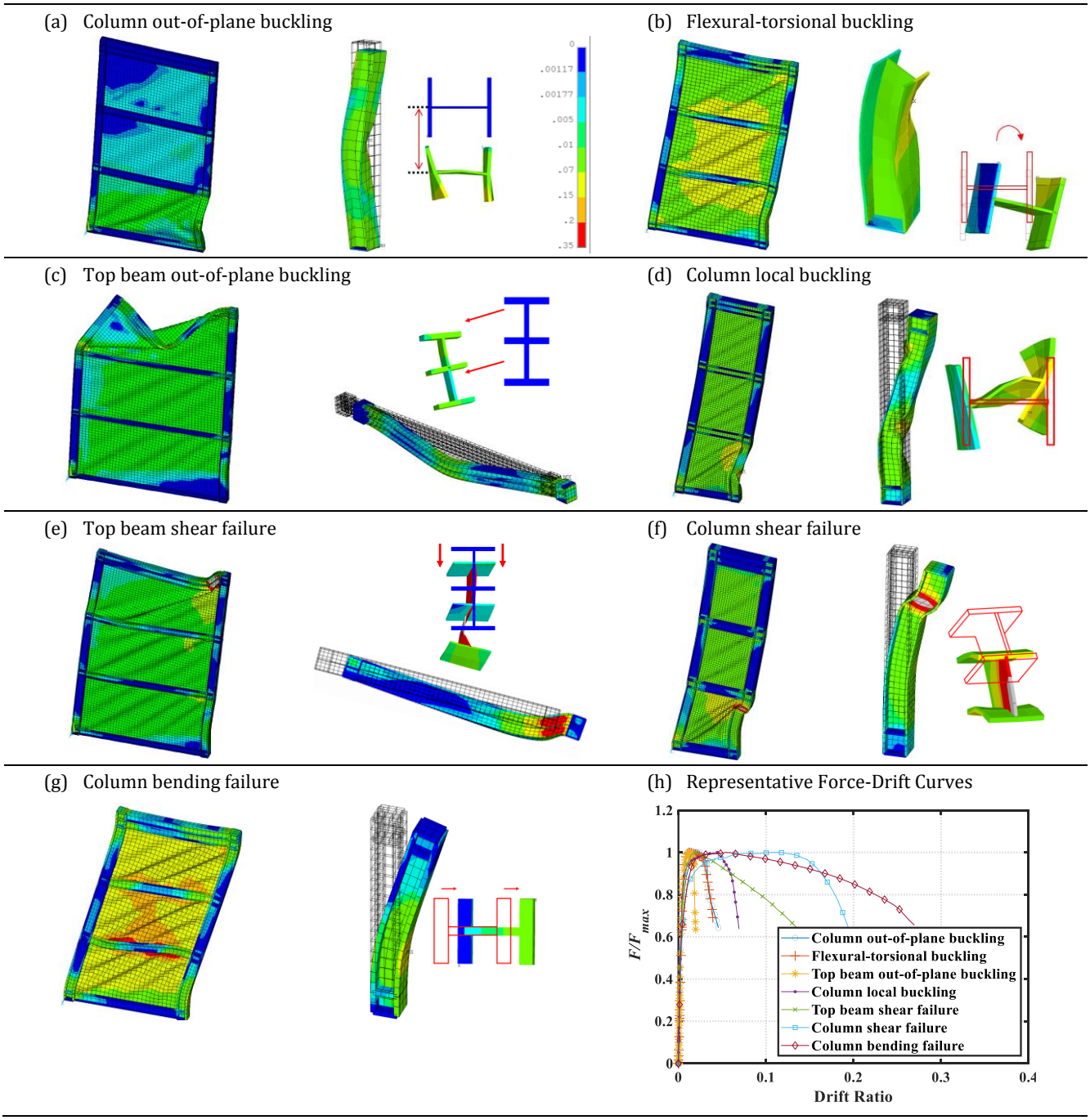

Fig. 2. Different failure modes of the SPSW models and representative Force-Drift ratio curves of each failure group.

The definition of the ultimate drift ratio (DR_u) of SPSWs varies for different models. When the force-drift curves are assessed, some groups show no noticeable drop, while others have a system that clearly fails as displayed in Fig. 3. Therefore, it could be claimed that this difference in how the ultimate drift ratio is defined is necessary.

The point where the base story shear force drops to 85% of its maximum value on the load-displacement curve is the ultimate drift ratio for the group that failure is observable (Fig. 3(a)). In a different group that is represented by the force-drift curve in Fig. 3(b), it can be seen that the system can still sustain the load at 85% of its maximal strength, but after a particular drift, it loses its ability to resist force. The ultimate drift ratio for these models is referred to as the location of the break on the force-displacement curve. The ultimate drift limit, however, is taken as the drift level corresponding to 50% of the peak shear force, such as in high axial load instances where the force-displacement curve steadily decreases after peak force (Fig. 3(c)).

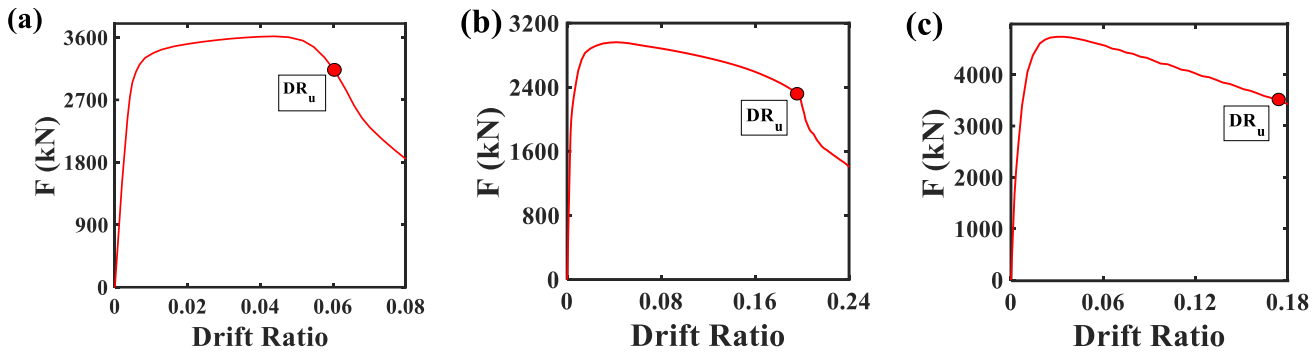

Fig. 3. Different definitions of the ultimate drift ratio in Gürbüz and Kazaz (2022a).

In ensuring data quality and preparing the dataset for model training, several crucial data preprocessing steps were employed. This included an extensive data cleaning process to handle outliers and anomalies, normalization techniques to standardize feature scales, and imputation methods to address missing values.

3. Method

The dataset employed in this study is composed of numerical data that simulates the behavior of steel plate shear walls with moment frames under extreme loading conditions. This dataset was created specifically to explore the performance of the SPSW structures under these high-loading conditions. By providing the data to feed the machine learning models, this study also investigates the parameter effects on the overall behavior of the structures.

The study employed a Stacking Regressor, which combines multiple base models to improve the prediction accuracy of the drift behavior of Steel Plate Shear Walls (SPSWs) under monotonic loading. A variety of base models were defined, including Gradient Boosting, Lasso, Random Forest, XGBoost, ANN and AdaBoost was selected due to their capability to deal with nonlinear and complex data and used as input to the Stacking Regressor. This ensemble approach aims to leverage the strengths of each individual model to achieve improved performance.

The choice of model hyperparameters is a critical issue in machine learning models. When creating models, different values are given to parameters like the learning rate and the number of estimators, which directly impact the prediction accuracy of the models. These parameters can be chosen randomly or optimized using different methods. One of these methods is the grid search technique finding the ideal set of hyperparameters for a particular model. To achieve this, a model is trained using various combinations of hyperparameters, and its effectiveness is assessed using test data. The ideal setting is then determined by the combination of hyperparameters that produces the best performance. Many supervised machine learning tasks use grid search. The grid search can be performed using sklearn's GridSearchCV class. This section provides information about each machine learning algorithm used in this study.

3.1. AdaBoost

The AdaBoost algorithm was employed as one of the base models in the stacking regressor. AdaBoost, which stands for Adaptive Boosting, is a type of ensemble method that combines a number of weak learners to form a strong learner. Freund and Schapire (1997) introduced it in 1997 and since then has been widely used in various applications. The basic idea behind AdaBoost is to iteratively improve the performance of a weak model by giving more weight to the misclassified examples in the training data.

In this study, the AdaBoost algorithm is implemented using the Sklearn library in Python. Scikit-learn (Sklearn) is an open-source machine learning library for the Python programming language. It provides a wide range of tools and techniques for machine learning and statistical modeling, including classification, regression, clustering, and dimensionality reduction ("scikit-learn: machine learning in Python - scikit-learn 1.2.0 documentation" n.d.). The AdaBoostRegressor class is used to create the model, which takes several parameters such as the number of estimators, the learning rate, and the random state. The number of estimators refers to the num-

ber of weak learners to be used, the learning rate determines the weight of each estimator in the final prediction, and the random state is used to initialize the random number generator for reproducibility.

The number of estimators is set to 200, 400, and 600, the learning rate is set to 0.001, 0.005, and 0.01, and the random state is set to 0 for the grid search. Finally, the learning rate is set to 0.01 and the number of estimators is 600.

3.2. Gradient Boosting

Gradient Boosting is an ensemble learning technique that is an iterative method to optimize a differentiable loss function using the gradient descent algorithm. The idea behind gradient boosting is to train a set of weak models (such as decision trees) and combine them to form a stronger model. Each tree grown during the iteration fits the negative gradient of the loss function (or residual) concerning the current ensemble predictions. After each iteration, the negative gradient is computed as the difference between the true target values and the current ensemble predictions. A typical loss function used in gradient boosting is mean squared error (MSE) for regression problems is given as,

$$MSE = \frac{1}{n}\sum(y_i - \hat{y}_i)^2 \quad (1)$$

where y_i is the i^{th} observed value, $\hat{y}_i$ is the predicted value and n is the number of observations.

In this study, the Gradient Boosting algorithm is implemented using the sklearn library in Python. The GradientBoostingRegressor class is used to create the model, which takes several parameters such as learning rate, loss function, maximum depth of the trees, the minimum number of samples required to split a node, and the number of estimators. Using the GridSearchCV class, the learning rate is set to 0.01. The loss function is set to 'ls' (least squares), which minimizes the mean squared error between the predicted and actual response values. The maximum depth of the trees is 6, the minimum samples required to split a node is 4, and the number of estimators is 600.

3.3. Random Forest

Random forest is a popular algorithm for many machine-learning tasks, including classification and regression. The idea behind it is to construct multiple decision trees and combine their predictions with improving the overall performance of the model. Each tree in a random forest is built using a different subset of the training data and a different subset of the features. The final prediction is made by averaging or voting the predictions of all the trees in the forest. Fig. 4 depicts a schematic of the Random Forest working algorithm.

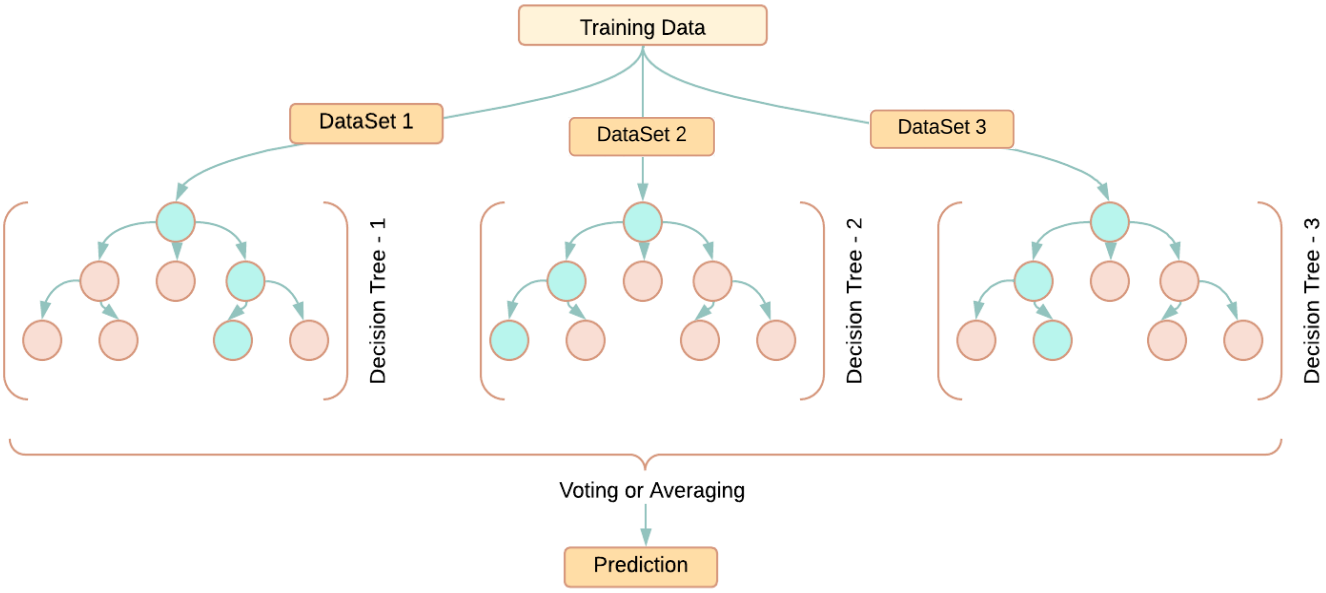

Fig. 4. Random Forest algorithm.

The random forest algorithm was first introduced by Breiman (2001). The idea of building a model using multiple decision trees was motivated by the problem of high variance in individual decision trees, which often resulted in poor generalization performance. By averaging the predictions of multiple trees, random forest is able to reduce the variance and improve the overall performance of the model.

In terms of implementation, one can use the RandomForestClassifier and RandomForestRegressor classes from the scikit-learn library to train and evaluate a random forest model. These classes provide a simple and easy-to-use interface for training and evaluating random forest models and provide a variety of parameters for fine-tuning the model performance. Grid search and cross-validation techniques can also be used to tune the parameters of the random forest model.

The RandomForestRegressor class is used to create the model, which takes several parameters such as the maximum depth of the trees, the minimum number of

samples required to split a node, the number of estimators and the random state. Using the GridSearchCV class, the maximum depth of the trees is set to 8, the minimum number of samples required to split a node is set to 4, the number of estimators is set to 400 and the random state is set to 0. These hyperparameters are used to initialize the Random Forest model, which is then trained on the provided dataset to make predictions. It is important to note that these values are not necessarily optimal for every dataset and problem and that tuning these hyperparameters is crucial to achieve good performance.

3.4. XGBoost

XGBoost, also known as eXtreme Gradient Boosting, is a powerful gradient-boosting algorithm that is specifically designed to be efficient and fast. It was first introduced by Chen and Guestrin (2016). It is an optimized implementation of the gradient boosting framework, which sequentially combines decision trees to improve the overall accuracy of the model. XGBoost is a popular algorithm in machine learning competitions due to its ability to handle large and high-dimensional data and to be robust in handling missing data.

The algorithm works by fitting an ensemble of decision trees, with each new tree trained to correct the errors made by the previous one. It uses several regularization and optimization techniques to improve the speed and performance of the algorithm. Chen and Guestrin (2016) stated that it is ten times faster than existing solutions. The output variable is given in the following equation:

$$\hat{y}_i = \sum_{k=1}^{k} f_k(x_i), f_k \in \mathrm{F} \tag{2}$$

where, $\hat{y}$ and x_i are the output and input variables, K is the number of trees, f is the score function and F is the possible regression or classification tree set. The regularized objective function is:

$$L(\emptyset) = \sum_i l(\hat{y}_i, y_i) + \sum_k \Omega(f_k) \tag{3}$$

where, l is a differentiable convex loss function and the second term Ω penalizes the complexity of the model.

The XGBoost algorithm is implemented using the XGBRegressor class of the XGBoost library. It takes several parameters, such as the learning rate, maximum depth of the trees, and the number of estimators. Using the GridSearchCV class, the learning rate is set to 0.01, the maximum depth of the trees is 8, and the number of estimators is 600. These hyperparameters are used to initialize the XGBoost model, which is then trained on the provided dataset to make predictions.

3.5. Lasso Regression

The Lasso algorithm, which stands for Least Absolute Shrinkage and Selection Operator, was first introduced by Robert Tibshirani (1996). Apart from the algorithms given above, Lasso is a linear model that uses L1 regularization, which is a technique that constrains the sum of the absolute values of the coefficients. The Lasso algorithm was developed as an extension of the least squares method, a commonly used technique for fitting a linear model to a dataset. However, unlike least square, which uses L2 regularization, Lasso uses L1 regularization, resulting in sparse solutions where some of the coefficients are zero. This makes Lasso particularly useful for feature selection, as it can automatically select a subset of the most important features for the model.

The Lasso algorithm has been widely used in various fields such as statistics, machine learning, and applied sciences. It is advantageous in high-dimensional settings where the number of features is larger than the number of samples. Since its introduction, many extensions and variations of the Lasso algorithm have been developed, such as the elastic net, which is a combination of L1 and L2 regularization, and the adaptive Lasso, which adapts the L1 penalty to the data.

In this study, the alpha value is set to 0.001, which controls the regularization strength. A larger value will make the model more conservative, while a smaller value will make the model more flexible and prone to overfitting.

3.6. Stacked Regressor

The StackingRegressor class can combine the predictions of multiple base estimators and use them for training a higher-level meta-model. The base estimators are trained in parallel, and their predictions are combined using a blending process, which can be specified through the blender parameter. The meta-model is then trained on the blended predictions of the base estimators.

In this case, the StackingRegressor object is a model that combines the predictions of the Gradient Boosting model, Lasso model, Random Forest Model, and XGBoost model using the RidgeCV model as the meta-model. This can potentially improve the performance of the resulting model compared to using any of the base estimators alone.

The stacked regressor model, however, came after to the XGBoost model in this investigation. The stacked regressor model's R^2 value is 0.79, and the evaluation process took 11.62 sec in total. Among all the models, this evaluation period is the longest. This is a predictable outcome, given that using a new meta-model and combining additional regression models takes some time. However, the stacked regressor results being less accurate than the XGBoost model is generally not expected. It is worth considering whether the ensemble model is appropriate for the data. Ensemble models can be powerful, but they may not always be the best choice for a particular dataset. The chosen parameters might have high relations to each other, resulting in the ensemble model being unable to capture the full range of prediction patterns and performing worse than the individual models. A correlation investigation was conducted and the results are presented in the results section.

3.7. Artificial Neural Network

Artificial neural networks (ANNs) are a class of machine learning models that are inspired by the structure and function of biological neural networks. The ANN

consists of numerous layers of neurons, which process and transmit information. ANNs are capable of learning from data and can be used for a variety of tasks. The working mechanism of an ANN involves the processing of input data through the various neuron layers, each of which applies a set of weights and biases to the input and produces an output. An example of the ANN algorithm is given in Fig. 5(a). The output of one layer serves as the input to the next layer. The weights and biases are adjusted during the training process to optimize the performance of the network

The ANN model is created in this study using the Neural Network Toolbox in MATLAB ("Deep Learning Toolbox - MATLAB" n.d.). The given code creates a loop that runs 60 times. In each loop iteration, a neural network with a different number of neurons in the hidden layer is created and trained using the fitnet and train functions. The training ratio is set to 70%. The validation ratio is 20% while the test ratio is 10%. It then sets the proportion of data for training, validation and testing and trains the network using the train data. Next, the code calculates the Root Mean Squared Error (RMSE) for the training and validation sets for each hidden layer size. After all, the hidden layer sizes have been trained and the errors have been calculated, the code used in this study finds the index of the minimum RMSE value on the validation set and prints the optimal number of neurons in the hidden layer. The code then retrains the network with an optimal number of neurons with a training ratio of 70%, a validation ratio of 20% and a testing ratio of 10%. Then the code calculates the RMSE and relative RMSE of the training and validation dataset. An image created by the MATLAB Neural Network tool that shows the number of inputs, the number of optimal hidden layers and the output is given in Fig. 5(b).

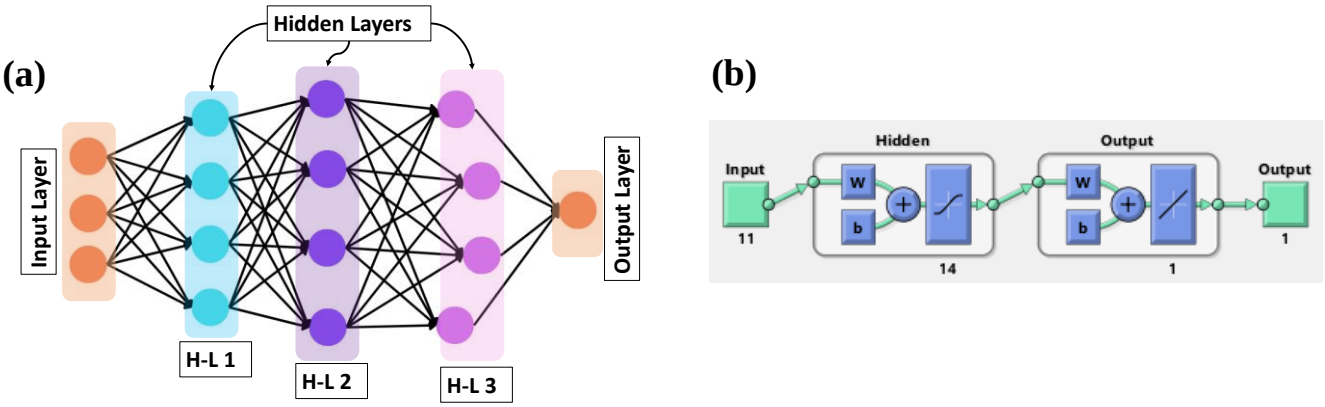

Fig. 5. (a) ANN architecture; (b) An architecture created by MATLAB Neural Network tool.

In each run, the optimal number of neurons takes a different value. The reason is that the hidden layer changes in each run since the training and validation sets are selected randomly at the beginning of each run. This means that the data on which the ANN is trained and evaluated will be different in each run, and therefore the optimal number of neurons in the hidden layer that leads to the best performance on that specific data will also be different. The study aims to have an average performance on the ANN model.

In addressing the concern of overfitting in this study, several strategies were implemented. We applied regularization techniques, including L1 regularization in Lasso Regression and leveraging regularization parameters in the XGBoost algorithm, aiming to control model complexity. Cross-validation, particularly k-fold cross-validation, played a pivotal role during model training, ensuring robustness by evaluating models across various data partitions. The optimization of hyperparameters through techniques like GridSearchCV and the utilization of ensemble methods, such as the StackedRegressor, were employed to strike a balance between model complexity and predictive performance. These concerted efforts were undertaken to mitigate overfitting risks while maintaining the models' accuracy and generalizability.

4. Results

A total of seven different models were trained and evaluated using the database of steel plate shear walls (SPSW). These models included Random Forest, Lasso, Gradient Boosting, XGBoost, AdaBoost, a Stacking Regressor, and an Artificial Neural Network (ANN). The performance of each model was assessed using various evaluation metrics, including mean squared error (MSE), R-squared score, and evaluation time. The following section presents a detailed comparison of the performance of each of these models in terms of their prediction accuracy and computational efficiency.

Regarding the R-squared score, the Artificial Neural Network (ANN) model outperformed all other models with an R-squared score of 0.918 on the validation dataset. The second-best performer was the XGBoost model, which had an R-squared score of 0.83. The Gradient Boosting model had an R-squared score of 0.701, followed by the Stacking Regressor with an R-squared score of 0.791. The Random Forest model had an R-squared score of 0.753, while the AdaBoost model had an R-squared score of 0.633. The lowest R-squared score was achieved by the Lasso model, with an R-squared score of 0.418. Overall, it can be seen that the ANN model had the highest prediction accuracy, followed by the XGBoost model. It is

also worth noting that the ANN model had the highest R-squared score for all data, training, validation and test set. The results are presented in Fig. 6. The results of the best-performed model are investigated separately in Fig. 7.

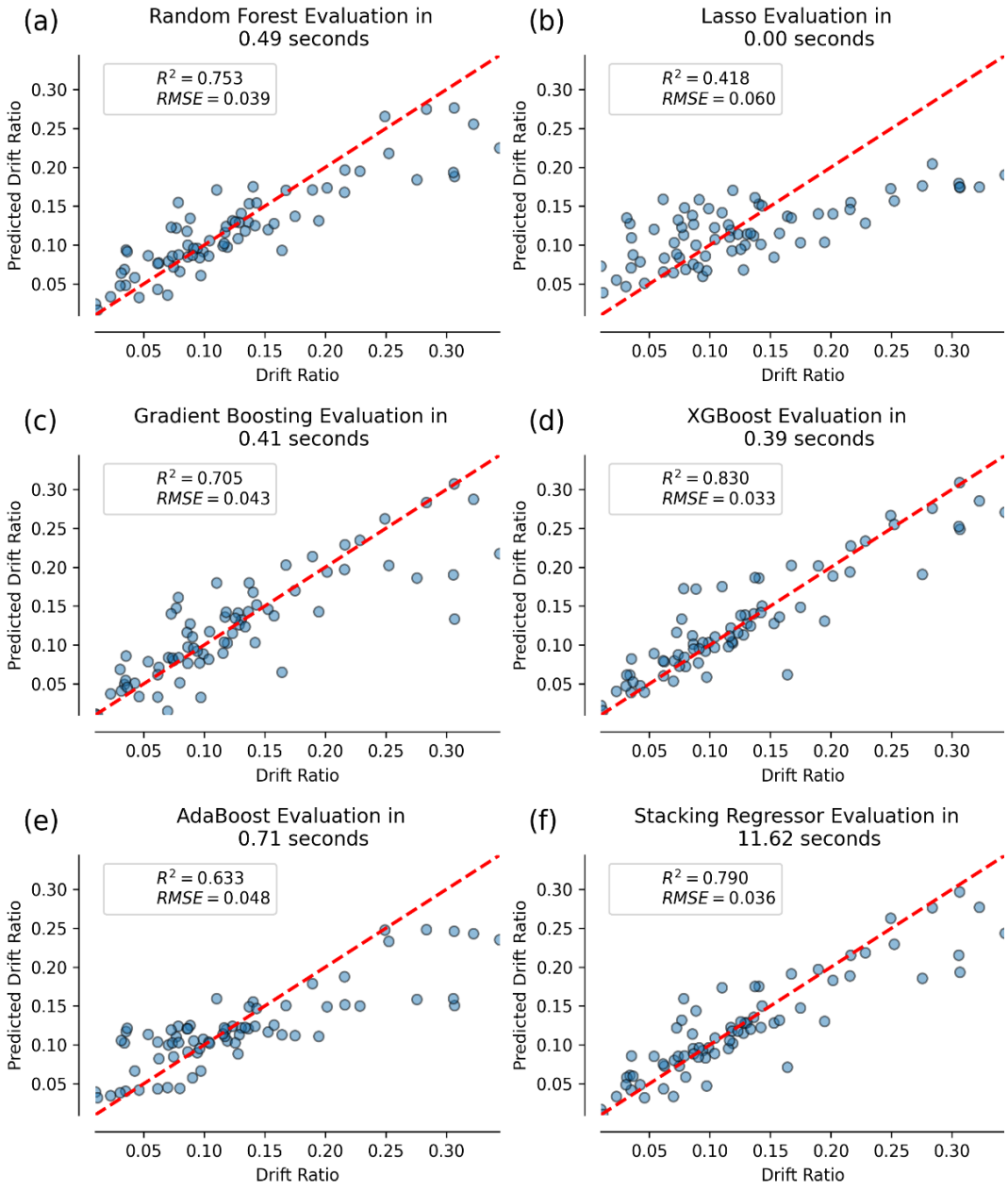

Fig. 6. Comparison of different models.

In terms of evaluation time, the best models were Lasso and XGBoost, with evaluation times of 0.01 and 0.4 seconds, respectively. These models could predict the ultimate drift ratio of SPSW systems with relatively low evaluation times. The Random Forest model, which had an evaluation time of 0.52 seconds, also performed relatively well in terms of evaluation time. On the other hand, the Gradient Boosting, Adaboost and Stacking regressor models had longer evaluation times of 0.43, 0.72 and 11.98 seconds, respectively. The Artificial Neural Network (ANN) model had one of the longest evaluation times of all the models, with an average evaluation time of 6.7 seconds. This is because the ANN model is a complex algorithm that requires more computational resources to train and evaluate. In addition, the loop in the script tests 1 to 60 hidden layers. However, the ANN model has the highest R-squared score of 0.9469 among the models. The evaluation time should be very low with a specific hidden layer size. It should be noted that the evaluation time of a model is an essential consideration in practice, as it can have a significant impact on the feasibility and cost of using the model in real-world applications.

When Fig. 7(a) is examined, the R-squared value of the ANN model of the training data was approximately 0.97, which is relatively high. Such a high R-squared number may indicate an overfitting issue. When an Artificial Neural Network (ANN) is overfitted, it underperforms on unknown, new data because the model was trained too well on the training data. Overfitting may occur due to noise, the small size of the training set, and the

complexity of the classifiers (Ying 2019). When a model has more parameters than training data, overfitting can happen, which prevents the model from generalizing to new data. However, the R^2 value of the validation data is 0.92 and the test data is 0.85, as shown in Figs. 7(b) and 7(c). These are also high R^2 values when viewed within the context of regression analysis, yet they are acceptable levels. A very high R^2 value of 0.95 was found in the regression analysis conducted on the entire data set in Fig. 7(c), similar to the other results.

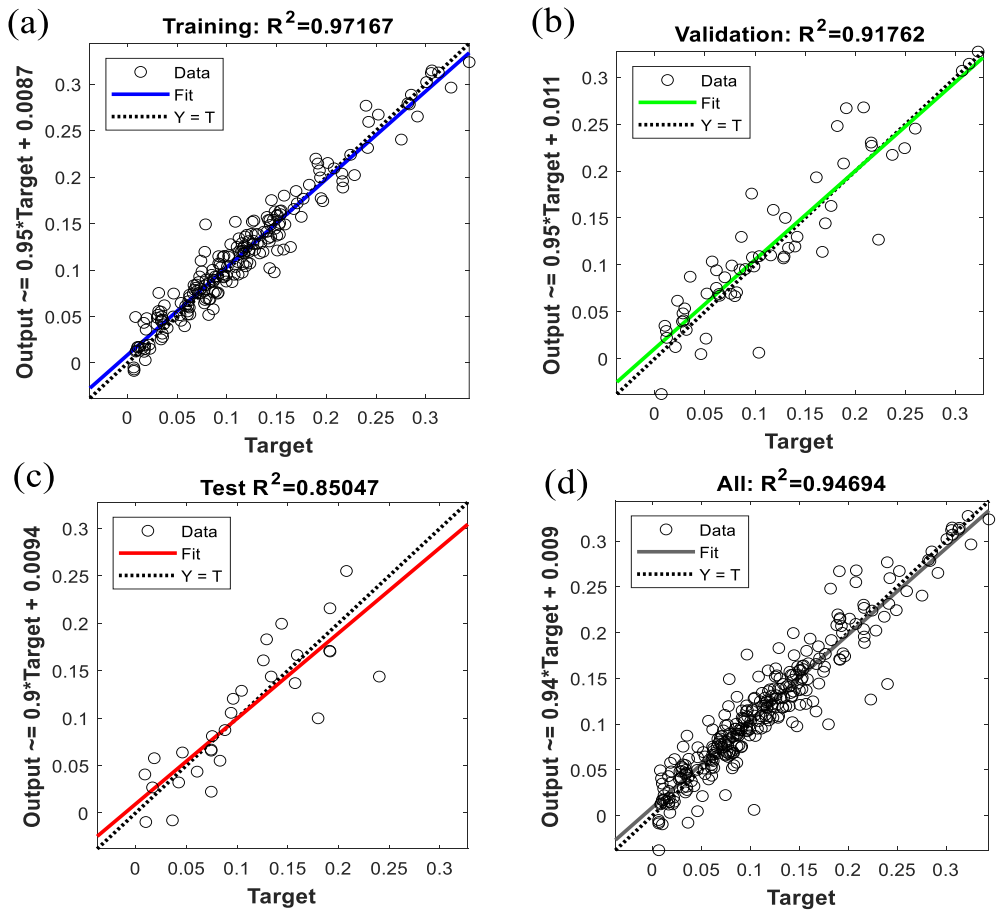

Fig. 7. ANN results: (a) Training data (70% of all data); (b) Validation data (20% of all data); (c) Test data (10% of all data); (d) All data predicted and target values.

Considering all these findings, XGBoost is among the most practical models regarding evaluation time and R-squared outcomes. Except for ANN, only XGBoost has a better R-squared value than the stacked regressor. The influence of the parameters on the results was investigated using various techniques through the XGboost model results.

The relative importance of each feature in a dataset can be evaluated using the machine learning technique known as feature importance analysis. First, a feature importance analysis was conducted and the results are presented in Fig. 8. In order to improve the performance of the model or to comprehend the underlying relationships in the data, it helps to identify the attributes that have the most influence on the model's outcome. In feature importance analysis, a tree-based model, such as XGBoost, was utilized to gauge the significance of various parameters in predicting the ultimate drift ratio of steel plate shear wall (SPSW) systems. The feature importance was calculated primarily through the evaluation of the Gini impurity or related metrics within these models. Higher feature importance scores indicate a stronger influence of the respective parameters on the predictive accuracy of the models.

When Fig. 8 is analyzed, it is obvious that ω_i, t_w, and P/P_{cr} are the most critical factors in the drift behavior of SPSW systems. According to the findings of the former study (Gürbüz and Kazaz 2022a, 2022b), these parameters directly impact the behavior of the system. Fig. 9 shows the relationship between the most essential three parameters with the ultimate drift ratio (DR_u).

The ultimate drift ratio and ω_i have a relatively high relationship, as can be shown in Fig. 9. A higher value of the column flexibility parameter, ω_i, indicates that the columns are more flexible than the lower. It is expected that for high ω_i values, the ultimate drift ratio will take smaller values. Assessing the models with the lowest ultimate drift ratio reveals that they typically have thick plates and are subject to significant axial forces. This is another anticipated outcome that the SPSW system working principle can explain. Therefore, as the axial load on the columns and thickness of the plate increases, the columns are more proponed to buckle. Thick plates cause an increase in the inward force acting on the columns. Clearly, the

models with the lowest axial force also have the maximum capacity, as would be predicted. Another significant consequence of this figure is that very high drift values can be attained if the column axial load and plate thickness could be adjusted with the selected column section. Similar to the previous instance, the drift ratio capacity may be pretty low even when the column axial load and plate thickness are at their lowest levels in a poorly built model.

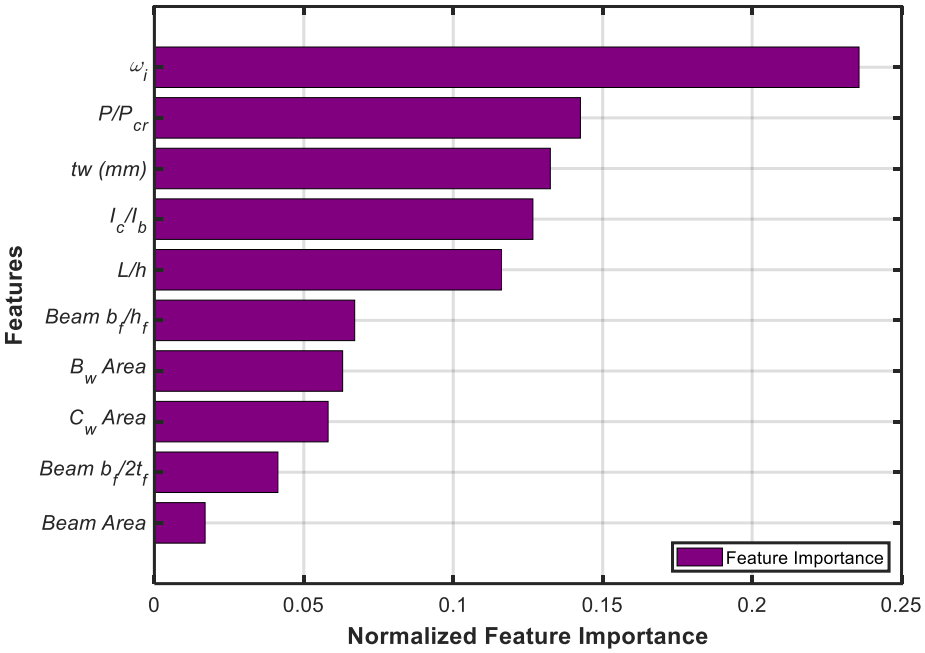

Fig. 8. Feature importance of XGBoost model.

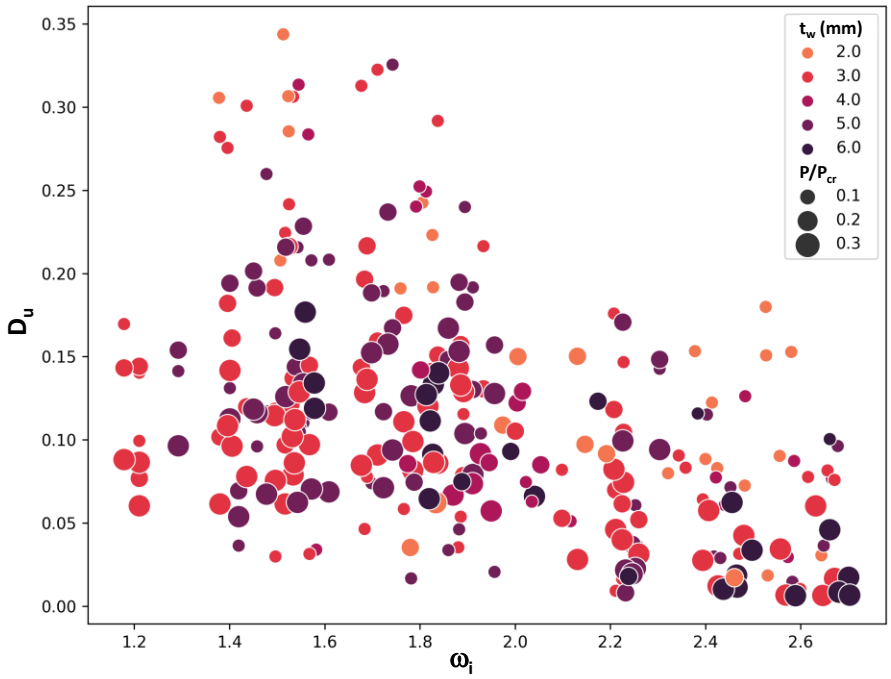

Fig. 9. Ultimate drift ratio – most effective parameters comparison.

Identifying the correlation between parameters is crucial to improve the data utilized in machine learning. Correlation between the input parameters is undesirable for machine learning. Because there is a high correlation between the input parameters, the model performs worse because the data set contains unused pairs. Additionally, any highly correlated parameters can improve the model's performance, while others can worsen it. The correlation coefficients for several variables in a dataset may be shown in a correlation matrix table. The matrix shows how each potential pair of variables in a table correlates. The correlation matrix is a table with rows and columns, and each cell displays the correlation between any two variables. Fig. 10 presents the correlation matrix of the parameters used in this study.

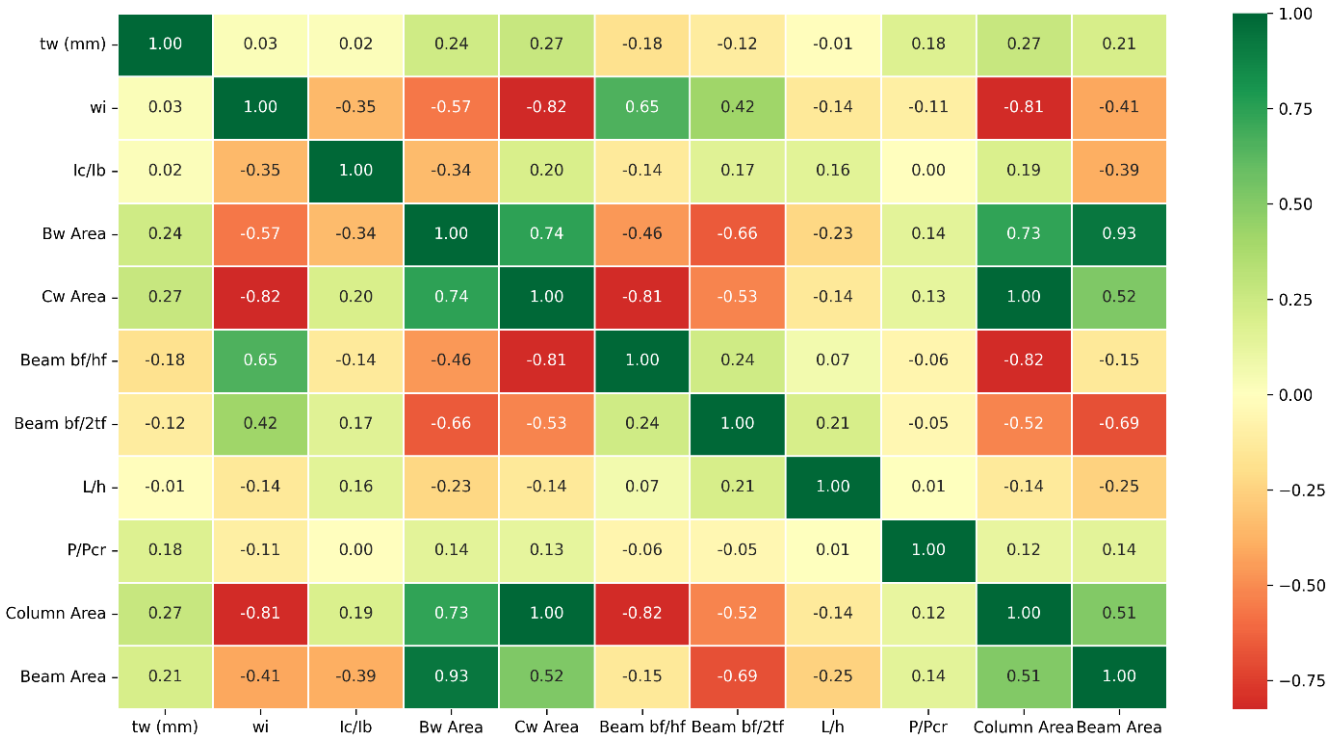

Fig. 10. Correlation matrix (XGBoost).

Some parameters have a very high correlation, as seen in Fig. 10. For instance, it is possible to conclude that the column area and the ω_i parameter have a strong inverse correlation. The relationship between beam web area and total beam area is also solid. The number of strong correlations might increase by looking at Fig. 10. That might be a reason for the relatively poor results of stacking-regressor. In this case, it can be concluded that the selected parameters should be optimized in machine learning.

On the other hand, the fact that the parameters t_w and P/P_{cr} typically do not exhibit a substantial correlation with any parameter indicates that two of the parameters which have the most extensive influence on the ultimate drift ratio were rather well selected. Similar to this, there was a low correlation between other factors and other relatively effective parameters, L/h and I_c/I_b. Assuming that (except for ω_i) parameters with high correlation are typically not very effective on the ultimate drift ratio would be reasonable.

In our analysis of feature importance, we utilized tree-based model, such as XGBoost, to gauge the significance of various parameters in predicting the ultimate drift ratio of steel plate shear wall (SPSW) systems. The feature importance was calculated primarily through the evaluation of the Gini impurity or related metrics within these models. Higher feature importance scores indicate a stronger influence of the respective parameters on the predictive accuracy of the models. Notably, parameters like ω_i, t_w, and P/P_{cr} emerged as the most critical factors affecting the ultimate drift ratio. These findings align coherently with established engineering knowledge in structural mechanics. For instance, ω_i, the column flexibility parameter, directly correlates with the stiffness of columns, impacting the structural deformation capacity. Similarly, the plate thickness (t_w) and the ratio of applied axial load to critical load (P/P_{cr}) are indicative of the structural robustness and load-carrying capabilities of SPSW systems. These parameters' prominence in our analysis underscores their pivotal roles in governing the behavior of such systems, affirming their relevance from an engineering standpoint.

5. Conclusions

Predicting the ultimate drift ratio in SPSW systems is important for engineers and the construction industry. It plays a key role in ensuring structural resilience during seismic events, guiding design optimization, and enhancing overall safety and cost-effectiveness in construction projects.

The performances of various machine learning methods in predicting the SPSW ultimate drift ratio were comprehensively evaluated in this study. The models were compared and evaluated based on their R-squared value, root-mean-squared error, and evaluation time. A grid search method was used to fine-tune the models' hyperparameters in order to maximize their performance. A StackedRegressor class was also used to combine the predictions of the different models in an attempt to enhance the models' overall performance. Then, compared to the individual models, these combined results were used to create more accurate predictions.

Machine learning procedures employing feature importance analysis are very useful in determining the relative importance of each parameter in a dataset in order to improve the performance of the prediction model or to reveal the underlying relationships in the data. It was demonstrated that ω_i, t_w, and P/P_{cr} are the most critical

parameters in the deformation capacity of SPSW systems. These parameters directly impact the behavior of the system.

It was found that the Artificial Neural Network (ANN) model exhibited the most accurate predictions among the various machine learning algorithms evaluated. For the ANN model, the lowest R-squared value that was obtained for the training, validation, and test groups was 0.85. The R-squared value for the analysis conducted on the entire dataset was found to be 0.94, indicating a high level of accuracy. Among the other models, the XGBoost model had the second-highest accuracy level with an R-squared value of 0.93. However, the ANN model had one of the worst performances in terms of evaluation time due to the use of a loop to optimize the number of neurons in the algorithm. The optimization of the number of neurons has a direct impact on the results. The data used in the analysis, which consisted of 292 data points, did not account for very complex data and it can be inferred that the models would work well with much more complex data in real-life applications. The ability of the model to make profound contributions to the usability of this model is an important aspect to consider.

Several limitations should be acknowledged in this study, notably the dataset's size and complexity. The dataset used for model training and evaluation comprised 292 instances, which, while informative, might not encapsulate the full breadth of potential scenarios encountered in real-world applications. The relatively small dataset size could potentially limit the model's ability to generalize well to diverse or unseen data patterns. Moreover, the inherent complexity of the structural behavior of steel plate shear walls (SPSW) systems adds another layer of challenge, as the dataset might not comprehensively cover all possible variations and scenarios observed in practical applications. These limitations may influence the generalizability of the results, suggesting that caution should be exercised when applying these models to different or more complex real-world scenarios.

Acknowledgements

None declared.

Funding

The authors received no financial support for the research, authorship, and/or publication of this manuscript.

Conflict of Interest

The authors declared no potential conflicts of interest with respect to the research, authorship, and/or publication of this manuscript.

Author Contributions

All of the authors made substantial contributions to conception and design, or acquisition of data, or analysis and interpretation of data; were involved in drafting the manuscript or revising it critically for important intellectual content; and gave final approval of the version to be published.

Data Availability

The datasets created and/or analyzed during the current study are not publicly available, but are available from the corresponding author upon reasonable request.

REFERENCES

Adeli H, Yeh C (1989). Perceptron learning in engineering design model. *Microcomputers in Civil Engineering*, 4, 247–256.

ANSYS (2016). Academic Research Mechanical, Release 17.2, Help System; *ANSYS. Inc.: Canonsburg, PA, USA.*

Breiman L (2001). Random forests. *Machine Learning*, 45(1), 5–32.

Chen T, Guestrin C (2016). XGBoost: A scalable tree boosting system. *Proceedings of the ACM SIGKDD International Conference on Knowledge Discovery and Data Mining*, 13-17-Augu, 785–794.

Deep Learning Toolbox - MATLAB. (n.d.). Retrieved January 11, 2023, from https://www.mathworks.com/products/deep-learning.html

Freund Y, Schapire R. E (1997). A Decision-theoretic generalization of on-line learning and an application to boosting. *Journal of Computer and System Sciences*, 55(1), 119–139.

Gürbüz M, Kazaz İ (2022a). A numerical investigation on the limitations of design equations for steel plate shear walls. *Teknik Dergi*, 33(5), 12677–12708.

Gürbüz M, Kazaz İ (2022b). Numerical evaluation on the steel plate shear wall design parameters for improved cyclic behavior. *International Journal of Steel Structures*, 22(2), 409–429.

Hajela P, Berke L (1991). Neurobiological computational models in structural analysis and design. *Computers and Structures*, 41(4), 657–667.

Inel M (2007). Modeling ultimate deformation capacity of RC columns using artificial neural networks. *Engineering Structures*, 29(3), 329–335.

Kalman Šipoš T, Sigmund V, Hadzima-Nyarko M (2013). Earthquake performance of infilled frames using neural networks and experimental database. *Engineering Structures*, 51, 113–127.

Li CH, Tsai KC (2008). Experimental responses of four 2-story narrow steel plate shear walls. *Proceedings of the 2008 Structures Congress*, vol. 314, Vancouver, Canada.

Luo H, Paal SG (2019). A locally weighted machine learning model for generalized prediction of drift capacity in seismic vulnerability assessments. *Computer-Aided Civil and Infrastructure Engineering*, 34(11), 935–950.

Mahfuz Ud Darain K, Shamshirband S, Jumaat MZ, Obaydullah M (2015). Adaptive neuro fuzzy prediction of deflection and cracking behavior of NSM strengthened RC beams. *Construction and Building Materials*, 98, 276–285.

Nguyen HD, Dao ND, Shin M (2021). Prediction of seismic drift responses of planar steel moment frames using artificial neural network and extreme gradient boosting. *Engineering Structures*, 242, 112518.

Scikit-learn: machine learning in Python – scikit-learn 1.2.0 documentation. (n.d.). Retrieved January 10, 2023, from https://scikit-learn.org/stable/index.html

Sun H, Burton HV, Huang H (2021). Machine learning applications for building structural design and performance assessment: State-of-the-art review. *Journal of Building Engineering*, 33, 101816.

Thai HT (2022). Machine learning for structural engineering: A state-of-the-art review. *Structures*, 38, 448–491.

Tibshiranit R (1996). Regression shrinkage and selection via the Lasso. *Journal of the Royal Statistical Society: Series B (Methodological)*, 58(1), 267–288.

Wu X, Ghaboussi J, Garrett JH (1992). Use of neural networks in detection of structural damage. *Computers and Structures*, 42(4), 649–659.

Xie Y, Ebad Sichani M, Padgett JE, DesRoches R (2020). The promise of implementing machine learning in earthquake engineering: A state-of-the-art review. *Earthquake Spectra*, 36(4), 1769–1801.

Ying X (2019). An overview of overfitting and its solutions. *Journal of Physics: Conference Series*, 1168(2).

Challenge Journal of Structural Mechanics

Research Article

The novelty design method in lightweight structures with low effective elastic modulus

Hojjat Ghahramanzadeh Asl [a,*], Derya Karaman [a]

[a] *Department of Mechanical Engineering, Karadeniz Technical University, 61080 Trabzon, Türkiye*

ABSTRACT

Lightweight structures are of great interest in industrial areas such as automotive, aerospace, and biomedical due to their lightness, and superior mechanical performance. The advantages of lightweight structures are increased with the spread of additive manufacturing and design them in various geometries. Beam-based structures and triply periodic minimal surface structures are currently used to extend these advantages. In this study, it is aimed to create die models of beam-based structures in order to contribute to the geometric diversity for lightweight structures. By designing the die lattice structures of the beam-based structures, the comparison of the mechanical performance of basic lattice and die lattice structures with the same porosity was carried out. For FCC, CFCC, and Octet-Truss lattice structures, basic lattice and die lattice structures are designed on scaffolds in 5x5x5 array with 50%, 60%, 70%, and 80% porosity. Numerical data were obtained for Ti6Al4V with compression tests simulated by applying pressure in the -y direction. According to numerical analyses, the effective elastic modulus decreased due to the increased porosity in both structure models. The CFCC and Octet Truss scaffolds have different force transmission performances. Likewise, this situation is observed in die lattice structures, but the force transmission with the surfaces reveals the difference of the structures. The effective elastic modulus of basic lattice structure with 80% porosity of the Octet Truss structure is approximately twice that of the die lattice structure. Thus, the use of die lattice structures will provide advantages for the design of lightweight structures with low elastic modulus.

ARTICLE INFO

Article history:
Received 6 January 2024
Revised 3 February 2024
Accepted 23 February 2024

Keywords:
Lattice structure
Effective elastic modulus
Finite element analysis
Additive manufacturing

1. Introduction

With the development of additive manufacturing technologies, lightweight structures are widely used in aerospace, marine, automotive, construction industries, biomedical, etc. in many engineering fields (Ghahramanzadeh Asl et al. 2023; Almalki et al. 2022; Sharma et al. 2022). In addition to the material saving advantage of lightweight structures, their superior performance such as high specific stiffness, strength, and energy absorption capacity are the main reasons for their wide use (Yang et al. 2021). The design and use of lightweight structures are accomplished by two methods: (1) material type variance; and (2) structure design (Sun et al. 2022). It is quite common to use porous structures modeled in various geometries for the design of structures.

Porous structures are formed by material reduction based on mechanical strength in the basic configuration. These reduction techniques are performed with stochastic (foam) or regular (cell architectures) based on topology optimization (Timercan et al. 2021; Feng et al. 2022). Cell architectures are infinitely replicable homogeneous structures in beam or surface-based forms. A wide variety of cell architectures are created with beam or surface forms having various geometrical properties, and thanks to this diversity, the performance requirements of the structures in the systems can be obtained (Wang et al. 2020). Among these structures, beam-based lattice

* *Corresponding author*. Tel.: +90-462-377-3149 ; E-mail address: h.kahramanzade@ktu.edu.tr (H. Ghahramanzadeh Asl)
ISSN: 2149-8024 / DOI: https://doi.org/10.20528/cjsmec.2024.02.002

structures are frequently preferred for porous structures in terms of modeling with simple design methods and accessibility. Beam-based structures are formed by the combination of various numbers of beams at different angles and with nodes. These data are the main parameters that affect the stiffness of the lattice structures as they cause flexing or bending in the beams. These effects of beams have been studied by many researchers. To investigate the design of impact resistant components, Nasrullah et al. (2020) preferred Octet Truss lattice structures to provide a special structural configuration that provides crush deformation. Peng et al. stated that fewer geometric defects of FCC and BCC structures can occur in Simple Cubic (SC), Body Centred Cubic (BCC), Simple Cubic Body Centred Cubic (SC-BCC), and Face Centred Cubic (FCC) lattice structures, which stand out with their energy absorption capabilities. They developed a parametric computational approach and created a numerical framework for estimating fatigue lives (Peng et al. 2020). Gatto et al. (2021) mechanically investigated diamond and rhombic dodecahedron lattice structures for the biomedical industry and experimentally noted that the compression behavior of these lattice structures is quite similar to natural bone. Triply periodic minimal surface structures (TPMS), defined as surface-based structures, are cell architectures that can be extended infinitely in the cartesian space plane. In TPMS structure, two different solid forms (network and sheet solids) are obtained with the same surface equations of the same architecture (Kapfer et al. 2011). Different geometries of lightweight structure, affect both the mechanical and permeability performance of structures. Günther et al. (2022) evaluated the mechanical performance of two lightweight structure geometries in TPMS structures for bone regeneration. As a result of this evaluation, the sheet solid model for cortical bone and the network solid model for trabecular cell architecture were suggested. In the overall assessment of the difference in TPMS structures, sheet solids were noted to have better mechanical properties in relative density compared to network solids (Kapfer et al. 2011; Al-Ketan et al. 2018). These differences are mainly related to the surface properties and wall thickness of the structures. However, these two form states have been expressed only for TPMS structures and no studies have been found in the literature regarding such a situation for beam-based lattices.

Beam-based lattice structures are symmetrical geometries that form repetitive arrays by combining different numbers of beams at different angles and nodes (Du Plessis et al. 2022; Letov et al. 2023). In addition, minimal surface unit cells provide the formation of porous structures where the curvature sum is equal to zero and can be multiplied infinitely in three directions (Fu et al. 2022). According to this information, die lattice models to be obtained from beam-based lattice structures can be considered as a new alternative for lightweight structures modeling, since they have surface properties. Die lattice structures are obtained by forming the basic lattice structures in the opposite direction with reference to their surfaces. As the novelty of this study, both basic models and die models of FCC, CFCC, and Octet Truss architectures are designed with 50%, 60%, 70%, and 80% porosity. To evaluate the mechanical properties difference between the lattice and die structures, the compression tests are simulated by the Finite Element Method and the effective elastic modulus of these lattice structures is determined. Also, the effects of structure type on effective elastic modules are analyzed by ANOVA. In addition, as a result of the equation obtained from OriginLab software, the results for the intermediate values can be predicted with high precision.

2. Material and Method

2.1. Design of lattice structures

In this study, FCC, CFCC, and Octet Truss were chosen for beam-based lattice structures. For each architecture, unit cells for both basic lattice structure and die structure were designed with 50%, 60%, 70%, and 80% porosity. Unit cell models with dimensions of 1 mm x 1 mm x 1 mm were obtained by using SolidWorks software. Die lattice structures were obtained by evacuating the basic lattice structures from the cube with dimensions of 1 mm x 1 mm x 1 mm in the fully filled structure with the cavity command. For this purpose, die lattice structures with 50%, 60%, 70%, and 80% porosity were designed from the basic lattice structures of 20%, 30%, 40%, and 50% porosity of each model (Fig. 1). Structures designed by this method have surface properties such as surface based TPMS structures.

Eq. (1) was used to calculate the porosity of the unit cells:

$$\text{Porosity} = 1 - (\rho_l/\rho_s) \tag{1}$$

In Eq. (1), ρ_l is the density of the lattice structures and ρ_s that of the solid from which it is obtained (Ashby et al. 2006). A priority classification according to the number of beams and nodes in beam-based structures is determined according to Maxwell's stability criterion (Eq. (2)) (Calladine et al. 1978).

$$M = b - 3j + 6 \tag{2}$$

In this criterion b and j terms are the number of beams and the number of nodes, respectively. The schematic representation of the terms in the equation was given in Fig. 2.

By determining the M criterion, the behavior of beam lattice structures under load is classified. Also, if $M<0$, bending in the structures is dominant, and if $M \geqslant 0$, stretching is dominant in the structure (Deshpande et al. 2001). The specified Maxwell criterion will apply to the basic models. Considering the design rules of die lattice, they are modeled on a surface basis, unlike beam structures. Therefore, this criterion cannot be applied to die lattice structures.

2.2. Finite element analysis

Scaffolds were modeled in 5x5x5 array at the x, y, and z direction with unit cells and the labeling of these models was given in Table 1.

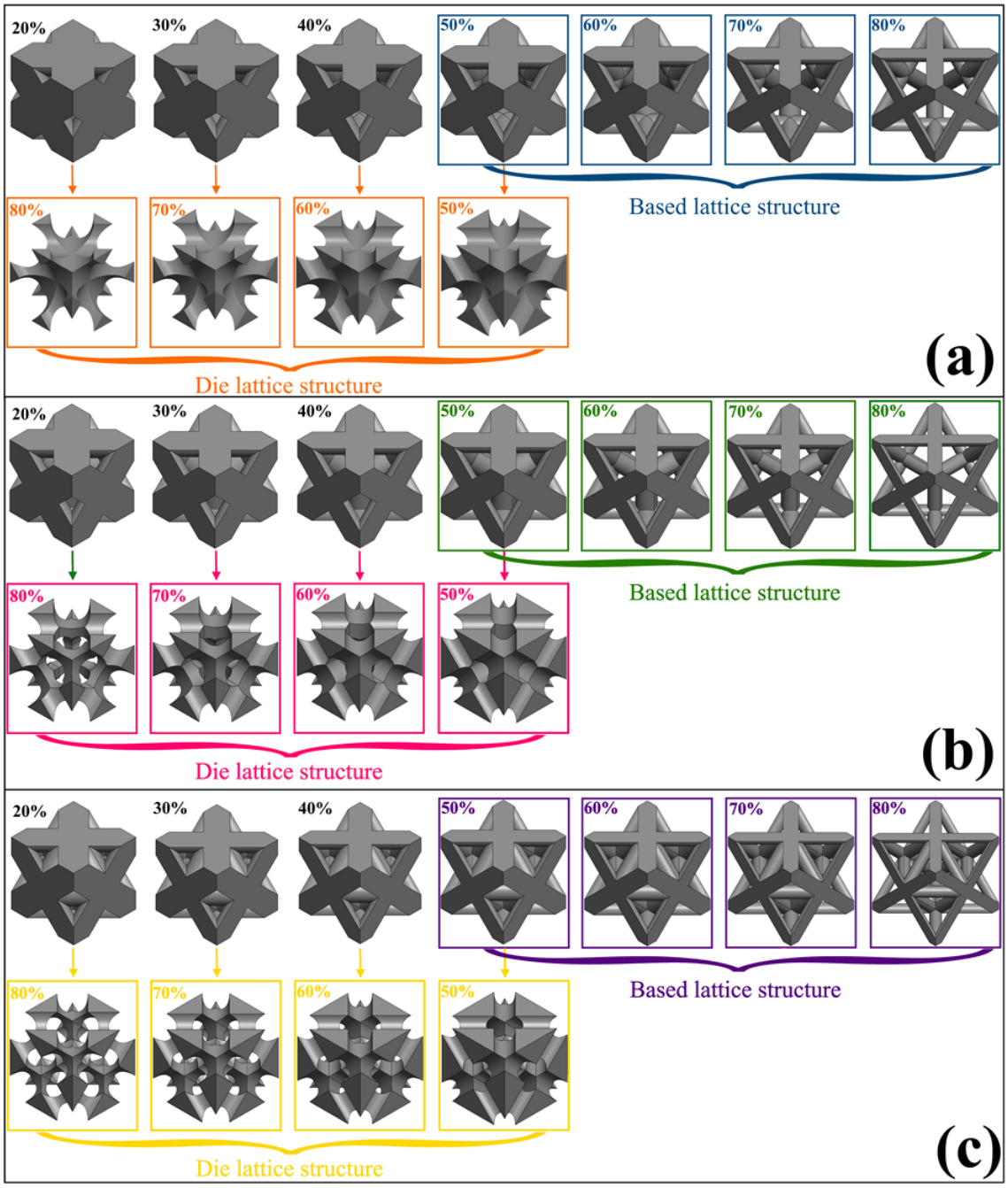

Fig. 1. Unit cells of die lattice structures designed using basic lattice structures: (a) FCC; (b) CFCC; (c) Octet Truss.

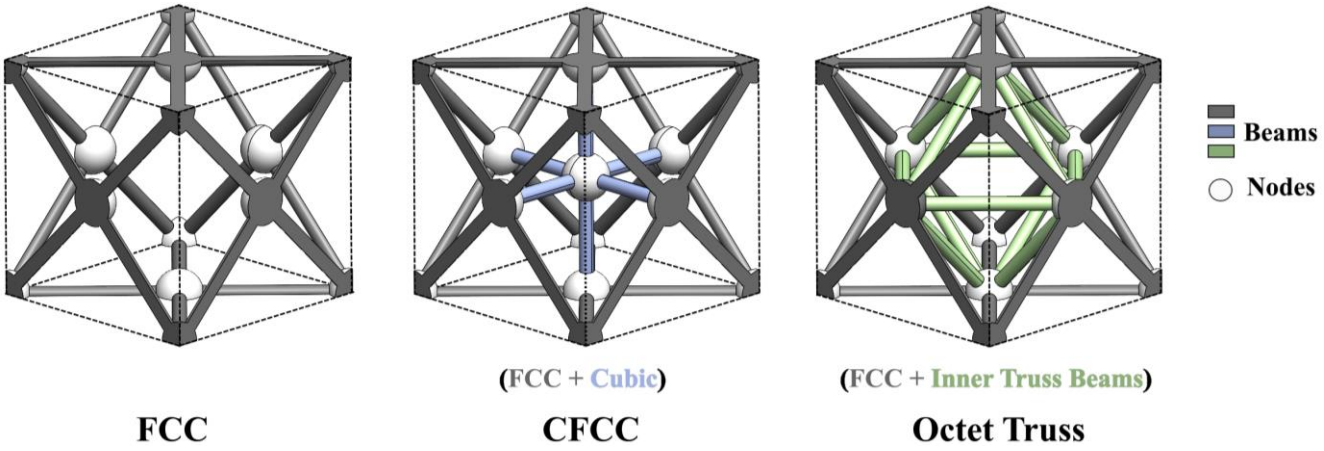

Fig. 2. Beams and nodes of FCC, CFCC, and Octet Truss unit cells.

Table 1. Labeling of scaffold structures.

Unit cell	Type of structure	Porosity			
		50%	60%	70%	80%
FCC	Basic lattice	FCC-50	FCC-60	FCC-70	FCC-80
	Die lattice	FCC_d-50	FCC_d-60	FCC_d-70	FCC_d-80
CFCC	Basic lattice	CFCC-50	CFCC-60	CFCC-70	CFCC-80
	Die lattice	$CFCC_d$-50	$CFCC_d$-60	$CFCC_d$-70	$CFCC_d$-80
Octet Truss	Basic lattice	Octet-50	Octet-60	Octet-70	Octet-80
	Die lattice	$Octet_d$-50	$Octet_d$-60	$Octet_d$-70	$Octet_d$-80

The mechanical performances of the scaffolds were determined according to the effective elastic modulus values. For this determination, compression tests on the scaffolds were simulated. Rigid plates were added to the top and bottom of the scaffold models (Fig. 3a). Plate-mounted scaffolds were transferred to the ANSYS Workbench software, and mesh structures were created. Especially due to the complex geometry of the latticed structure, the mesh element selection was performed as program controlled. The mesh grit of the structure was shown in Fig. 3b.

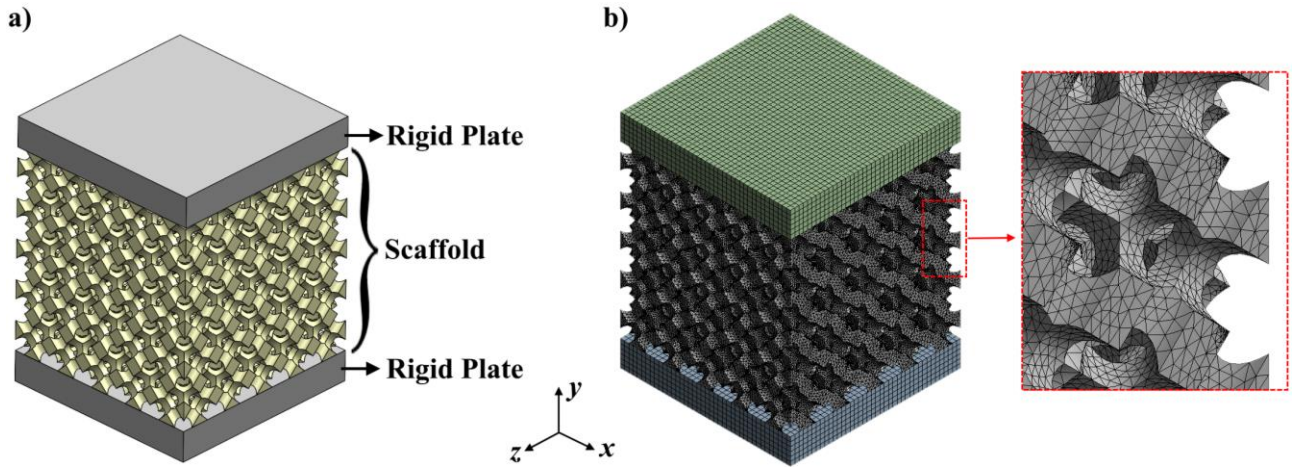

Fig. 3. Compression test models of scaffold; and b) sample mesh structure consisting of tetrahedral elements.

In order to determine the optimum mesh structure, mesh convergence tests with tetrahedral elements were applied and mesh structures with a number of approximately 1.5 million elements were accepted for analysis. The finite element analyses were defined as fixed plane for the bottom plate for the boundary conditions, fixed in the *x* and *z* directions for the top plate, and free in the *y* direction. The scaffold contact surfaces of both plates were defined as bonded (Karaman et al. 2022). As the analysis conditions, a compression pressure of 1 MPa was applied in the *-y* direction. Ti6Al4V alloy was selected as the material where the elastic modulus was 110 GPa and the Poisson ratio was 0.33 as material properties (Xu et al. 2019). As a result of these analyses, the effective elastic modulus (E_{eff}) values of each scaffold were calculated according to Hooke's law. In Hooke's law:

$$\sigma = E \times \varepsilon \qquad \varepsilon = \frac{\Delta L}{L_0} \qquad E_{eff} = \left(\frac{\sigma}{\varepsilon}\right) = \frac{(\sigma \times L_0)}{\Delta L} \qquad (3)$$

In Eq. (3), σ, L_0, and ΔL are the applied pressure (MPa), the initial length of the model (mm), and directional deformation (mm), respectively.

Additionally, a statistical analysis was performed to determine the parameters using the effective elastic modulus data of the scaffolds. One-way analysis of variance was used to investigate statistically significant differences (ANOVA). A p-value less than 0.05 was considered to indicate a statistically significant difference. Furthermore, the curve fitting technique was used to determine the closest match via analyzing the correlation between the dependent and independent variables and constructing a mathematical function, either linear or nonlinear, which includes the curve according to the data points in the collection. The input parameters for this investigation were (*x, y, z*). The data obtained from each scaffold model were analyzed using OriginLab software for evaluating the architecture and porosity of the unit cell. Thus, the effects of design method on effective elastic modules are more clearly understood. In addition, as a result of the equation obtained, the results for the intermediate values can be predicted with high precision.

3. Results and Discussion

The maximum von-Mises stress values that occur in scaffold structures because of compression tests are given in Table 2. According to von-Mises stress values, all scaffolds do not exceed the yield strength in compression of the Ti alloy (970 MPa). Maximum stress values are realized in 80% porous scaffolds in the same architectures. However, the maximum von-Mises stress of the scaffolds gradually increases with increasing porosity.

Table 2. Maximum von-Mises stress values of scaffold structures.

Porosity	von-Mises stress (MPa)					
	FCC	FCC_d	CFCC	$CFCC_d$	Octet	$Octet_d$
50%	18.43	19.31	22.40	15.13	26.97	13.49
60%	26.32	29.37	27.15	26.34	38.13	21.42
70%	41.39	47.16	35.95	44.57	60.12	45.24
80%	74.30	104.64	59.32	89.95	96.70	201.23

The stress distributions occurred in each lattice structure are shown in Fig. 4. The stress distribution of the scaffolds is relatively uniform in von-Mises stress counters. This represents the excellent stress transmission properties of the lattice structures (Nasrullah et al. 2020). When the basic lattice models are evaluated as quantitative amounts, the order of stress values is Octet>CFCC>FCC for 50% and 60% porosity. For 70% and 80% porosity, it is Octet>FCC>CFCC. The occurrence of higher von Mises stress values in the Octet Truss lattice structure compared to both lattice structures is related to the number of beams (Viswanath et al. 2022). It has more beams while having the same number of nodes as FCC. This increases the stress by causing the load density at the joint intersection point in the structure. The variability between FCC and CFCC structures with increasing porosity can be expressed in a similar method. The beams intersecting at the node point in the body center of CFCC structures affect the mechanical behavior of the structure (Zheng et al. 2019). CFCC structures do not differ much from FCC up to 60% porosity. However, with the decrease of the cross-sectional area after 70% porosity, high stresses occur in FCC structures due to structural refining (Zheng et al. 2019). A classical quantitative sort cannot be established for die lattice structures. There are different quantitative sorts within each porosity group. This is affected by the variability of the number of beams and the location of the node points that forming the cavity in the die lattice structures. FCC die lattice structures have a higher tensile value compared to other structures up to 70% porosity. At 80% porosity, Octetd scaffold has the highest stress (201.23 MPa). It is known in the literature that the yielding behavior occurs at 45° during loading in structures (Xu et al. 2019). The cavities created at 45° in the die lattice structures are the main cause of the high stresses. According to the maximum von-Mises stresses, the FCC and CFCC basic lattice structures have lower stress values than the die lattice structures. For Octet Truss, this is the opposite, except for 80% porosity. Octet die lattice structures have lower stress values compared to basic lattice structures. This is all about the angle of cavities formation and the variability in the cross-sectional area of the structure.

The directional deformation values within the elastic limits according to the compression analyses are given in Table 3. For all structures, the directional deformation value increases with the increase in porosity.

In Fig. 5, the visuals of the directional deformations in the structures are given. For all structures, the directional deformation value increases with the increase in porosity. At 50% porosity, the values of the basic lattice structures and the die lattice structures are relatively close to each other. However, with increasing porosity, this situation disappears. With the increase in porosity, the solid volume in the structures decreases and the cross-sectional area decreases (Pham et al. 2020). These refining in the structures reduce the resistance to the force which applies from the y direction. Thus, the directional deformation values increase.

Table 3. Directional deformation values on the scaffolds.

Porosity	Directional deformation (mm) (*y* axis)					
	FCC	FCC_d	CFCC	$CFCC_d$	Octet	$Octet_d$
50%	0.00021012	0.00020916	0.00021680	0.00021223	0.00025220	0.00027175
60%	0.00032741	0.00034049	0.00031772	0.00033906	0.00038795	0.00047018
70%	0.00055005	0.00064242	0.00049198	0.00061829	0.00063133	0.00094640
80%	0.00104240	0.00177290	0.00085139	0.00147470	0.00114580	0.00288850

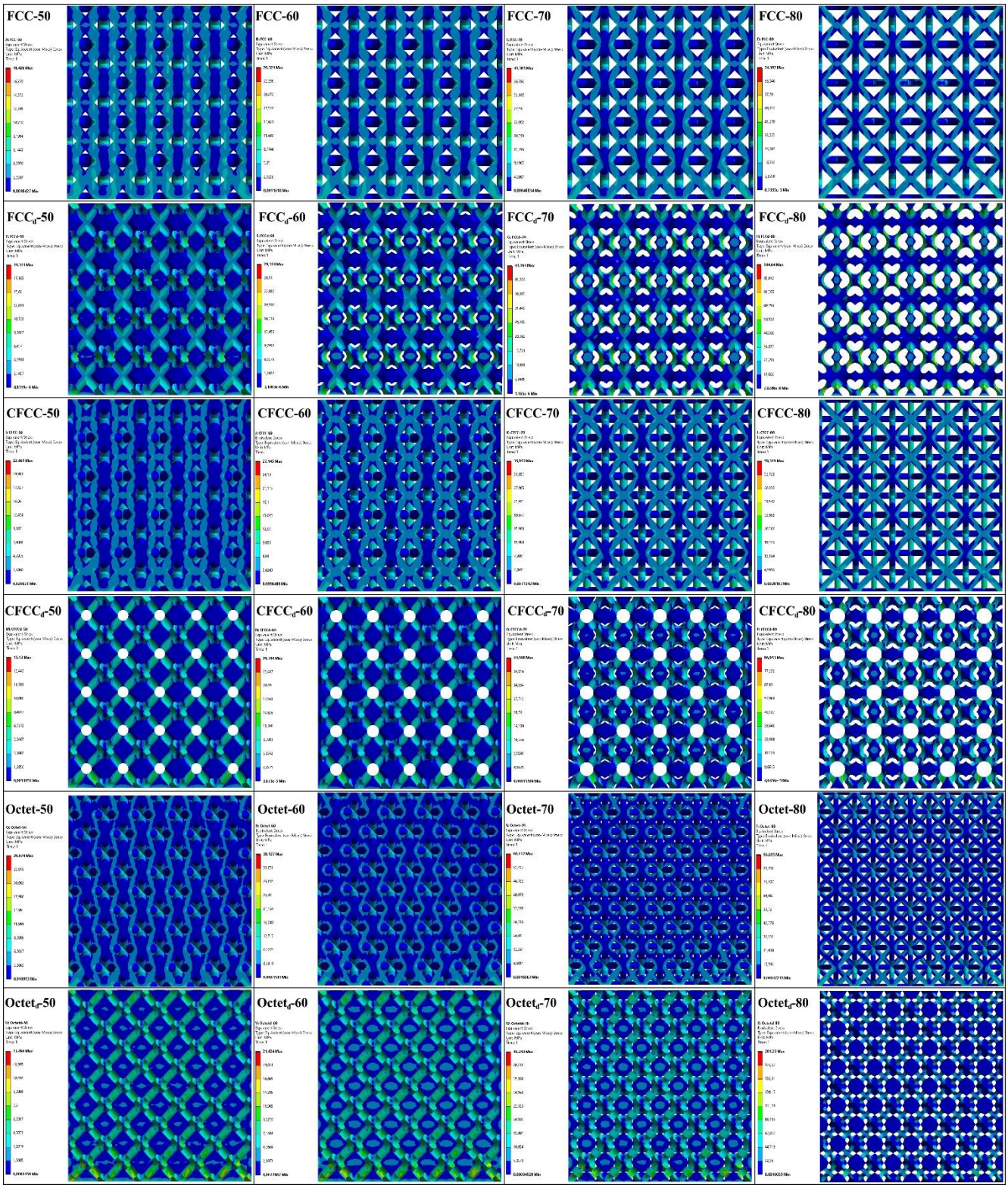

Fig. 4. The distributions of von-Mises stresses occurred in the basic lattice structures and the die lattice structures.

According to the deformation values given in Table 3, the effective elastic modulus values of the scaffolds are calculated according to Hooke's law. Comparison of effective elastic modules of scaffold structures with each other is shown in Fig. 6. In the general impression, the effective elastic modulus value decreases with increasing porosity in the three lattice types. In addition, the die lattice structures of a lattice type, have lower effective elastic modulus values than the basic lattice structures. In FCC and CFCC lattice structures with 50% porosity, basic and die lattice structures are formed at approximately the same values. This situation is not observed in the Octet Truss lattices. Since the directional deformation value in the Octetd-50 model is higher, it has a lower effective elastic modulus compared to the Octet-50.

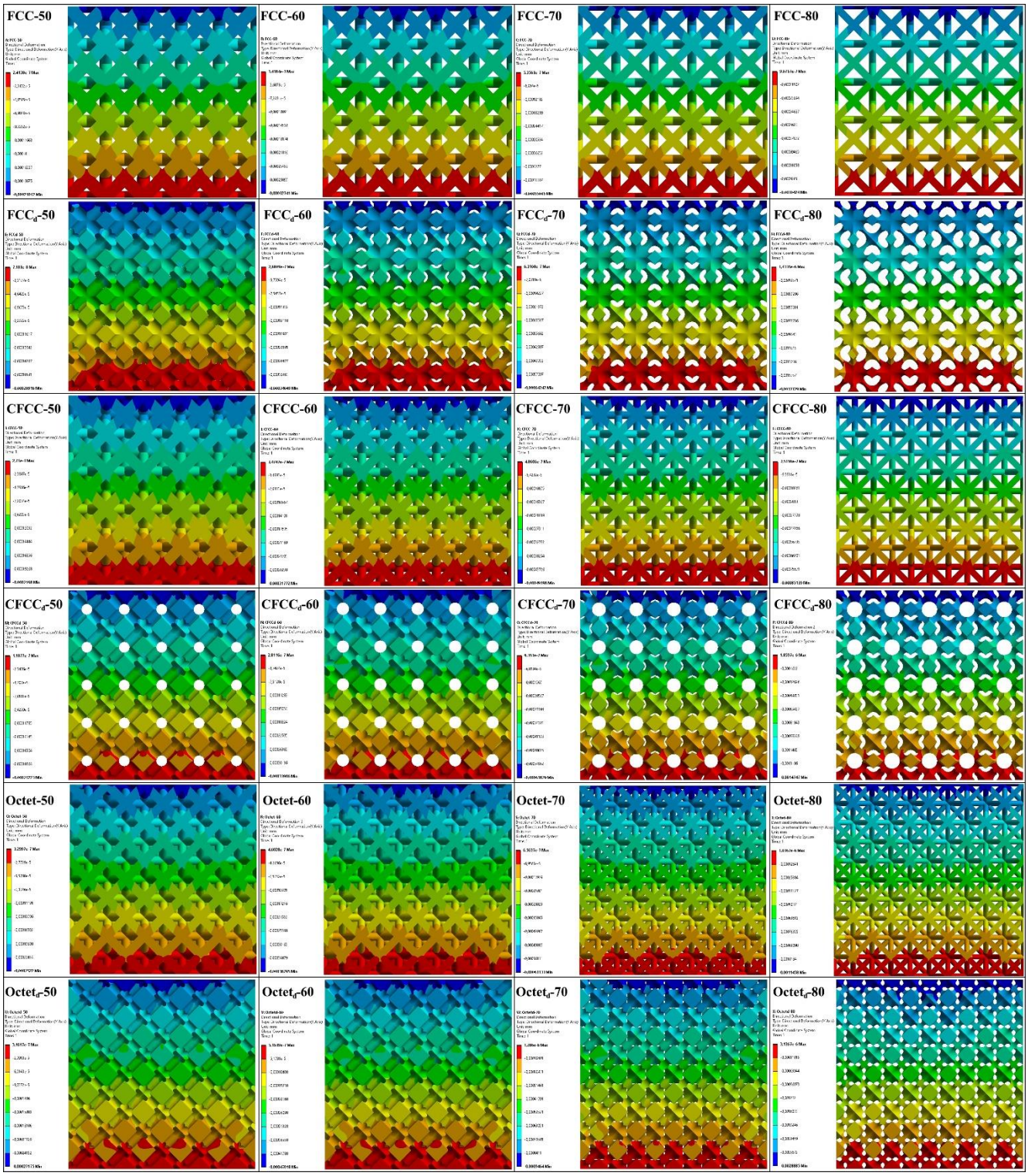

Fig. 5. The distributions of directional deformation (*y*-axis) occurred in the basic lattice structures and the die lattice structures.

With the increase of porosity, the elastic modulus between the basic lattice structure and the die lattice structure increases at different rates in the same lattice type. For example, there is a 3.8% difference between FCC-60 and FCCd-60 structures, 14.4% between FCC-70 and FCCd-70 structures, and 41.2% between FCC-80 and FCCd-80 structures. While there is a 6.29% difference between CFCC-60 and CFCCd-60 structures in CFCC lattice structures, there is 20.4% difference between CFCC-70 and CFCCd-70 structures, and 42.2% difference between FCC-80 and FCCd-80 structures. In Octet Truss lattice structures, these difference values occur significantly at 50% porosity. There is a difference of 7.2% between Octet-50 and Octetd-50, 17.5% between Octet-60 and Octetd-60, 33.3% between Octet-70 and Octetd-70, and 60.3% between Octet-80 and Octetd-80. The reason for the increase in the differences is the increase in the directional deformation values.

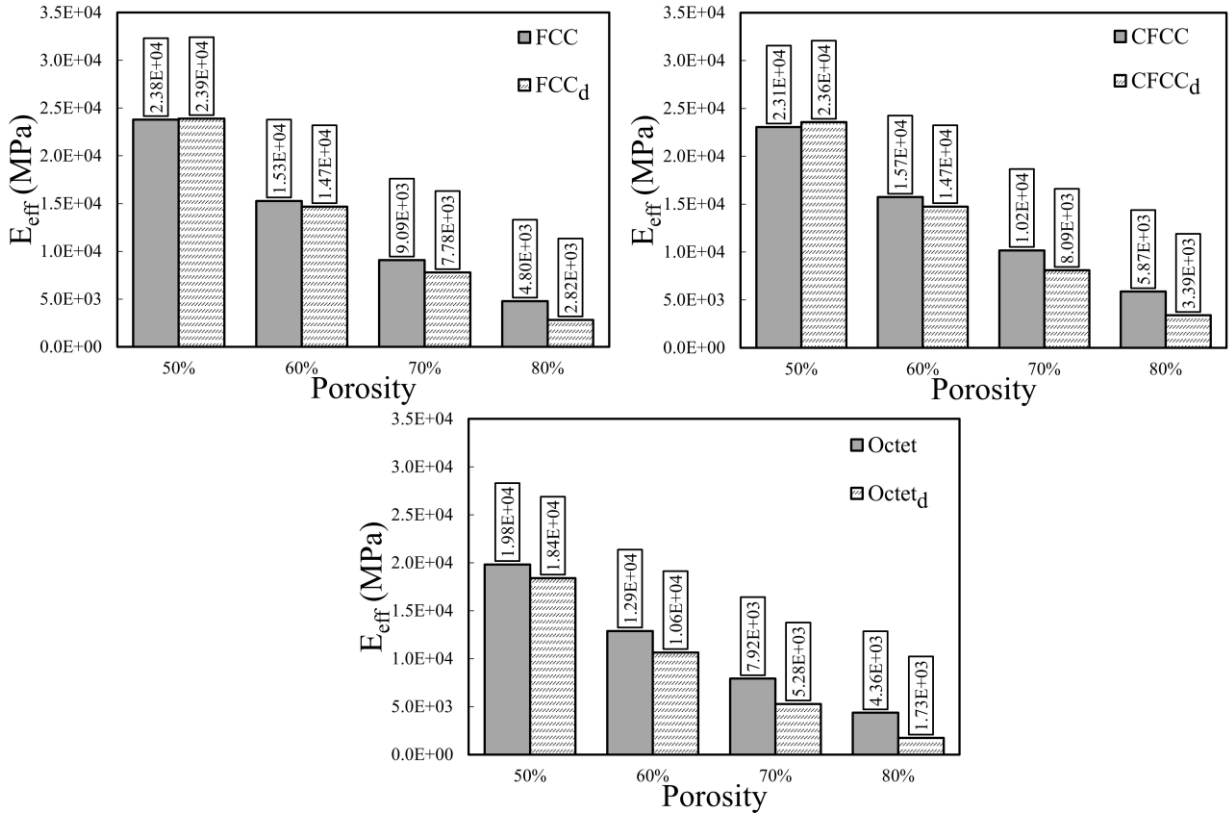

Fig. 6. Effective elastic modulus plot of basic lattice structures and die lattice structures of FCC, CFCC, and Octet Truss.

Octet Truss lattice structures have lower elastic modulus values than other lattice structures. This situation can be associated with Maxwell values (Table 4).

Table 4. Maxwell's criteria for beam-based unit cells.

	FCC	CFCC	Octet Truss
Maxwell's number	-12	-9	0

CFCC and Octet Truss lattices are constructed based on the FCC lattice structure by adding different numbers of beams and nodes (Fig. 2). CFCC lattice structure has 1 more number of nodes and 6 additional beams, unlike FCC. In Octet Truss structures, the nodes are the same as the FCC, but the additional 8 beams form a connection between the surface centers. CFCC structures show more strength in loadings from the y direction. The main reason why CFCC lattice structures show relatively higher strength compared to FCC is the nodes located in the center of the body. Refai et al. (2020) reported the effective elastic properties of 17 different beam-based lattices for Titanium material. According to the outputs of their studies, the CFCC model has higher effective elasticity than both FCC and Octet Truss structures of the same porosity. It is advantageous for these structures that the node, which appears as the intersection point of in the body center, has a higher load-bearing potential. In other words, while tension occurs in the beams cross at the center of the volume, it is seen that stronger structures will be obtained by the formation of compression in the outer beams (Park et al. 2022). Octet Truss structures have the lowest strength among these three structures. Although it has the same node as the FCC lattice structure, the increase in beams joining at these nodes causes this low. The vertical load on the lattice structure is covered by 8 beams that converge at a node, and the nodal points are displaced in all three directions. This causes the bending of beams in Octet Truss structures to occur at a higher rate compared to other lattice structures.

Quantitative ordering obtained in the basic lattice structures in terms of strength is valid for die lattice structures. In other words, CFCCd structures have higher effective elastic modulus than FCCd and Octetd. Verma et al. (2022), who investigated the mechanical properties of the contact between metal and polymer, created resin models with the die method. According to numerical analysis, they noted that CFCC die structures have higher tensile strength than Kelvin structures among the structures they investigated. CFCCd has higher strength compared to other lattice structures in the same porosity, while Octetd has the lowest strength. Since there is no beam in these structures, surface behavior is in the foreground. Die lattice structures provide their continuity with surfaces such as minimal surface structures. However, instead of the surface equations in TPMS structures, it can be defined as the beam surfaces forming the cavity. As mentioned in the literature, lattice structures (especially TPMS) are frequently preferred in various industrial areas such as biomedical and heat transfer due to their surface area properties (Dixit et al. 2022). Tang et al. (2023) performed numerical and experimental analyses using TPMS unit cells (Diamond, Gyroid, and I-WP) to improve the heat transfer process and examine

the performance effects. It was stated that the results differ according to the surface geometry and surface area, and they stated that the best result was obtained from the I-WP unit cell. Al-Ketan and Abu Al-Rub (2021), who simplifies the creation of two different unit cells in TPMS structures with the same surface equations, report that the surface areas change depending on the cell architecture. Expressing this difference for use in the biomedical field, Günther et al. (2022) numerically considered that the network and sheet solids of TPMS structures can provide alternatives for different bone tissues. The die lattice structures created in this study also have a minimal surface geometry similar to TPMS structures. Due to these properties, the load bearing and mechanical strength properties vary according to the surface geometry. Surface geometries will change according to the angles of various beam numbers in beam-based structures.

As a result of statistical analyses, S/N ratio charts are given in Fig. 7 for the effect levels of parameters on the mechanical performance of scaffold structures. The signal value (S) in this sentence refers to the value that has to be measured, while the noise value (N) represents the level at which contaminants affect the measured value. The graphs of the obtained signal-to-noise ratios show the extent of impact of each variable parameter used in the investigation. ANOVA analysis was used to ascertain the significant levels of variable factors that impact the mechanical characteristics of the constructions, in addition to the S/N ratio. The Minitab program was used to carry out this research.

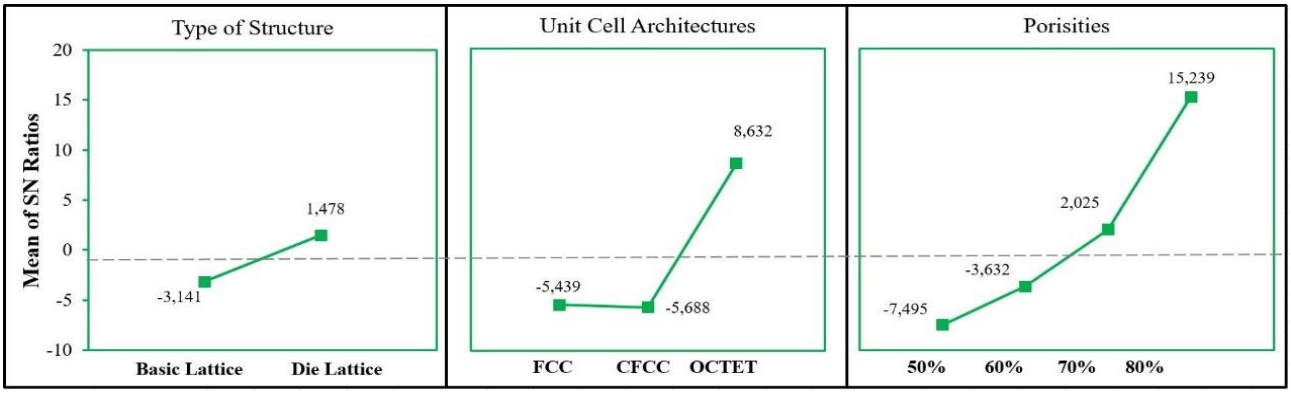

Fig. 7. Influence of the evaluated parameters on the effective elastic modulus.

The residual error of 0.08% is the foundation for these graphics. The charts show that porosity, unit cell architecture, and type of structure have an impact on the effective elastic modulus of the scaffold, accordingly. In this evaluation, porosity is considered the most important parameter at a rate of 54.55%. The effect of unit cell architecture is 34.36%. Type of structures are 11.01% effect on the mechanical performance of the scaffolds. As can be seen from this analysis, the effect of the structure type is significant. With the use of this structure type, scaffold structures with a lower elastic modulus can be obtained. On the other hand, Effective elastic modulus values are transferred to OriginLab software to establish the relationship between results achieved. For each type of structure, equations are obtained using the curve fitting method in OriginLab software according to all unit cell architecture and porosities. Considering the scaffold structure type first, if the "x" value is unit cell architecture and the "y" value is taken as porosity rates (%), the following equations and R squared values for each structure type are seen in Table 5. These curve fitting observations are shown graphically in Fig. 8.

Table 5. Curve fitting analysis results in terms of scaffold structure type.

Cure fitting equation	Structure type	Constants values	R-square
$f(x,y,z) = a_0 + a.x + b.y + c.x^2 + d.y^2 + e.x.y$	Basic lattice	$a_0 = 91063 \pm 1476$ $a = 1013 \pm 121$ $b = -1841 \pm 43$ $c = -1471 \pm 58$ $d = 8.85 \pm 0.35$ $e = 59.55 \pm 3.10$	0.999
	Die lattice	$a_0 = 103322 \pm 1417$ $a = 706 \pm 87$ $b = -2165 \pm 51$ $c = -1793 \pm 110$ $d = 10.57 \pm 0.79$ $e = 74.15 \pm 7.88$	0.998

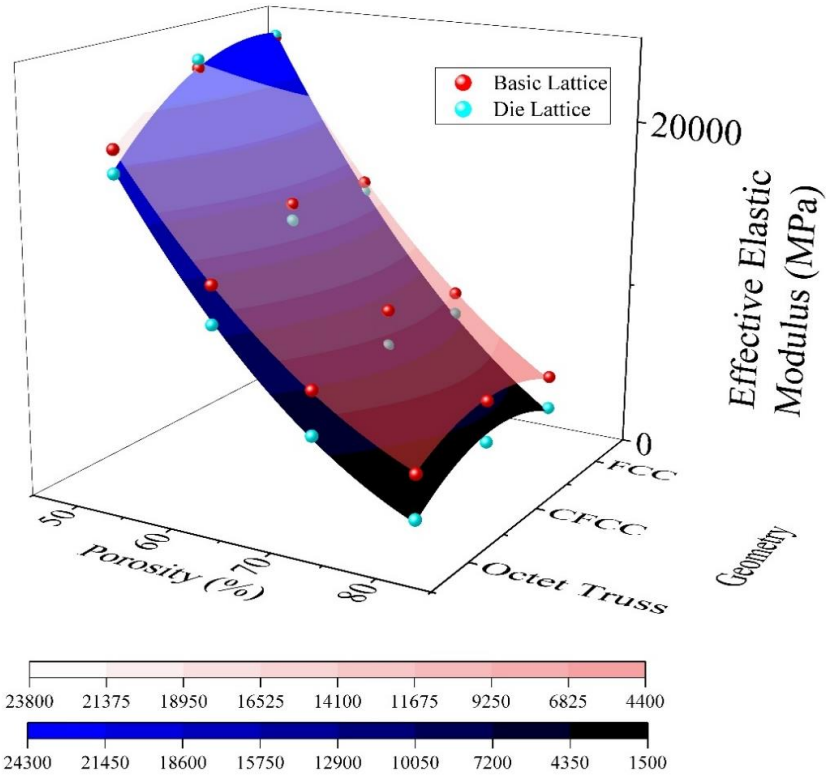

Fig. 8. The graphics of curve fitting results for each structure type.

By using the equations given in Table 5, it will be possible to obtain how much effective elastic modulus of scaffolds will have with inserting the elastic modulus value of the unit cell architecture and the porosity desired to be produced into the equations.

4. Conclusions

In this study, the usability of die structures based on beam-based structures for lightweight structures was investigated. The basic lattice structures and die lattice structures of FCC, CFCC, and Octet Truss unit cells were modeled at 50%, 60%, 70%, and 80% porosity. Mechanical strength properties of a total of 24 lattice structures were analyzed numerically. The directional deformation values in lattice structures with the same architecture increased as the porosity increased in both the basic lattice structure and the die lattice structures. These increases caused a decrease in the effective elastic modules for both structures as the porosity increased. Both the basic lattice structure and the die lattice structure of the CFCC architecture show higher mechanical strength compared to other architectures. In addition, die lattice structures with the same porosity in architecture have lower effective elastic modules. As a result of the ANOVA analysis, it was seen that the structure type had an effect of ~11%. The main reason for this is that surface connections come in effectively instead of beams for load transmission. The study provides a reference for innovating design configurations of lattice structures by modeling lightweight structures with low elastic modulus. The polynomial equations, which represent second-order curves, were classified into three groups based on the curve fitting approach used to the data received from finite element analysis. The coefficient of determination (R-square) for these equations exceeded 0.99. The formulae provided allow for the calculation of the effective elastic modulus without any restrictions, by using two established constant values related to the relevant fields. The calculated correlations for the curve equation demonstrated adequate accuracy for the engineering field. Because of their use, these curve equations provide an abundance of options for the geometric and mechanical characteristics of the structure, thus providing an invaluable resource for production planning in an efficient way.

Acknowledgements

None declared.

Funding

The authors received no financial support for the research, authorship, and/or publication of this manuscript.

Conflict of Interest

The authors declared no potential conflicts of interest with respect to the research, authorship, and/or publication of this manuscript.

Author Contributions

All of the authors made substantial contributions to conception and design, or acquisition of data, or analysis and interpretation of data; were involved in drafting the manuscript or revising it critically for important intellectual content; and gave final approval of the version to be published.

Data Availability

The datasets created and/or analyzed during the current study are not publicly available, but are available from the corresponding author upon reasonable request.

REFERENCES

Al-Ketan O, Rowshan R, Al-Rub RKA (2018). Topology-mechanical property relationship of 3D printed strut, skeletal, and sheet based periodic metallic cellular materials. *Additive Manufacturing*, 19, 167-183.

Al-Ketan O, Abu Al-Rub RK (2021). MSLattice: A free software for generating uniform and graded lattices based on triply periodic minimal surfaces. *Material Design and Processing Communications*, 3(6), e205.

Almalki A, Downing D, Lozanovski B, Tino R, Du Plessis A, Qian M Brandt M, Leary M (2022). A digital-twin methodology for the non-destructive certification of lattice structures. *JOM*, 74(4), 1784-1797.

Ashby MF (2006). The properties of foams and lattices. *Philosophical Transactions of the Royal Society A: Mathematical, Physical and Engineering Sciences*, 364(1838), 15-30.

Calladine CR (1978). Buckminster Fuller's "tensegrity" structures and Clerk Maxwell's rules for the construction of stiff frames. *International Journal of Solids and Structures*, 14(2), 161-172.

Deshpande VS, Ashby MF, Fleck NA (2001). Foam topology: bending versus stretching dominated architectures. *Acta Materialia*, 49(6), 1035-1040.

Dixit T, Al-Hajri E, Paul MC, Nithiarasu P, Kumar S (2022). High performance, microarchitected, compact heat exchanger enabled by 3D printing. *Applied Thermal Engineering*, 210, 118339.

Du Plessis A, Razavi SMJ, Benedetti M, Murchio S, Leary M, Watson M, Bhate D, Berto F (2022). Properties and applications of additively manufactured metallic cellular materials: A review. *Progress in Materials Science*, 125, 100918.

Feng Y, Huang T, Gong Y, Jia P (2022). Stiffness optimization design for TPMS architected cellular materials. *Materials & Design*, 222, 111078.

Fu H, Kaewunruen S (2022). Experimental and DEM investigation of axially-loaded behaviours of IWP-based structures. *International Journal of Mechanical Sciences*, 235, 107738.

Gatto ML, Groppo R, Bloise N, Fassina L, Visai L, Galati W, Iuliano L, Mengucci P (2021). Topological, mechanical and biological properties of Ti6Al4V scaffolds for bone tissue regeneration fabricated with reused powders via electron beam melting. *Materials*, 14(1), 224.

Ghahramanzadeh Asl H, Altıntaş Kahriman E, Karaman D (2023). Numerical investigation of the effective mechanical properties of Octet Truss lattice structures with different strut geometry. *Challenge Journal of Structural Mechanics*, 9(4), 133-144.

Günther F, Wagner M, Pilz S, Gebert A, Zimmermann M (2022). Design procedure for triply periodic minimal surface based biomimetic scaffolds. *Journal of the Mechanical Behavior of Biomedical Materials*, 126, 104871.

Kapfer SC, Hyde ST, Mecke K, Arns CH, Schröder-Turk GE (2011). Minimal surface scaffold designs for tissue engineering. *Biomaterials*, 32(29), 6875-6882.

Karaman D, Ghahramanzadeh Asl H, Altıntaş Kahriman E (2022). Estimation and comparison of effective elastic modulus of different scaffolds using curve fitting method for additive manufacturing field. *Arabian Journal for Science and Engineering*, 47, 15973–15987.

Letov N, Fiona Zhao Y (2023). Beam-based lattice topology transition with function representation. *Journal of Mechanical Design*, 145(1), 011704.

Nasrullah AIH, Santosa SP, Dirgantara T (2020). Design and optimization of crashworthy components based on lattice structure configuration. *Structures*, 26, 969-981.

Park SJ, Lee JH, Yang J, Heogh W, Kang D, Yeon SM, Kim SH, Hong S, Son Y, Park J (2022). Lightweight injection mold using additively manufactured Ti-6Al-4V lattice structures. *Journal of Manufacturing Processes*, 79, 759-766.

Peng C, Tran P, Nguyen-Xuan H, Ferreira A (2020). Mechanical performance and fatigue life prediction of lattice structures: Parametric computational approach. *Composite Structures*, 235, 111821.

Pham A, Kelly C, Gall K (2020). Free boundary effects and representative volume elements in 3D printed Ti–6Al–4V gyroid structures. *Journal of Materials Research*, 35(19), 2547-2555.

Refai K, Montemurro M, Brugger C, Saintier N (2020). Determination of the effective elastic properties of titanium lattice structures. *Mechanics of Advanced Materials and Structures*, 27(23), 1966-1982.

Sharma D, Hiremath SS, Kenchappa NB (2022). Bio-inspired Ti-6Al-4V mechanical metamaterials fabricated using selective laser melting process. *Materials Today Communications*, 33, 104631.

Sun G, Chen D, Zhu G, Li Q (2022). Lightweight hybrid materials and structures for energy absorption: A state-of-the-art review and outlook. *Thin-Walled Structures*, 172, 108760.

Tang W, Zhou H, Zeng Y, Jiang C, Yang P, Li Q, Fu J, Huang Y, Zhao Y (2023). Analysis on the convective heat transfer process and performance evaluation of Triply Periodic Minimal Surface (TPMS) based on Diamond, Gyroid and Iwp. *International Journal of Heat and Mass Transfer*, 201, 123642.

Timercan A, Sheremetyev V, Brailovski V (2021). Mechanical properties and fluid permeability of gyroid and diamond lattice structures for intervertebral devices: functional requirements and comparative analysis. *Science and Technology of Advanced Materials*, 22(1), 285-300.

Verma S, Yang CK, Lin CH, Jeng JY (2022). Additive manufacturing of lattice structures for high strength mechanical interlocking of metal and resin during injection molding. *Additive Manufacturing*, 49, 102463.

Viswanath A, Khan KA, Barsoum I (2022). Design of novel isosurface strut-based lattice structures: Effective stiffness, strength, anisotropy and fatigue properties. *Materials & Design*, 224, 111293.

Wang C, Gu X, Zhu J, Zhou H, Li S, Zhang W (2020). Concurrent design of hierarchical structures with three-dimensional parameterized lattice microstructures for additive manufacturing. *Structural and Multidisciplinary Optimization*, 61, 869-894.

Xu Y, Zhang D, Hu S, Chen R, Gu Y, Kong X, Tao J, Jiang Y (2019). Mechanical properties tailoring of topology optimized and selective laser melting fabricated Ti6Al4V lattice structure. *Journal of the Mechanical Behavior of Biomedical Materials*, 99, 225-239.

Yang JS, Chen SY, Li S, Pang YZ, Schidt R, Schröder KU, Qu J, Wu LZ (2021). Dynamic responses of hybrid lightweight composite sandwich panels with aluminum pyramidal truss cores. *Journal of Sandwich Structures & Materials*, 23(6), 2176-2195.

Zheng HD, Liu LL, Deng CL, Shi Z, Ning C (2019). Mechanical properties of AM Ti6Al4V porous scaffolds with various cell structures. *Rare Metals*, 38, 561-570.

Challenge Journal of Structural Mechanics

Research Article

Effect of different trimline extension of clear aligners in combination with Class II elastics on the mandibular dentition: a finite element analysis

Nurver Karslı [a,*], Bahanur Hilal Kisbet [a]

[a] *Department of Orthodontics, Karadeniz Technical University, 61080 Trabzon, Türkiye*

ABSTRACT

The objective of this study is to evaluate the effect of different trimline extension of aligners and the effect of elastics applied through the slit cutouts and buttons on the mandibular dentition using Class II intermaxillary elastics combined with clear aligner treatment. Three-dimensional (3D) finite element models that simulate the effects of Class II elastics on the mandibular arch in four different scenarios were studied, named, straight and high trimline aligner (HTLA) model with elastic applied through buttons (Model 1), straight and low trimline aligner (LTLA) model with elastic applied through buttons (Model 2), HTLA model with elastic applied through slit cutout (Model 3), LTLA model with elastic applied through slit cutout (Model 4). 3D displacements of the teeth, von Mises stress (VMS) in the periodontal ligament (PDL) were calculated. In all models, the crown of the mandibular anterior teeth moved labially, the root moved lingually, and the mandibular first molars moved mesially. Among all models, labialization of incisors and mesialization of molars was highest in Model 2 and lowest in Model 3. In clear aligner treatment combined with Class II elastics, HTLA was more effective in controlling mandibular incisor proclination and mesial tipping of mandibular molars. The slit cutout models were more effective in controlling mesial tipping of mandibular molars.

ARTICLE INFO

Article history:
Received 5 February 2024
Revised 14 March 2024
Accepted 10 April 2024

Keywords:
Clear aligner
Class II elastics
Incisor
Dentition
Finite element analysis

1. Introduction

Class II malocclusion is one of the most important reasons why patients seek orthodontic treatment and many different techniques can be preferred for its treatment; the use of intermaxillary elastics is one of these options as mentioned by Jones et al. (2008). In a recent study by Liu et al. (2022), intermaxillary elastics play an important role in the correction of many malocclusions, especially Class II malocclusions. Although CIIe has been demonstrated to provide beneficial effects, including anchorage support and the prevention of mesialization of maxillary posterior teeth, it has also been reported by Nelson et al. (2007) and Janson et al. (2013) that it can cause undesirable side effects, such as the proclination of mandibular anterior teeth. As stated by Patter-son et al. (2021), the use of ClIe in fixed orthodontic treatments inevitably results in loss of anchorage and reciprocal force transmission to the mandibular anterior teeth. This may cause side effects such as alveolar defects, fenestration and dehiscence, especially in patients with thin cortical bone in the lower anterior region, as reported by Evangelista et al. (2010). Therefore, to avoid these side effects, many researchers (Celikoglu et al 2016; Unal et al. 2015; Aslan et al. 2014; Luzi and Luzi 2013; Turkkahraman et al. 2016) have used various methods, such as utilizing skeletal anchorage devices and increasing the anchorage of the dental units involved.

In recent years, clear aligner treatment (CAT) has been preferred among patients seeking orthodontic treatment due to its ease and aesthetic features, and its treatment efficacy has increased with current develop-

* *Corresponding author*. E-mail address: nurverkarsli@ktu.edu.tr (N. Karslı)
ISSN: 2149-8024 / DOI: https://doi.org/10.20528/cjsmec.2024.02.003

ments, as reported in a study by Rossini et al. (2015). As Patterson et al. (2021) and Caruso et al. (2019) mentioned, CIIe can be applied from buttons adhered on the teeth or slit cutouts prepared on the aligner in CAT. According to Staderini et al. (2022), the side effects caused by CIIe, such as mandibular incisor proclination and posterior rotation of the palatal plane, can be compensated to some extent under clinical conditions because the aligners cover all teeth as a unit. However, further specific information is required on the study of the maxillary and mandibular dental arch in a force system that is complex.

The clinical results (Elkholy et al. 2019; Elshazly et al. 2022; Liu and Chen 2015) obtained in CAT are affected by many parameters such as the trimline extension of the aligner, the aligner material, the thickness of the aligner, the use of attachments, and the design of the attachment. Elhazy et al. (2022) found that high trimline aligner (HTLA) extending over the gingiva produced higher forces on the teeth. However, the trimming lines of ClearCorrect® aligners are designed to be straight and high, and this design has been scientifically proven to provide more accurate tooth movement and effective root control in a study by Elshazly et al. (2022). The study by Nicera et al. (2022) showed that the use of attachments increased the effectiveness of mesio-distal movements and that better anchorage of posterior teeth was obtained by increasing the number of attachments applied to the posterior teeth.

Finite element analysis (FEA) is a computational engineering method used to determine tooth displacements after the application of external forces. In recent years, FEA studies (Wang et al. 2022; Rossini et al. 2020) have been used in orthodontics to prove effective means of stimulating tooth movement patterns.

There is a lack of information in the literature regarding the effect of CAT with the use of CIIe, especially on the possible mandibular anterior teeth. Therefore, the aim of this current study was to evaluate the effects of different trimline extensions of the aligners and the application of elastic force through button or slit cutouts on the mandibular dentition in CAT combined with CIIe using FEA.

2. Materials and Methods

2.1. Model creation

The 3D mesh structure was arranged and mathematically transformed into a solid mesh structure. The generation of 3D FEA models and analysis were conducted on HP workstations equipped with INTEL Xeon E-2286 processors operating at a frequency of 2.40 GHz and 64 GB ECC memory.

The 3D Slicer Software was used to get the 3D model (.stl) of the bone structure using the CBCT data. The ANSYS SpaceClaim software was used for reverse engineering and 3D CAD activities. In addition, the adaptation of solid models to the analysis environment and optimized mesh creation activities were carried out with ANSYS Workbench software. LS-DYNA solver was used to solve the finite element models. The dimensions and cutout modifications of the aligner were based on the ClearCorrect® system.

2.2. Cortical bone, trabecular bone, teeth, and periodontal ligament

Pre-existing CBCT data from an adult patient with Class II malocclusion with complete dentition was used to obtain the bone model used in this study. The thickness of every CBCT slice was adjusted to 0.10 mm. The CBCT data, formatted as DICOM, was partitioned based on suitable Hounsfield values using the 3DSlider program. Subsequently, the data was transformed into a three-dimensional model by segmentation. The threshold procedure was used to create mask layers of maxillary and mandibular bone, tooth structure, mandible and temporomandibular joint (TMJ).

The 3D model was imported into the ANSYS SpaceClaim software, where the maxillary and mandibular cortical bone and tooth geometry were modeled. The trabecular bone has been obtained by reference the inside of the 3D mandibular cortical bone. The disc was modeled using an anatomic structure. A periodontal ligament model with a thickness of 0.25 mm was created using the outer surface of the dentin model. All the prepared models were placed in the correct coordinates in 3D space in ANSYS SpaceClaim software and the modeling process was completed (Fig. 1). Vertical rectangular attachments (2×3×1 mm) on the buccal surface of the lower canine and premolar teeth were added for retention.

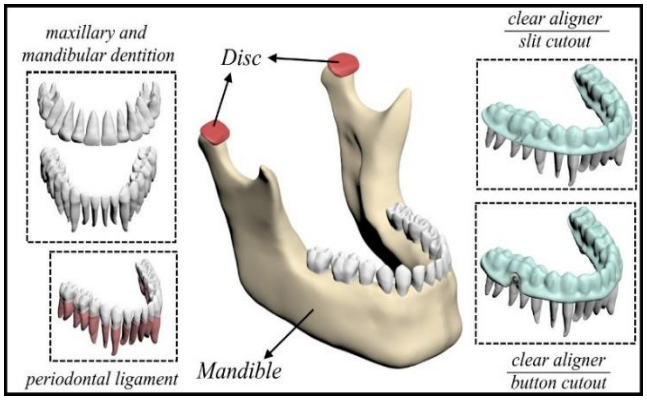

Fig. 1. Different components of the model.

2.3. Creating analysis models from the original 3D model

The button used in this study was modeled in ANSYS SpaceClaim software. Two main models as button and slit cutout were designed. Each of the main models were designed to the 0.76 mm thick aligners as HTLA (straight and high trimline that extends 2 mm above the gingival margin) and LTLA (straight and low trimline that extends 0.5 mm above the gingival margin). Thus, four different models were prepared for analysis (Fig. 2). The modifications of the prepared models are given in Table 1.

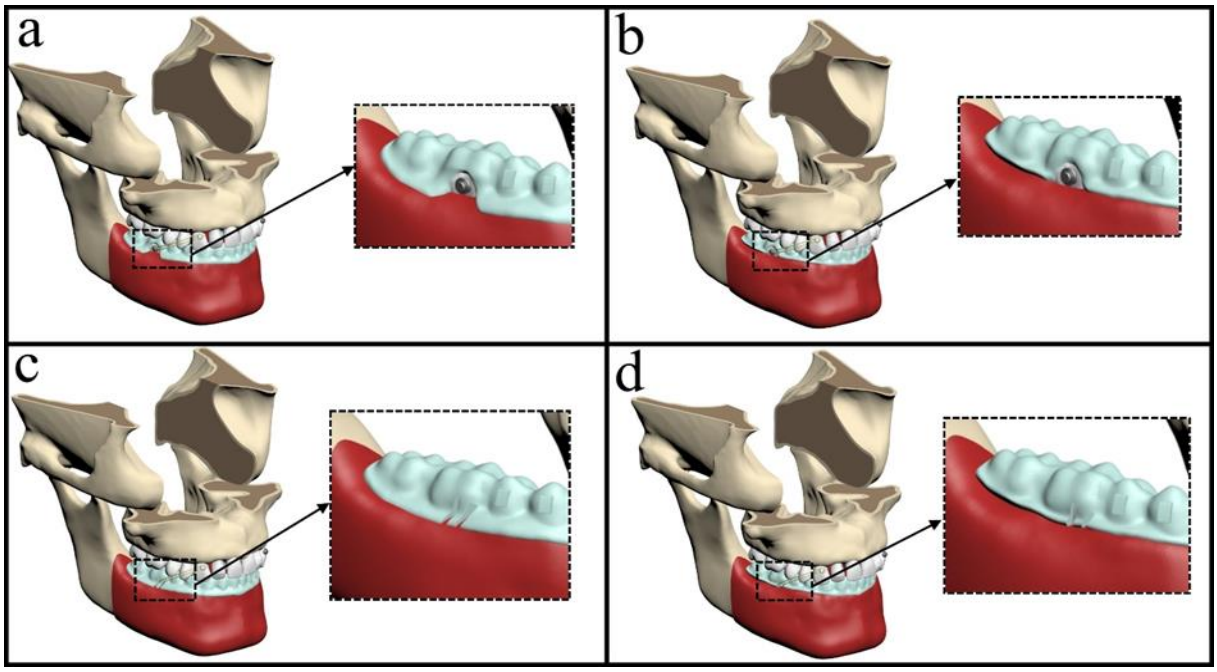

Fig. 2. Finite element models:
(a) Model 1 (straight and high trimline aligner (HTLA) model with elastic applied through button);
(b) Model 2 (straight and low trimline aligner (LTLA) model with elastic applied through button;
(c) Model 3 (HTLA model with elastic applied through slit cutout);
(d) Model 4 (LTLA model with elastic applied through slit cutout).
The black square areas represent close-up views the aligner cutout and the aligner trimline extension.

Table 1. Modifications of the models.

Models	Trimline extension	Aligner cutouts
Model 1	High	Button
Model 2	Low	Button
Model 3	High	Slit
Model 4	Low	Slit

2.4. Obtaining mathematical models

Mathematical models were created by partitioning geometric models into discrete and compact parts referred to as meshes. The modeling procedure was conducted using ANSYS SpaceClaim software, while the models were generated mathematically using ANSYS Workbench software. Subsequently, the models were prepared for analysis. The mathematical models created in ANSYS Workbench software were transferred to the LS-DYNA solver for analysis.

2.5. Material properties

The material properties of the investigated model are quantitatively specified in Table 2. The examinations used linear material properties, including the elastic modulus and Poisson's ratio.

Table 2. Linear material properties.

Material	Elastic modulus (MPa)	Poisson's ratio (ν)
Cortical Bone (Liu et al. 2022; Chen et al. 2019)	1.37×10^4	0.26
Trabecular Bone (Liu et al. 2022; Chen et al. 2019)	1.37×10^3	0.30
Tooth (Liu et al. 2022, 2023)	1.96×10^4	0.30
PDL (de Oliveira et al. 2020; Li et al. 2006)	6.9×10^{-1}	0.45
Mucosa (Hohmann et al. 2007)	2.8	0.40
Button (Liu et al. 2023; Ammar et al. 2011)	1.14×10^5	0.35
CA (Liu et al. 2022, 2023)	5.28×10^2	0.36
Attachments (Liu et al. 2022, 2023)	1.25×10^4	0.36
Condylar cartilage (Liu et al. 2022, 2023)	8×10^{-1}	0.30
Disc (Liu et al. 2022, 2023)	1.8×10^{-1}	0.40

***PDL, periodontal ligament; CA, clear aligner.

2.6. Loading and boundary conditions

A force of 120 g (~1.177 N) was applied to maxillary canines and mandibular first molars by CIIe.

In the slit cutout models; a total force of 120 g was applied from the slit cutout on the aligner to the button on the maxillary canine. In button cutout models; a load representing 120 g of force was applied from the button on the maxillary canine to the button on the mandibular first molar.

The models were bound at the nodal points in the upper part of the maxillary bones, thereby constraining all degrees of freedom to prohibit any movement in the three axes. A total of six nonlinear static analyses were conducted on six analysis models, with the force and boundary conditions indicated. Based on the boundary criteria, the lower border of the mandible is immobilized and the upper region is restricted the movement of the maxillary and temporal structures. The attachment contact was set at the interfaces from cancellous bone to cortical bone, cortical bone to PDL, PDL to tooth and tooth to attachment. This bonding prevented any movement between the contact surfaces. Furthermore, the joints between the teeth were not separated at their interfaces, allowing some frictionless sliding along the contact surfaces. In order to be able to apply the analysis in the mathematical models created and to obtain accurate results, the surface relations between the parts must be defined in the analysis program.

A nonlinear frictional contact with a coefficient $\mu = 0.2$ was set at the aligner-tooth and aligner-attachment interfaces. The tooth-PDL, tooth-attachment, and cortical and trabecular bone-PDL contact areas were designated as bonded-type contact. This approach is based on the assumption that the parts move with full correlation during their movement. The mesh structure and boundary condition of model were shown in Fig. 3.

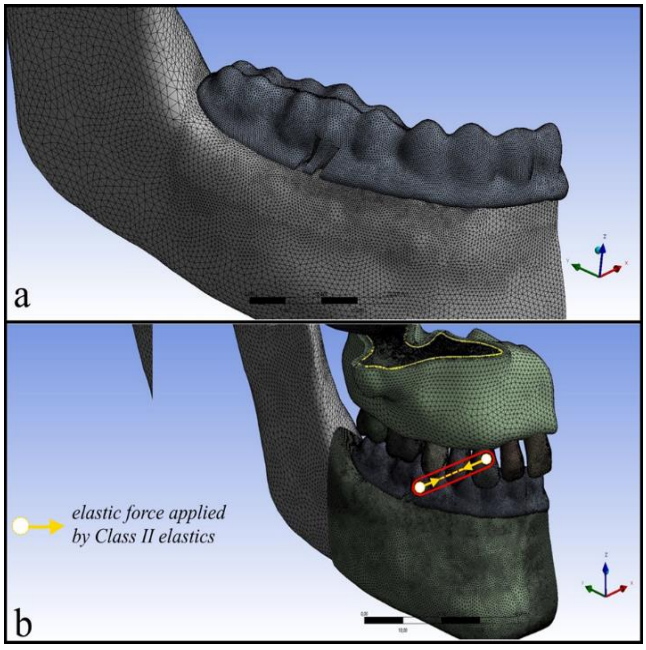

Fig. 3. (a) Mesh structure; (b) Global coordinate and boundary condition of model.

2.7. Outcomes

The global coordinate system shown in Fig. 3 was created for the mandibular tooth structure. In this system, the *x*-axis relates to the coronal plane, with positive values indicating the left side and negative values indicating the right side. The *y*-axis indicates the sagittal plane, with positive values indicating the posterior direction and negative values indicating the anterior direction. Lastly, the *z*-axis indicates the vertical plane, with positive values indicating the superior direction and negative values indicating the inferior direction. Each tooth was assigned a local coordination system, with the *x*-axis indicating the mesial direction (+) and the distal direction (-), the *y*-axis indicating the lingual direction (+) and the buccal direction (-), and the positive direction on the *z*-axis being indicated by the apex of the mandibular teeth and the incisor/occlusal of the mandibular teeth.

2.8. Quantitative model information

The mesh properties created in the prepared analysis models are given in Table 3. In all models, mesh quality was checked for the triangles that have skewness > 80°, and minimum length of 0.001. Failed meshes were edited accordingly.

Table 3. Nodes and elements.

Models	Nodes	Elements
Model 1	415551	1528465
Model 2	422270	1553124
Model 3	412867	1517856
Model 4	419153	1540841

3. Results

3.1. Aligner deformation

During the mesialization of the mandibular arch with CIIe force, different behaviors and force systems were recorded among the simulations performed. Data for maximum and minimum aligner deformation are given in Appendix A and Figs. 4(a-d). The maximum aligner deformation among the models was observed in Model 3 (slit cutout-high) in the region of the slit cutout of the first molar (0.0817 mm). The maximum aligner deformation was concentrated on the buccal slit cutout region of the first molars in Models 3 and 4, on the mesiobuccal cusp region of the first molars in Models 1 and 2, while the minimum aligner deformation was observed on the bucco-gingival region of the canine teeth in all models.

3.2. Three-dimensional movement of the mandibular dentition

The displacement of the teeth has been recorded according on the global coordinate system. The movement of the mandibular dentition occurred mostly in the sag-

ittal plane toward the *y*-axis. The mandibular dentition of all models moved forward with extrusion tendency of molars and intrusion of anterior teeth due to the CIIe force (Figs. 5(a-d) and Appendix B).

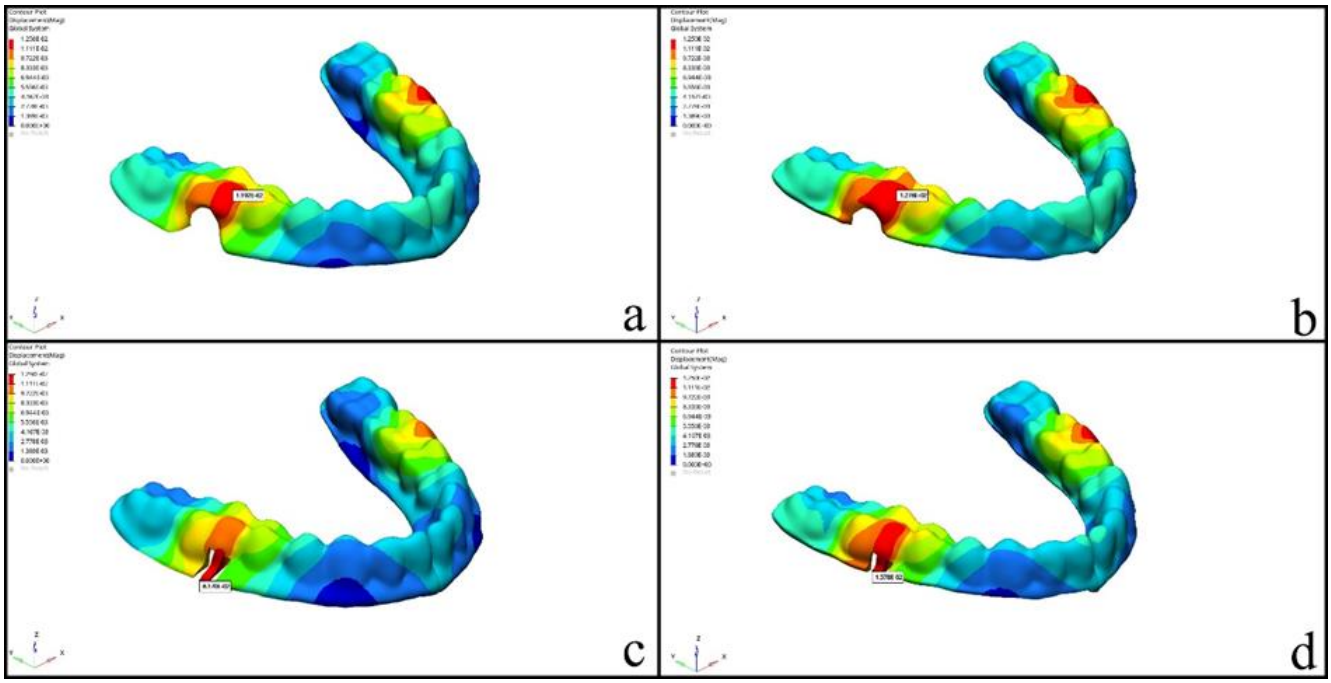

Fig. 4. Clear aligner deformation values:
(a) Model 1 (straight and high trimline aligner (HTLA) model with elastic applied through button);
(b) Model 2 (straight and low trimline aligner (LTLA) model with elastic applied through button);
(c) Model 3 (HTLA model with elastic applied through slit cutout);
(d) Model 4 (LTLA model with elastic applied through slit cutout).

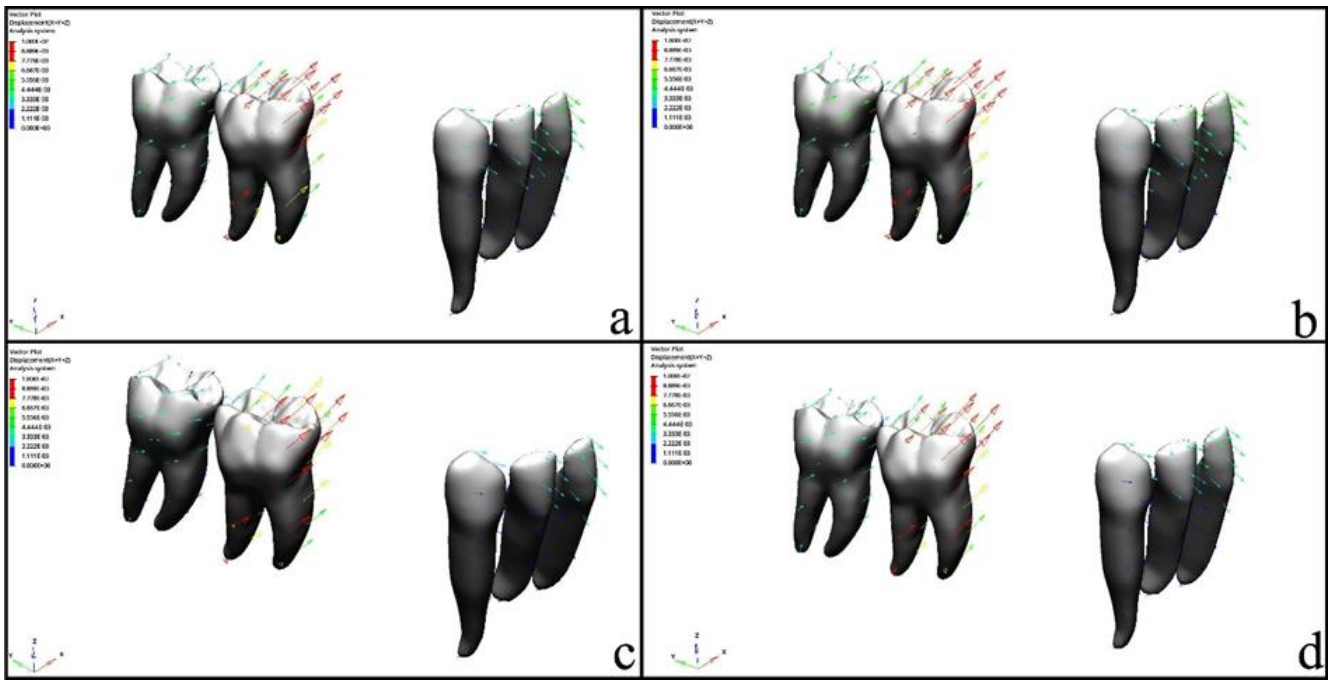

Fig. 5. The directional inclination of the lower teeth in models that received Class II elastics:
(a) Model 1 (straight and high trimline aligner (HTLA) model with elastic applied through button);
(b) Model 2 (straight and low trimline aligner (LTLA) model with elastic applied through button;
(c) Model 3 (HTLA model with elastic applied through slit cutout);
(d) Model 4 (LTLA model with elastic applied through slit cutout).

3.3. Three-dimensional displacement of mandibular anterior teeth

The 3D displacements of the mandibular anterior teeth in all models are shown in Appendix B and Figs. 6(a-d).

Mandibular central and lateral incisors;

In the mesio-distal direction (*x*-axis), the crown exhibited mesial movement and the root exhibited distal movement in all models. Among all models, the highest movement was observed in Models 1 and 2 (L1, 0.0010; L2, 0.0012 mm), and the least movement was observed in Model 4 (L1, 0.0007; L2, 0.0010 mm).

In the labio-lingual direction (*y*-axis), the crown exhibited buccal movement and the root exhibited lingual movement in all models. Among all models, the greatest labial crown movement was observed in Model 2 (L1, 0.0044; L2, 0.0039 mm), and the least labial movement was observed in Model 3 (L1, 0.0032; L2, 0.0027 mm).

In the supero-inferior direction (*z*-axis), the crown and root moved inferiorly (intrusion) in all groups. Among all groups, the highest inferior movement was observed in Model 4 (L1, 0.0025; L2, 0.0018 mm), and the least in Model 3 (L1, 0.0017; L2, 0.0011 mm).

Mandibular canines;

In the *x*-axis, the crown moved mesially and the root moved distally in all models. Among all models, the maximum mesial movement of the crown was observed in Model 2, (0.0025 mm), and the minimum mesial movement was observed in Model 3 (0.0020 mm).

In the *y*-axis, the crown moved buccally and the root moved lingually in all models. Among all models, the most labial crown movement was observed in Model 2 (0.0029 mm), and the least buccal crown movement was observed in Model 3 (0.0019 mm).

In the *z*-axis, the crown and root moved inferiorly in all models. Among all models, the most inferior movement was observed in Model 2 (0.0007 mm), while the least inferior movement was observed in Model 3 (0.0003 mm).

3.4. Three-dimensional displacement of mandibular molars

The 3D displacements of the mandibular molars in all models are shown in Appendix B and Figs. 6(a-d).

Mandibular first molars;

In the bucco-lingual direction (*x*-axis), lingual tipping with mesiolingual rotation was observed in all models. Among all models, the highest amount of lingual tipping with rotation was observed in Model 2 (0.0100 mm) and, the least in Model 3 (0.0083 mm).

In the mesio-distal direction (*y*-axis), mesial displacement was observed in all models. The greatest mesial displacement was observed in Model 2 (0.0042 mm), followed by Model 1 and Model 4, respectively. The least mesial displacement was found in Model 3 (0.0028).

In the supero-inferior direction (*z*-axis), the crown and root moved superiorly (extrusion) in all models. Among all models, the highest extrusion movement was observed in Model 4 (0.0052 mm), and the least in Model 3 (0.0015 mm).

Mandibular second molars;

In the *x*-axis, lingual tipping with mesiolingual rotation was observed in all models. The highest amount of lingual tipping with rotation was observed in Model 2 (0.0016 mm), and the lowest in Model 3 (0.0010 mm).

In the *y*-axis, the crown and root moved mesially in all models, with a higher displacement in the crown. The highest mesial displacement was observed in Model 2 (0.0037 mm), and the lowest in Model 3 (0.0029 mm).

In the z*x*-axis, the crown and root were displaced superiorly (extrusion) in all models. Among all models, the highest extrusion movement was observed in Model 2 (0.0029 mm) and the lowest in Model 3 (0.0019 mm).

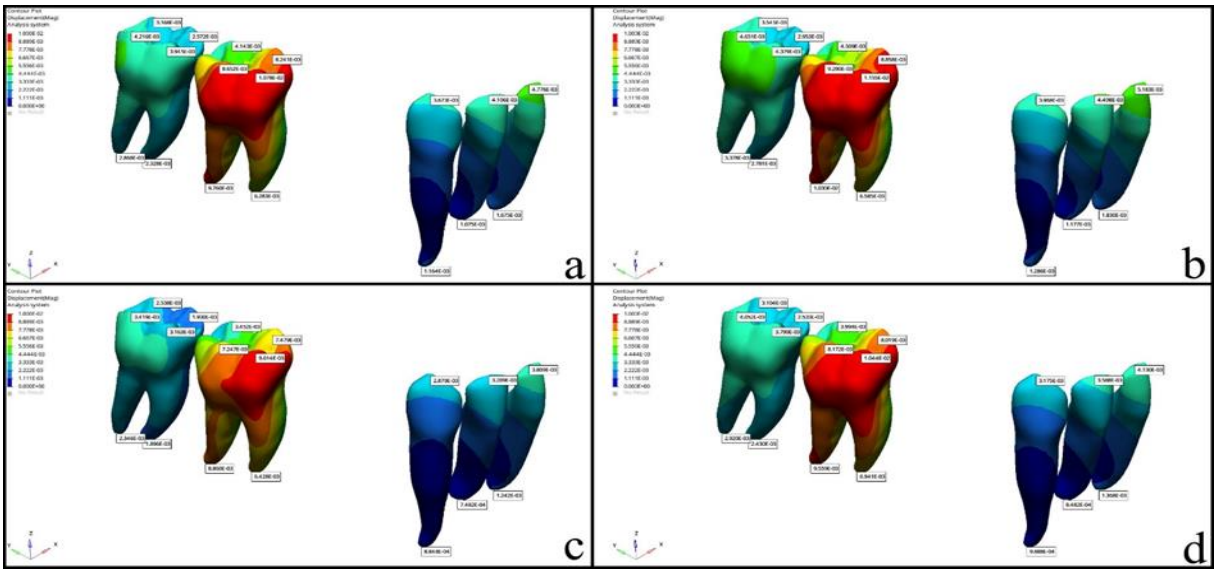

Fig. 6. A propensity for three-dimensional displacement of the mandibular dentition in Class II elastic models:
(a) Model 1 (straight and high trimline aligner (HTLA) model with elastic applied through button);
(b) Model 2 (straight and low trimline aligner (LTLA) model with elastic applied through button;
(c) Model 3 (HTLA model with elastic applied through slit cutout);
(d) Model 4 (LTLA model with elastic applied through slit cutout).

3.5. Stress distribution

The stress distribution values and regions occurring in the PDL are presented in Appendix C and Figs. 7(a-d).

In all models, maximum stress values were observed at the buccal root of the maxillary first molars and the highest PDL stress was found in Model 4 (0.0150 MPa).

The highest PDL stress was concentrated in the labial and cervical region of the incisors, and the highest stress was found in Model 2 (L1, 0.0046 MPa; L2, 0.0040 MPa) among all models.

The maximum PDL stress was found to be concentrated in the lingual and cervical region of the canines, and the highest stress was observed in Model 2 (0.0038 MPa) among all models.

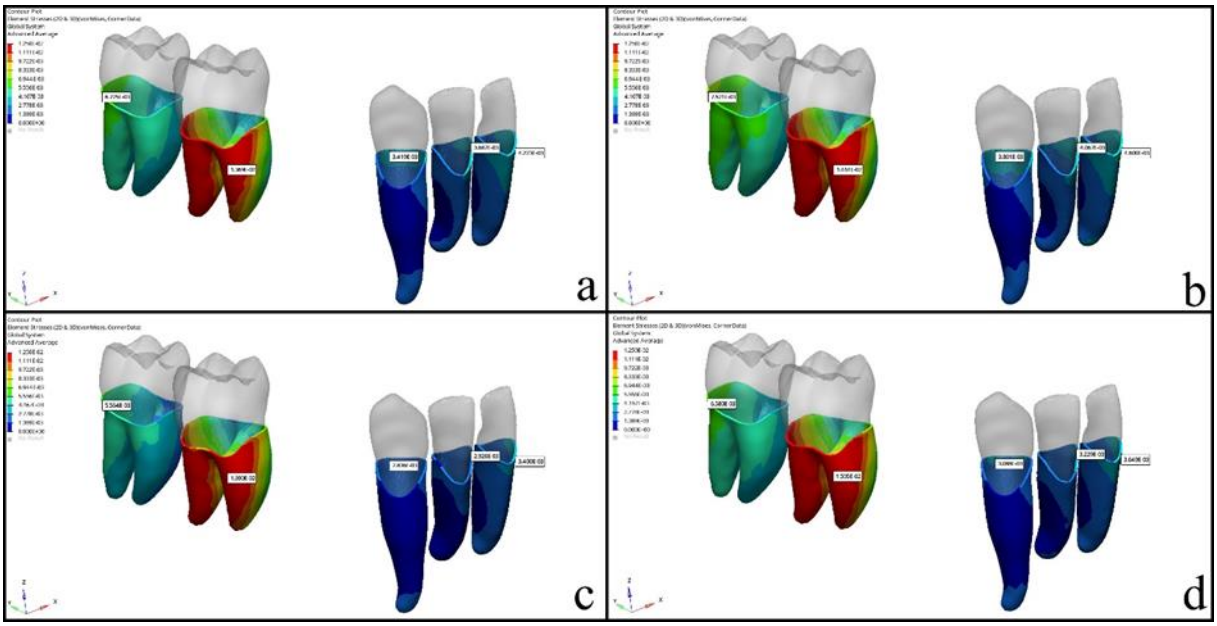

Fig. 7. The stress distribution of PDL:
(a) Model 1 (straight and high trimline aligner (HTLA) model with elastic applied through button);
(b) Model 2 (straight and low trimline aligner (LTLA) model with elastic applied through button;
(c) Model 3 (HTLA model with elastic applied through slit cutout);
(d) Model 4 (LTLA model with elastic applied through slit cutout).

4. Discussion

The popularity of CAT has been increasing due to its significant advantages, including cosmetic and comfort benefits. Along with the developing aligner industry, different aligner designs are also gaining attention in the industry, and one of these variables is the trimline extension of the aligners. Previous experimental studies (Elshazly et al. 2022; Cowley 2012; Brown 2021; Gao and Wichelhaus 2017) have also reported the importance of the trimline design and extension of aligners for orthodontic treatment planning.

In aligner therapy of some complex cases, additional mechanics such as ClIe may be required for additional anchorage. At this point, the factor of where to apply the intermaxillary elastics comes to the fore; the elastics can be applied through the precision cutouts designed on the aligner or through the buttons added on the teeth. Liu et al. (2022) also reported that CIIe applied through slit cutouts transfers the force directly through the aligner and elastic force applied through buttons transfers the force directly to the tooth where the button is applied and then spreads it to the other teeth. In addition, intermaxillary elastics combined with CAT can effectively correct the sagittal relationship and have many positive contributions in terms of anchorage and treatment time. However, the number of studies investigating the effects of CAT combined with CIIe on the mandibular dentition is quite limited. In the light of all this information, our study investigates the effects of the area of application of the elastics and the trimline extension of the aligners on the mandibular arch in CAT combined with CIIe.

FEA is a mathematical method that can precisely evaluate the changes in complex geometric shapes and the stresses and strains that occur on them, which is frequently used in orthodontics. Studies in the literature (Kucukkurt 2019; Knop et al. 2015) have also indicated that FEA is an effective method for precisely measuring changes in teeth and VMS.

In previous research conducted by Liu et al. (2023), it was demonstrated that correcting the molar relationship using CIIe combined with CAT involved moving the maxillary molars posterior and the mandibular molars forward. In our study, mesialization was observed in mandibular molar teeth with the effect of the force applied with CIIe. The force vector of CIIe applied through the button on the buccal side of the mandibular molar or through the slit cutouts on the aligner can be divided into lingual and superior components, with the mesial force being greater in the study by Liu et al. (2022). Therefore,

lingual tipping with mesio-lingual rotation was observed in mandibular molars in this study. Liu et al. (2022) found that CIIe applied through the button provided more effective molar mesialization than those applied through the slit cutout. They attributed this to the fact that mandibular molar mesialization was greater with the force applied directly to the tooth from the button. Furthermore, the results obtained in the present study are consistent with these findings. It was seen that models with slit cutout and high trimline extension provided more control over mesial tipping and rotation during mesial movement of the first molars. The improved control of tooth movement observed in the high trimline and slit cutout models can be attributed to the optimization of forces resulting from the expanded surface area over which the force is transmitted by the high trimline aligners, as well as the utilization of elastics through the slit cuts to ensure that the force is not directly applied to the tooth, thereby optimizing force distribution. Moreover, the increased mesial rotation observed in the button models can be attributed to the presence of a gap between the aligners and teeth. This gap is further exacerbated when the aligner fit is inadequate particularly in patients where the aligners are not tracking properly. Hence, this gap would prevent the aligner to overcome the mesial rotation effect of Clle, when applied through a button. It can be proposed that greater control over overturning in the slit-cutout and high trimline model can be attributed to the fact that the force applied by the CIIe is directed towards the centre of resistance of the tooth.

Previous studies (Nelson et al. 2005; Janson et al. 2013) have shown that the use of CIIe causes some side effects such as undesirable proclination of the mandibular anterior teeth. In our study, labial tipping of the mandibular incisors was observed to varying degrees in all models and it was found that labial tipping of the mandibular incisors was higher in models with a low trimline extension. This information allows us to interpret that incisor proclination may be more controllable in treatment with aligners with a high trimline extension. In addition, Liu et al. (2022) reported that additional optimized torque designs can be planned for the control of the proclination of the mandibular anterior teeth.

The proclination of the mandibular anterior teeth leads to the concentration of strains on the periodontal ligament (PDL) and alveolar bone in the cervical region of the labial surface. Some investigators reported an increased risk of root resorption due to the pressure on the PDL exceeding the capillary pressure in the area and impaired blood flow. Furthermore, previous studies (Hohmann et al. 2007; Dorow and Sander 2005) showed that the PDL pressure threshold involved in root resorption is 0.047 MPa. Although none of the models exceeded this threshold for PDL stress, this threshold was relatively close, especially in the low LTLA and button cutout model (0.0046 MPA). This may be attributed to the fact that low trimline extension aligners are less effective in controlling the proclination of mandibular anterior teeth. Moreover, PDL stress values were measured to be lower in slit cutout models than in button models.

Although FEA is a widely used technology for biomechanical analysis of applied forces in orthodontics, it is inevitable to say that it has some limitations. Although it is possible to optimally adjust the magnitude and vector of the applied force initially, the direction and intensity of the force are constantly changing with tooth movement during clinical practice. Furthermore, these models cannot take into account complex masticatory pressures and bone remodeling. On the other hand, in this FEA study (Tanne et al. 1987), the PDL thickness was assumed to be constant; however, the PDL varies in thickness along the tooth root. In their study, Hohmann et al. (2011) suggested that this nonlinear change in PDL thickness changes the elastic modulus of the PDL, which in turn affects the VMS values. Therefore, clinical studies evaluating the effects of CIIe applied with aligners on mandibular anterior teeth are needed and future studies should investigate the dynamic behavior of the dentition when using CAT in combination with CIIe.

In terms of the clinical importance of these findings, it can be stated that utilizing a Clle with buttons is a preferable option for patients with short crowns. However, it does have the drawbacks of inducing tipping and mesial rotation. Hence, it might be imperative to incorporate anti-rotation movement to the lower molars in patients who would necessitate prolonged use of Clle.

5. Conclusions

Clear aligners with high trimline extension were found to be more effective in controlling lower anterior teeth. Less mesial movement was observed in mandibular molars due to increased aligner deformation by ClIe applied through slit cutouts. The presence of high trimline aligners and the application of CIIe from the slit cutout were found to increase the control of mesial tipping of mandibular molars.

Appendix A. Aligner deformation and location

Aligner deformation	Maximum deformation (mm)	Localization	Minimum deformation (mm)	Localization
Model 1	0.0119	Mesio-buccal cusp of mandibular first molar	0	Bucco-gingival edges of canine
Model 2	0.0127	Mesio-buccal cusp of mandibular first molar	0.0013	Bucco-gingival edges of canine
Model 3	0.0817	Slit cutout region of mandibular first molar	0	Bucco-gingival edges of canine
Model 4	0.0157	Slit cutout region of mandibular first molar	0	Bucco-gingival edges of canine

Appendix B. Three-dimensional displacement of mandibular teeth

Tooth	Axes	*x*-axis				*y*-axis				*z*-axis			
	Models	1	2	3	4	1	2	3	4	1	2	3	4
Central incisor	C	0.0010	0.0010	0.0008	0.0007	-0.0040	-0.0044	-0.0032	-0.0036	-0.0023	-0.0025	-0.0017	-0.0018
	R	-0.0003	-0.0003	-0.0002	-0.0002	0.0014	0.0015	0.0010	0.0012	-0.0008	-0.0008	-0.0005	-0.0005
Lateral incisor	C	0.0012	0.0012	0.0010	0.0010	-0.0035	-0.0039	-0.0027	-0.0031	-0.0016	-0.0018	-0.0011	-0.0013
	R	-0.0003	-0.0003	-0.0025	-0.0002	0.0008	0.0009	0.0006	0.0007	-0.0005	-0.0005	-0.0002	-0.0003
Canine	C	0.0024	0.0025	0.0020	0.0020	-0.0026	-0.0029	-0.0019	-0.0024	-0.0006	-0.0007	-0.0003	-0.0003
	R	-0.0007	-0.0007	-0.0006	-0.0006	0.0008	0.0009	0.0005	0.0007	-0.0003	-0.0003	-0.0000	-0.0001
First molar	CMB	0.0093	0.0100	0.0083	0.0088	-0.0032	-0.0033	-0.0020	-0.0025	0.0042	0.0046	0.0043	0.0049
	CML	0.0080	0.0086	0.0071	0.0076	-0.0003	-0.0003	0.0005	0.0001	0.0016	0.0018	0.0020	0.0025
	CDB	0.0059	0.0063	0.0051	0.0054	-0.0040	-0.0042	-0.0028	-0.0034	0.0048	0.0052	0.0042	0.0049
	CDL	0.0035	0.0038	0.0030	0.0033	-0.0007	-0.0007	0.0000	-0.0003	0.0019	0.0021	0.0015	0.0022
	AM	-0.0031	-0.0031	-0.0020	-0.0022	-0.0033	-0.0033	-0.0042	-0.0043	0.0043	0.0046	0.0043	0.0049
	AD	-0.0065	-0.0068	-0.0051	-0.0054	-0.0048	-0.0049	-0.0056	-0.0057	0.0053	0.0058	0.0044	0.0053
Second molar	CMB	0.0013	0.0016	0.0010	0.0013	-0.0033	-0.0035	-0.0027	-0.0031	0.0015	0.0019	0.0011	0.0016
	CML	0.0009	0.0011	0.0007	0.0009	-0.0016	-0.0017	-0.0011	-0.0014	0.0017	0.0021	0.0013	0.0018
	CDB	-0.0003	-0.0003	-0.0005	-0.0003	-0.0035	-0.0037	-0.0029	-0.0033	0.0022	0.0026	0.0017	0.0023
	CDL	-0.0009	-0.0008	-0.0010	-0.0008	-0.0016	-0.0017	-0.0012	-0.0014	0.0025	0.0029	0.0019	0.0025
	AM	0.0003	0.0003	0.0002	0.0003	-0.0011	-0.0013	-0.0010	-0.0012	0.0019	0.0024	0.0015	0.0020
	AD	-0.0006	-0.0007	-0.0006	-0.0006	-0.0013	-0.0015	-0.0012	-0.0013	0.0024	0.0029	0.0018	0.0024

C, crown; R, root; CMB, mesiobuccal cusp; CML, mesiolingual cusp; CDB, distobuccal cusp; CDL, distolingual cusp; AM, Mesial root apex; AD, distal root apex.

Appendix C. von Mises stress values and distribution in the mandibular dentition

Models	PDL stress	Maximum value (MPa)	Localization	Minimum value (MPa)	Localization
Model 1	Central Incisor	0.0042	Bucco-gingival root surface	0	Disto-apical root surface
	Lateral Incisor	0.0036	Bucco-gingival root surface	0	Disto-lingual root surface
	Canine	0.0034	Linguo-gingival root surface	0	Buccal root surface
	First Molar	0.0136	Buccal root surface	0.001	Cervico-lingual root surface
	Second Molar	0.0067	Disto-gingival root surface	0.001	Mesio-lingual root surface
Model 2	Central Incisor	0.0046	Bucco-gingival root surface	0	Disto-apical root surface
	Lateral Incisor	0.0040	Bucco-gingival root surface	0	Disto-lingual root surface
	Canine	0.0038	Linguo-gingival root surface	0	Buccal root surface
	First Molar	0.0146	Buccal root surface	0.001	Cervico-lingual root surface
	Second Molar	0.0075	Disto-gingival root surface	0.001	Mesio-lingual root surface
Model 3	Central Incisor	0.0034	Bucco-gingival root surface	0	Disto-apical root surface
	Lateral Incisor	0.0029	Bucco-gingival root surface	0	Disto-lingual root surface
	Canine	0.0028	Linguo-gingival root surface	0	Buccal root surface
	First Molar	0.0139	Buccal root surface	0	Cervico-lingual root surface
	Second Molar	0.0055	Disto-gingival root surface	0	Mesio-lingual root surface
Model 4	Central Incisor	0.0036	Bucco-gingival root surface	0	Disto-apical root surface
	Lateral Incisor	0.0032	Bucco-gingival root surface	0	Disto-lingual root surface
	Canine	0.0030	Linguo-gingival root surface	0	Buccal root surface
	First Molar	0.0150	Buccal root surface	0.001	Cervico-lingual root surface
	Second Molar	0.0065	Disto-gingival root surface	0.001	Mesio-lingual root surface

Acknowledgements

The authors would like to thank Tinus Technologies, ClearCorrect and its employees for their technical contributions, and Dr. Arda Dilgiloğlu and Assoc. Prof. Dr. Hüccet Kahramanzade for sharing their knowledge and experience.

Funding

The authors received no financial support for the research, authorship, and/or publication of this manuscript.

Conflict of Interest

The authors declared no potential conflicts of interest with respect to the research, authorship, and/or publication of this manuscript.

Author Contributions

All of the authors made substantial contributions to conception and design, or acquisition of data, or analysis and interpretation of data; were involved in drafting the manuscript or revising it critically for important intellectual content; and gave final approval of the version to be published.

Data Availability

The datasets created and/or analyzed during the current study are not publicly available, but are available from the corresponding author upon reasonable request.

REFERENCES

Ammar HH, Ngan P, Crout RJ, Mucino VH, Mukdadi OM (2011). Three-dimensional modeling and finite element analysis in treatment planning for orthodontic tooth movement. *American Journal of Orthodontics and Dentofacial Orthopedics*, 139(1), e59–71.

Aslan BI, Kucukkaraca E, Turkoz C, Dincer M (2014). Treatment effects of the Forsus Fatigue Resistant Device used with miniscrew anchorage. *The Angle Orthodontist*, 84(1), 76-87.

Brown BE (2021). Effect of Gingival Margin Design on Clear Aligner Material Strain and Force Delivery. Thesis. University of Minnesota.

Caruso S, Nota A, Ehsani S, Maddalone E, Ojima K, Tecco S (2019). Impact of molar teeth distalization with clear aligners on occlusal vertical dimension: a retrospective study. *BMC Oral Health*, 19(1), 182.

Celikoglu M, Buyuk SK, Ekizer A, Unal T (2016). Treatment effects of skeletally anchored Forsus FRD EZ and Herbst appliances: A retrospective clinical study. *The Angle Orthodontist*, 86(2), 306-314.

Chen X, Mao B, Zhu Z, Yu J, Lu Y, Zhang Q, Yue L, Yu H (2019). A three-dimensional finite element analysis of mechanical function for 4 removable partial denture designs with 3 framework materials: CoCr, Ti-6Al-4V alloy and PEEK. *Scientific Reports*, 9(1), 13975.

Cowley DP (2012). Effect of Gingival Margin Design on Retention of Thermoformed Orthodontic Aligners. Thesis. University of Nevada.

de Oliveira JC, Sordi MB, da Cruz ACC, Zanetti RV, Betiol EAG, Vieira SR, Zanetti AL (2020). Number of dental abutments influencing the biomechanical behavior of tooth–implant-supported fixed partial dentures: A finite element analysis. *Journal of Dental Research, Dental Clinics, Dental Prospects*, 14(4), 228-234.

Dorow C, Sander FG (2005). Development of a model for the simulation of orthodontic load on lower first premolars using the finite element method. *Journal of Orofacial Orthopedics / Fortschritte der Kieferorthopädie*, 66(3), 208-218.

Elkholy F, Mikhaiel B, Repky S, Schmidt F, Lapatki BG (2019). Effect of different attachment geometries on the mechanical load exerted by PET G aligners during derotation of mandibular canines. J*ournal of Orofacial Orthopedics / Fortschritte der Kieferorthopädie*, 80(6), 315-326.

Elshazly T, Salvatori D, Bourauel C, Elattar H, Alkabani Y. (2022). Effect of thickness and material type of orthodontic aligners on force transmission: An in vitro study using pressure-sensitive films. *SSRN*, 4270102.

Elshazly TM, Keilig L, Salvatori D, Chavanne P, Aldesoki M, Bourauel C (2022). Effect of trimming line design and edge extension of orthodontic aligners on force transmission: An in vitro study. *Journal of Dentistry*, 125, 104276.

Evangelista K, Vasconcelos K de F, Bumann A, Hirsch E, Nitka M, Silva MAG (2010). Dehiscence and fenestration in patients with Class I and Class II Division 1 malocclusion assessed with cone-beam computed tomography. *American Journal of Orthodontics and Dentofacial Orthopedics*, 138(2), 133.e1-133.e7.

Gao L, Wichelhaus A (2017). Forces and moments delivered by the PET-G aligner to a maxillary central incisor for palatal tipping and intrusion. *The Angle Orthodontist*, 87(4), 534-541.

Hohmann A, Kober C, Young P, Dorow C, Geiger M, Boryor A, Sander FM, Sander C, Sander FG (2011). Influence of different modeling strategies for the periodontal ligament on finite element simulation results. *American Journal of Orthodontics and Dentofacial Orthopedics*, 139(6), 775-783.

Hohmann A, Wolfram U, Geiger M, Boryor A, Sander C, Faltin R, Faltin K, Sander FG (2007). Periodontal ligament hydrostatic pressure with areas of root resorption after application of a continuous torque moment. *The Angle Orthodontist*, 77(4), 653-659.

Janson G, Sathler R, Fernandes TMF, Branco NCC, de Freitas MR (2013). Correction of Class II malocclusion with Class II elastics: A systematic review. *American Journal of Orthodontics and Dentofacial Orthopedics*, 143(3), 383-392.

Jones G, Buschang PH, Kim KB, Oliver DR (2008). Class II non-extraction patients treated with the forsus fatigue resistant device versus intermaxillary elastics. *The Angle Orthodontist*, 78(2), 332-338.

Knop L, Gandini LG Jr, Shintcovsk RL, Gandini MR (2015). Scientific use of the finite element method in Orthodontics. *Dental Press Journal of Orthodontics*, 20(2), 119-125.

Kucukkurt S (2019). Finite element stress analysis method and researches on dental implantology. *Journal of Dental Faculty of Atatürk University*, 29(4), 701-710.

Li LL, Wang ZY, Bai ZC, Mao Y, Gao B, Xin HT, Zhou B, Zhang Y, Liu B (2006). Three-dimensional finite element analysis of weakened roots restored with different cements in combination with titanium alloy posts. *Chin Med J*, 119(4), 305-311.

Liu DS, Chen YT (2015). Effect of thermoplastic appliance thickness on initial stress distribution in periodontal ligament. *Advances in Mechanical Engineering*, 7(4), 168781401557836.

Liu L, Song Q, Zhou J, Kuang Q, Yan X, Zhang X, Shan Y, Li X, Long H, Lai W (2022). The effects of aligner overtreatment on torque control and intrusion of incisors for anterior retraction with clear aligners: A finite-element study. *American Journal of Orthodontics and Dentofacial Orthopedics*, 162(1), 33-41.

Liu X, Cheng Y, Qin W, Fang S, Wang W, Ma Y, Jin Z (2022). Effects of upper-molar distalization using clear aligners in combination with Class II elastics: a three-dimensional finite element analysis. *BMC Oral Health*, 22(1), 546.

Liu X, Wang W, Gao J, Qin W, Wen Y, Luo H, Ma Y, Jin Z (2023). Actual contribution ratio of maxillary and mandibular molars for total molar relationship correction during maxillary molar sequential distalization using clear aligners with Class II elastics: A finite element analysis. *American Journal of Orthodontics and Dentofacial Orthopedics*, 164(4), e106-e120.

Luzi C, Luzi V (2013). Traitement de la classe II squelettique au moyen d'un appareil de Herbst à ancrage osseux. *L'Orthodontie Française*, 84(4), 307-318.

Nelson B, Hägg U, Hansen K, Bendeus M (2007). A long-term follow-up study of Class II malocclusion correction after treatment with Class II elastics or fixed functional appliances. A*merican Journal of Orthodontics and Dentofacial Orthopedics*, 132(4), 499-503.

Nucera R, Dolci C, Bellocchio AM, Costa S, Barbera S, Rustico L, Farronato M, Militi A (2022), Portelli M. Effects of composite attachments on orthodontic clear aligners therapy: A systematic review. *Materials*, 15(2), 533.

Patterson BD, Foley PF, Ueno H, Mason SA, Schneider PP, Kim KB (2021). Class II malocclusion correction with Invisalign: Is it possible? *American Journal of Orthodontics and Dentofacial Orthopedics*, 159(1), e41-e48.

Rossini G, Parrini S, Castroflorio T, Deregibus A, Debernardi CL (2015). Efficacy of clear aligners in controlling orthodontic tooth movement: A systematic review. *The Angle Orthodontist*, 85(5), 881-889.

Rossini G, Schiaffino M, Parrini S, Sedran A, Deregibus A, Castroflorio T (2020). Upper second molar distalization with clear aligners: A finite element study. *Applied Sciences*, 10(21), 7739.

Staderini E, Ventura V, Meuli S, Maltagliati L, Gallenzi P (2022). Analysis of the changes in occlusal plane inclination in a Class II deep bite "teen" patient treated with clear aligners: A case report. *International Journal of Environmental Research and Public Health*, 19(2), 651.

Tanne K, Sakuda M, Burstone CJ (1987). Three-dimensional finite element analysis for stress in the periodontal tissue by orthodontic forces. *American Journal of Orthodontics and Dentofacial Orthopedics*, 92(6), 499-505.

Turkkahraman H, Eliacik SK, Findik Y (2016). Effects of miniplate anchored and conventional Forsus Fatigue Resistant Devices in the treatment of Class II malocclusion. *The Angle Orthodontist*, 86(6), 1026-1032.

Unal T, Celikoglu M, Candirli C (2015). Evaluation of the effects of skeletal anchoraged Forsus FRD using miniplates inserted on mandibular symphysis: A new approach for the treatment of Class II malocclusion. *The Angle Orthodontist*, 85(3), 413-419.

Wang Q, Dai D, Wang J, Chen Y, Zhang C (2022). Biomechanical analysis of effective mandibular en-masse retraction using Class II elastics with a clear aligner: a finite element study. *Progress in Orthodontics*, 23(1), 23.

Challenge Journal of Structural Mechanics

Research Article

From ruins to reconstruction: Harnessing text-to-image AI for restoring historical architectures

Kawsar Arzomand [a,*], Michael Rustell [a], Tatiana Kalganova [b]

[a] *Department of Civil and Environmental Engineering, Brunel University London, UB8 3PH London, UK*
[b] *Department of Electronic and Electrical Engineering, Brunel University London, UB8 3PH London, UK*

ABSTRACT

The preservation of cultural heritage has become increasingly important in the face of conflicts and natural disasters that threaten historical sites worldwide. This study explores the application of artificial intelligence (AI), specifically text-to-image generation technologies, in reconstructing heritage sites damaged by these adversities. Utilising detailed textual descriptions and historical records, this study employed AI to produce accurate visual representations of damaged heritage sites, bridging the gap between traditional documentation and modern digital reconstruction methods. This approach not only enhances the architectural design process across various disciplines but also initiates a paradigm shift towards more dynamic, intuitive, and efficient heritage conservation practices. The methodology integrates data collection, iterative AI-generated image production, expert review, and comparative analysis against historical data to evaluate reconstruction accuracy and authenticity. By integrating AI with traditional preservation practices, this study advocates a balanced approach to conserving cultural legacies, ensuring their preservation and revitalisation for future generations. Preliminary findings suggest that AI-generated imagery holds significant promise for enhancing digital heritage preservation by offering novel approaches for visualising and understanding historical sites. These findings also highlight the need to address ethical, technical, and collaborative challenges to enhance the precision, reliability, and applicability of AI technologies in the field of cultural heritage. This study contributes to digital humanities and archaeological conservation, demonstrating AI's potential to support and complement traditional heritage preservation methods and suggests a pathway for substantial methodological evolution in the field.

ARTICLE INFO

Article history:
Received 10 April 2024
Revised 15 May 2024
Accepted 3 June 2024

Keywords:
Text-to-image synthesis
Architectural heritage
AI-assisted reconstruction
Prompt engineering
Digital archaeology
Cultural heritage preservation

1. Introduction

The architectural design process is crucial across various disciplines, from engineering and software development to the arts and humanities, and it is significantly shaped by the fusion of traditional methods and contemporary technological advancements. Recent innovations in AI, particularly text-to-image systems such as Midjourney, DALL-E, and Stable Diffusion, mark a substantial evolution in the design and heritage conservation arenas, signifying a paradigm shift towards more dynamic, intuitive, and efficient conceptualisation practices (Brisco et al. 2023; Kenig et al. 2023). This evolution reflects a broader movement to integrate cutting-edge AI tools within the architectural design process, underscoring the transition from conventional methods to more advanced, future-oriented approaches. The advent of 3D and 2D modelling tools, including Building Information Modelling (BIM) software such as ArchiCAD, AutoCAD, and SketchUp, has revolutionised architects' ability to visualise conceptual designs, while the application of AI techniques, ranging from conditional Generative

* *Corresponding author*. E-mail address: kawsar.arzomand@brunel.ac.uk (K. Arzomand)
ISSN: 2149-8024 / DOI: https://doi.org/10.20528/cjsmec.2024.02.004

Adversarial Networks (cGANs) to deep learning and machine learning algorithms, has initiated a new era in the digital preservation and reconstruction of historical landscapes and artefacts (Navarro-Mateu et al. 2021). These technological advancements are reshaping methodologies in archaeological research and conservation efforts, particularly as the architectural and cultural heritage sectors confront profound losses inflicted by conflicts and wars. Considering such destruction, AI has emerged as a pivotal tool, not only in attempting to preserve and reconstruct cultural heritage, but also to facilitate a deeper understanding of historical contexts (Kadhim and Abed 2023; Lee and Chang 2022).

The destruction of cultural heritage sites due to conflicts, natural disasters, and human activities poses a substantial challenge to preservation. Traditional reconstruction methods often rely on incomplete or damaged visual records, leading to reconstructions that may lack accuracy and authenticity. Recent advancements in text-to-image technology have introduced tools such as Midjourney and DALL-E, which have revolutionised the generation of high-quality photorealistic images from simple text prompts (Adetayo 2024; Kenig et al. 2023; Becker and Laycock 2023). AI entities can create images based on text prompts that mimic human cognitive processes (Kenig et al. 2023). Models such as Stable Diffusion, DALL-E, and Midjourney are notable in the realm of text-to-image generation (Cobb 2023; Huang et al. 2023; Lyu et al. 2022). The impact of these models is significant, influencing various fields such as neuroscience research, education, libraries, and architectural visual culture (Adetayo 2024; Becker and Laycock 2023; Steinfeld 2023). These tools have made it possible for users to create fully rendered images promptly, showcasing the potential of AI in creative endeavours (Newton and Dhole 2023).

AI-generated imagery offers a novel solution to the problem of accurately reconstructing heritage sites by leveraging detailed textual descriptions and historical records to produce accurate visual representations (Nichol et al. 2021; Ramesh et al. 2022). This study aimed to explore the effectiveness and broader implications of leveraging AI-generated imagery for the digital reconstruction of heritage sites that are significantly damaged by conflicts. By integrating the capabilities of these models with dense multi-image 3D reconstruction techniques, it is feasible to digitally reconstruct and visualise the destroyed cultural heritage sites (Rihani 2023; Wahbeh et al. 2016). In addition, the utilisation of 3D photogrammetric reconstruction methods along with AI-generated images can provide interactive and immersive experiences for visitors exploring reconstructed heritage sites (Rihani 2023; Soto-Martín et al. 2020). Employing generative adversarial networks (GANs) for heritage image super-resolution reconstruction can assist in estimating high-resolution images of ruins, thereby enhancing the visual quality of the reconstructed heritage sites (Nayak and Balabantaray 2021). Techniques such as laser scanning, photogrammetry, and UAV-based 3D reconstruction can provide detailed spatial information for large cultural heritage objects, thereby enhancing the accuracy of the reconstruction process (Xu et al. 2016; Bayram et al. 2015).

The novelty and contribution of this study lies in its innovative approach of using AI-driven text-to-image generation to reconstruct ruined heritage sites. Unlike traditional methods, which rely heavily on physical remnants or incomplete visual records, this research utilises detailed textual descriptions informed by historical, architectural, and archaeological sources to generate accurate visual representations of heritage sites. By carefully crafting text prompts based on extensive research from articles and historical sources, the AI models were able to generate images that closely resembled the original structure. This approach not only leverages the strengths of AI to produce highly accurate visual representations from textual descriptions but also bridges the gap between historical documentation and digital reconstruction. This integration offers a more reliable, accurate, and engaging method of heritage reconstruction, presenting significant advancements in the field of digital heritage preservation. This study makes several key contributions to the digital heritage preservation field. First, it introduces a novel application of text-to-image AI technologies in the context of heritage conservation, demonstrating their potential for creating accurate digital reconstructions from textual descriptions. Secondly, the study presents a comprehensive methodology that integrates AI-generated imagery with historical, architectural, and archaeological data. This interdisciplinary approach enhances the reliability and authenticity of digital reconstruction and provides a robust framework for future research. Thirdly, by producing new visual perspectives on the original states of damaged or destroyed heritage sites, the AI-generated images offer valuable insights into their architectural and cultural significance.

This method was applied to reconstruct the Buddha of Bamiyan in Afghanistan, a heritage site that was significantly damaged (Hammer et al. 2018; Grün et al. 2004). By interweaving historical narratives with AI capabilities, this study seeks to uncover new methodologies in cultural heritage preservation, contributing to the academic discourse within the digital humanities (Brisco et al. 2023; Kenig et al. 2023; Navarro-Mateu et al. 2021). This exploration is not merely a testament to technological innovation but also a commitment to bridging past and present, ensuring the enduring legacy of our collective cultural memory. By leveraging AI-generated imagery, this research offers a new avenue for the preservation and understanding of cultural heritage, addressing the profound challenges posed by conflicts and natural disasters (Kadhim and Abed 2023; Lee and Chang 2022). This study contributes to the academic discourse on digital humanities and archaeological conservation by demonstrating AI's potential to support and complement traditional heritage preservation methods (Bharati 2023; Orengo et al. 2015).

2. Methodology

In the exploration of digital reconstruction methodologies for heritage sites decimated by conflict, this study adopts a comprehensive, multi-faceted approach grounded

in the latest advancements in artificial intelligence (AI) technology. The core objective centres on harnessing the potential of AI, particularly text-to-image generation models such as Midjourney and DALL-E, to reimagine and digitally resurrect heritage sites from textual descriptions informed by historical, architectural, and archaeological evidence. This methodology intersects technological innovation with historical research, aiming to reconcile the physical remnants of the past with digital reconstructions, thereby offering new avenues for understanding and preserving our cultural heritage. Architects can utilize natural language inputs to convey their design intentions more naturally, which promotes quicker revisions and reduces the obstacles usually associated with traditional design tools (Ko et al. 2023; Hsu et al. 2022). The process involves a synergistic blend of data collection, AI image generation, expert validation, and comparative historical analysis, outlined as in Fig. 1.

Fig. 1. Overview of the five-step research methodology.

Fig. 2 illustrates a detailed flowchart of the five-phase methodology for AI-driven heritage site reconstruction. This comprehensive process begins with Data Collection and Preparation, involving the detailed gathering and organisation of textual descriptions, architectural details, and historical records, which are then cross-referenced for accuracy and compiled into a structured overview. The AI Image Generation Process follows, where initial prompts are created based on the collected data, and images are generated using AI platforms such as Midjourney and DALL-E. These prompts and images are iteratively refined and meticulously documented. The third phase, Image Selection and Iterative Refinement, focuses on evaluating AI-generated images against historical benchmarks, readjusting prompts, regenerating images, and conducting internal validation with expert collaboration. Comparative Analysis and Validation is the fourth phase, involving rigorous comparison of AI-generated images with historical records, continuous refinement, and detailed documentation to address inaccuracies. The final phase, Scholarly Discussion and Practical Implications, includes engaging in discussions on the ethical and practical implications of AI in heritage reconstruction, proposing frameworks for integrating AI into preservation practices, and evaluating the educational, commemorative, and advocacy potential of the reconstructions. This flowchart provides a visual representation of the iterative and detailed nature of the research methodology, ensuring transparency and reproducibility in the AI-driven reconstruction process.

2.1. Data collection and preparation

The initial phase involves the collection and analysis of textual descriptions, architectural details, historical accounts, and existing visual records of selected heritage sites (Remondino 2011). This extensive dataset is crucial for generating detailed prompts that provide a thorough historical context to guide the image-generation process. We gathered a diverse range of historical sources, such as books, academic journals, architectural blueprints, and digital archives, to create the dataset. The incorporation of official photographs from UNESCO and other reputable institutions improved the dataset by offering authentic references that are vital for validating the accuracy of our AI-generated reconstructions and ensuring adherence to established architectural and cultural standards. The data collection process involved manually reading historical sources and articles to identify keywords related to the original construction of the heritage sites. These keywords are used to create comprehensive textual prompts for the AI generation process. The systematic extraction and organisation of specific phrases and terminology indicative of heritage sites' original construction methods were documented in a database, which was categorised by heritage site, historical period, architectural style, and other relevant factors to facilitate their effective use in prompt generation.

2.2. AI image generation process

Employing AI platforms such as Midjourney and DALL-E, this study implements a systematic approach to convert textual prompts into visual reconstructions (Horn et al. 2022; Gualandi et al. 2021). Despite extensive research efforts aimed at uncovering photographic records to inform and validate reconstructions, certain heritage sites lack definitive visual records, presenting a significant challenge for accurately reconstructing their prime versions. Considering these constraints, the meth-

odology relies more on prompt engineering, utilising detailed textual descriptions derived from available historical documentation and expert insights. However, it is important to note that the AI-generated images produced under these conditions served as initial approximations rather than exact replicas of the original structures. The textual prompts derived from the compiled data aimed to accurately reflect the architectural and cultural aspects of the targeted heritage sites. Multiple iterations and a variety of prompts are utilized to address the multifaceted nature of each site, facilitating a broad spectrum of visual outputs (Kadhim and Abed 2023). Utilising the information presented in Table 1, initial prompts were formulated to encapsulate the fundamental architectural features, historical contexts, and cultural significance of each heritage site. For instance, the Buddhas of Bamiyan are described in terms of their monumental statues, niches, and surrounding features before they were destroyed. These prompts were iteratively fine-tuned based on AI-generated images. Each iteration involved adjusting the textual descriptions to improve the accuracy and detail of the generated images. This process has been thoroughly documented to track modifications and advancements. AI platforms generate multiple images based on refined prompts and capture diverse perspectives and details. The generated images were assessed by using historical records and visual references. For heritage sites with restricted photographic records, the methodology relies on extensive textual descriptions and expert insights to guide the AI. For instance, for Palmyra, where many structures have been damaged or destroyed, archaeological reports and historical texts provide necessary information.

2.3. Image selection and iterative refinement

The methodology employed in this phase focuses on a systematic approach for assessing AI-generated images against historical and archaeological standards. This involves refining textual prompts and regenerating new images based on evaluations, utilising prompt engineering to enhance the AI's capability to produce images that accurately reflect complex architectural designs and cultural nuances (Oppenlaender 2022). Xie et al. (2023) emphasised that crafting precise textual prompts can significantly impact the performance of AI, ensuring that the generated images closely align with architectural intent and historical context. The current approach to reconstruction is based on internal validation, but future research will involve input from historians, archaeologists, architects, and cultural experts. This expert feedback enhances the accuracy of the reconstructions and refines the prompts to align with a wider range of historical and cultural criteria. By continuing to iterate and refine the AI-generated outputs, we will improve their alignment with the historical records and architectural reliability. A systematic documentation process tracks each step of the prompt refinement and image generation, which is crucial for transparency and reproducibility. By repeatedly adjusting the textual prompts and regeneration of images, inaccuracies will be addressed, and the level of detail will be improved.

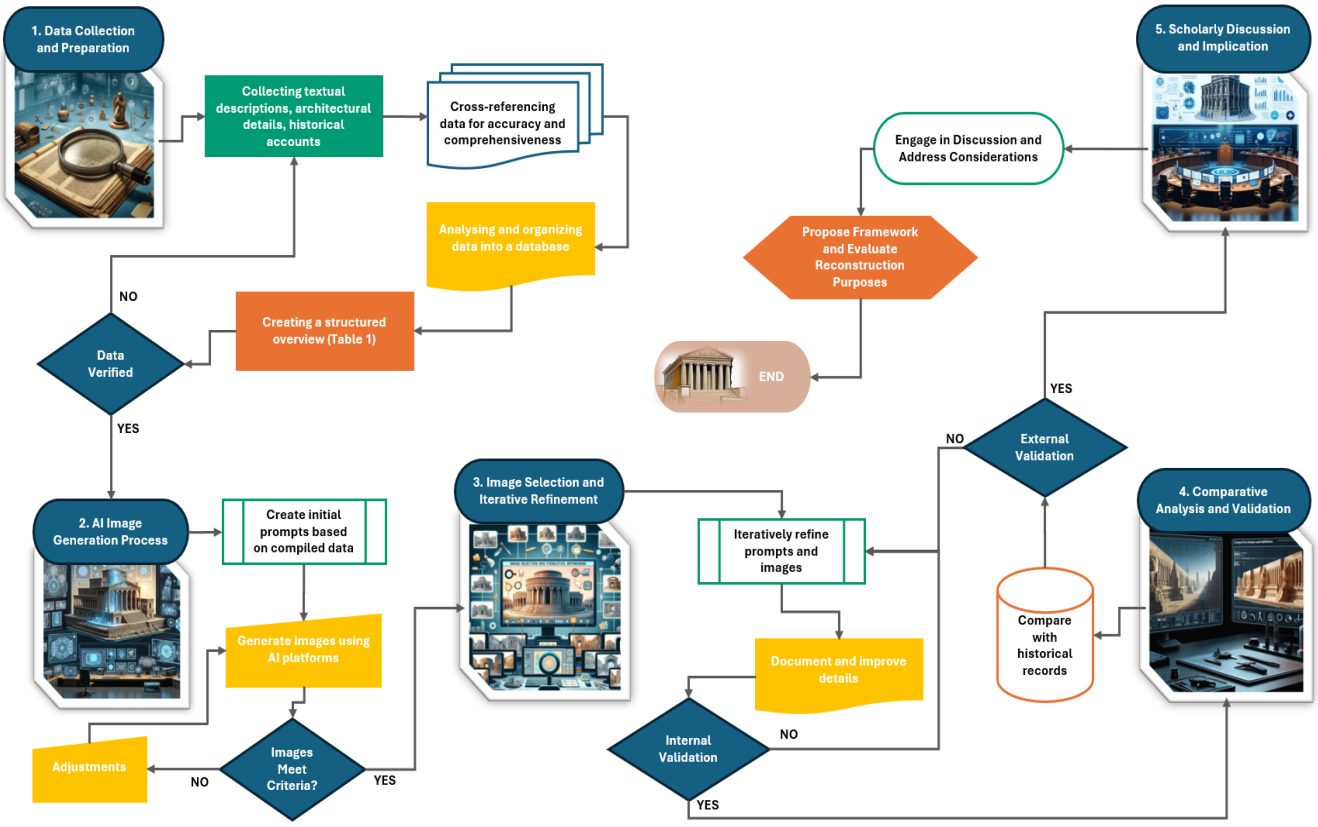

Fig. 2. Flowchart illustrating the five-phase methodology for AI-driven heritage site reconstruction.

Table 1. Overview of historical heritage sites: characteristics and conditions.

Site	Country	Period founded	Significant historical period	Main features	Destruction year	Area	Causes of damage	Current condition	Damaged parts	Key references
Palmyra	Syria	3rd millennium BC	Roman Empire, Islamic Caliphate	Temple of Bel, Great Colonnade	2015	Varies	Extremist group activities	Partially ruined	Temple of Bel, other structures	UNESCO, Britannica (Raja and Seland 2022; Elcheikh 2019)
Buddhas of Bamiyan	Afghanistan	6th century AD	Gandhara period	Two monumental statues	2001	105 hectares	Extremist group activities	Destroyed, niches remain	Two monumental statues	UNESCO (Asal et al. 2023; Toubekis et al. 2017; Grün et al. 2004)
Ancient City of Nimrud	Iraq	13th century BC	Assyrian Empire	Palaces, temples, colossal statues	2015	Over 360 hectares	Extremist group activities	Ruined	Palaces, temples, statues	UNESCO (Pollegioni et al. 2015; Reade 2002)
Pompeii	Italy	6th-7th century BC	Roman Empire	Urban infrastructure, frescoes	79 AD	66 hectares	Natural disaster (Volcanic Eruption)	Ruins preserved	Entire city	UNESCO, Britannica, (Scorrano et al. 2022; Wotzlaw et al. 2022; Senatore et al. 2014; Fulford and Wallace-Hadrill 1999)
Hampi	India	14th century AD	Vijayanagara Empire	Temples, royal complexes	1565	4187, 24 hectares	Historical Conflict	Ruins	Temples, marketplaces	UNESCO (Knell 2022; Rajangam and Sundar 2021; Powell 2018; Schettino 2016; Pakkeerappa and Thomas 2006)
Parthenon (Acropolis of Athens)	Greece	447-432 BC	Classical Greece	Doric temple dedicated to Athena	1687	69.5 by 30.9 m (228 by 101 ft)	Military Bombardment	Partially ruined	Structure, sculptures	UNESCO, Britannica (Angouri et al. 2017; Fincham 2012; Hamilakis 2002)
Temples of Thebes	Egypt	1500-30 BC	New Kingdom of Egypt	Karnak and Luxor temples	Various periods	7,390 ha with a buffer zone of 444 ha	Natural and Human Impact	Partially ruined	Karnak, Luxor temples	UNESCO, Britannica (Mahmoud et al. 2019; Manning 2012; Aubry et al. 2009)
The Great Wall	China	7th century BC and onwards	Various Chinese dynasties	Fortification system	Ongoing	21,196 km (total length)	Erosion and Human Impact	Partially ruined	Sections over time	UNESCO, Britannica (Cao et al. 2023; Shelach-Lavi et al. 2020; Yang 2017)
Maya Sites	Mexico	2000 BC to 16th century AD	Pre-Columbian Maya civilization	Temples, pyramids	Post 9th century AD	331,397 ha, surrounded by a buffer zone of 391,788 ha	Sociopolitical Decline	Ruins	Several city structures	UNESCO, Britannica (Chase et al. 2011; Scherer 2007)
Angkor Wat	Cambodia	Early 12th century	Khmer Empire	Temple complex	Not specified	Over 162 hectares	Neglect and Decay	Partially restored	Temples, infrastructure	UNESCO, Britannica (Chen 2021; Carter et al. 2019; Chen et al. 2016; Evans et al. 2013)

2.4. Comparative analysis and validation

This research incorporates a rigorous comparative analysis between AI-generated images and available historical sources, photographs, and scholarly interpretations. This validation phase assesses AI's capacity to accurately encapsulate the architectural styles, cultural significance, and ambient settings of the ruins (George 2022). The AI-generated images were evaluated by comparing them to historical records and visual references through a comprehensive analysis that included visual comparisons, consistency checks, and alignment of documentation for accuracy. Fig. 4 illustrates the AI-generated reconstructions of Palmyra, focusing on key elements such as the Temple of Bel, while Fig. 9 showcases the reconstructed images of Pompeii, highlighting hyper-realistic reconstructions of specific Roman buildings and emphasising the restoration of architectural elements and the site's historical and cultural significance. The images were assessed using photographs and descriptions to ensure accuracy. The iterative refinement process involves modifying prompts based on feedback from comparisons with historical records to ensure progressive alignment. This methodology employs prompt engineering to produce initial approximations of heritage sites, which are then refined using iterative processes.

2.5. Scholarly discussion and practical implications

The final phase of this research engages in a scholarly discussion on the implications of utilising AI for heritage reconstruction, focusing on future perspectives. This analysis employs ethical considerations, ensures historical accuracy while balancing technological advancements, and examines the interplay between digital innovation and traditional restoration practices. Key themes include the role of AI-generated imagery in enhancing educational and commemorative initiatives, and their contribution to broader heritage conservation efforts. This forthcoming discourse aims to navigate the complexities of AI applications in cultural preservation, addressing both potential benefits and challenges. This study evaluates how these reconstructions can serve educational, commemorative, and advocacy purposes within the broader framework of heritage preservation (Bharati 2023; Orengo et al. 2015). The initial phase primarily investigated the feasibility and potential of the AI-driven reconstructions. Future research should focus on specific heritage sites, such as the Buddhas of Bamiyan in Afghanistan, involving extensive collaboration with domain experts. This collaboration will aim to validate and refine the results, thereby ensuring robust and reliable outcomes. The structured approach to scholarly discussion will facilitate meaningful contributions to academic discourse on digital heritage preservation.

Subsequent validation phases will engage historians, archaeologists, and cultural experts to further refine the prompts and validate AI-generated images against a comprehensive set of historical and cultural criteria. Expert feedback enhances the accuracy and authenticity of the generated images. This multidisciplinary collaboration will significantly improve the reliability and validity of the reconstructions, ensuring that they adhere to rigorous historical and cultural standards.

By systematically employing AI-generated imagery based on historical and textual data, this study seeks to contribute to the emerging discourse on digital approaches to cultural heritage preservation and reconstruction. Prompt engineering is important for improving the generation of realistic images in text-to-image syntheses. This process involves carefully selecting and composing textual prompts to guide AI models in producing images that match the intended visual style or content described in the text (Oppenlaender 2022). The objective of strategic prompt engineering is to ensure that the generated images accurately reflect the input prompts, resulting in visually coherent and contextually relevant outputs. Designing prompts allows researchers and practitioners to influence generative AI systems to produce images with desired characteristics, such as realism, diversity, and adherence to specific visual styles (Xie et al. 2023; Rombach et al. 2022). Prompt engineering enhances the interpretability and controllability of text-to-image synthesis systems. By refining the prompts used to condition image generation, researchers can adjust output images to meet specific criteria or constraints, such as photorealism, colour accuracy, or object composition (Liu and Chilton 2021). This approach empowers users to shape the creative process of AI-generated image synthesis, allowing them to steer the output towards their desired visual outcomes (Taveekitworachai et al. 2023). The design and optimisation of prompts significantly impact the performance and capabilities of text-to-image generation systems, expanding their potential in design, art, and visual content creation. The integration of AI methodologies marks a new era in architectural conceptualisation and heritage conservation, ensuring that digital reconstructions can serve educational, commemorative, and advocacy purposes within a broader heritage preservation framework.

We employed two types of comparison methodology for our evaluation:

- Historical Accuracy Check: This involves verifying the AI-generated images against historical records and literature to ensure that the generated content aligns with the documented descriptions and visual references. This approach helps ensure the contextual and cultural accuracy of the images.
- Quantitative Metrics Evaluation: This involves utilising image quality metrics, such as SSIM, MSE, PSNR, and MAE, to quantitatively measure the similarity and fidelity of the AI-generated images. As illustrated in Figs. 11–13, these metrics offer a detailed quantitative analysis of the accuracy of the generated images compared with the original references.

By combining these two approaches, we ensured a comprehensive evaluation of the AI-generated reconstructions, balancing both qualitative historical accuracy and quantitative image fidelity.

3. Results and Discussion

This study examined the integration of 3D modelling techniques and AI in the reconstruction of heritage sites significantly damaged by conflicts and natural disasters, offering innovative solutions for cultural preservation. Drawing on the comprehensive flowchart detailed in the methodology section, this discussion enriches the narrative by incorporating additional insights into the systematic approach employed for AI-driven heritage reconstruction. Table 1 is a key resource for the AI-driven reconstruction process implemented in this study. By detailing the architectural characteristics, historical significance, and extent of damage to each heritage site, the table provides essential data that inform the development and calibration of AI models. This compilation of site-specific information ensures that AI-generated visualisations are contextually accurate and architecturally precise. For instance, the incorporation of specific architectural features and the extent of damage facilitated the AI's ability to interpolate missing data and extrapolate likely architectural elements where physical evidence is scant. Comprehensive data on the current conditions of the sites are provided in Table 1 aids in evaluating the effectiveness of AI for reconstructing various levels of decay and destruction. This evaluation was involved in refining the AI algorithms to enhance their adaptability and accuracy in dealing with the diverse preservation states found across the surveyed heritage sites. Thus, Ta-

ble 1 not only informs the technical execution of AI-driven reconstructions, but also deepens the analysis of how these technologies can be leveraged to preserve and interpret cultural heritage. This methodological foundation supports the subsequent discussion on the technological approaches listed in Table 2 highlighting advancements and identifying areas for further integration of AI into heritage preservation.

Table 2. Technological approaches in heritage site reconstruction.

Site	Author and year	Photogrammetry	3D GIS	CityGML	Parametric approaches	3D reconstruction modelling software	EMF	3DMM	2D-ERT	TOF cameras	Point Cloud	Deep learning methods	MayaArch3D	Reality-based 3D documentation tools	Information system	3D WebGIS	Crowdsourcing	Panoramic imagery	Remote sensing data	3D lase-scanning/recordings	Historical photography	VR technologies
Palmyra	Pan et al. (2020) Denker (2017) Wahbeh et al. (2016)	✓				✓												✓				
Maya Sites	von Schwerin et al. (2013) Pierrot-Deseilligny et al. (2011)	✓											✓			✓						
Pompeii	Sbrogiò (2022) Mazzaglia (2021)				✓										✓							
Buddhas of Bamiyan	Spallone et al. (2022) Bevilacqua et al. (2019) Maiwald et al. (2017) Heikkinen (2009)	✓				✓														✓	✓	✓
Ancient City of Nimrud	Biljecki et al. (2015) Gröger and Plümer (2012) Remondino (2011)	✓	✓	✓																		
Hampi	Keyvanfar et al. (2022) Natampally (2014)	✓				✓																
Parthenon	Hu et al. (2013) Debevec (2004)																			✓		
Temples of Thebes	Berto et al. (2021) Meister et al. (2021) Bennoui-Ladraa and Chennaoui (2018) Hu et al. (2013)	✓					✓	✓	✓													
The Great Wall	Zeng and Jin (2023) Zhou et al. (2022) Bassier et al. (2020)									✓	✓	✓										
Angkor Wat	Wang et al. (2020) Shishido et al. (2017)		✓			✓											✓		✓			

Table 2 provides a comprehensive historical overview of the technologies used across diverse heritage sites, offering an essential context for the application of contemporary AI techniques. For Palmyra, the reconstruction process involves a combination of public domain images and professional panoramic imagery (Wahbeh et al. 2016). This approach utilises crowdsourced images and 3D photogrammetric processes to create interactive immersive experiences, particularly for the reconstruction of the Temple of Bel. These tools and techniques have enabled researchers to digitally recreate and preserve the cultural heritage of Palmyra, emphasising the importance of advanced imaging techniques in restoration efforts (Pan et al. 2020; Denker, 2017). The reconstruction of Maya sites in Mexico has been enhanced by the application of photogrammetry techniques (Pierrot-Deseilligny et al. 2011). These automated image-based procedures allow accurate 3D modelling and orthoimage generation, which are instrumental in creating detailed reconstructions. Additionally, reality-based 3D documentation techniques involving software, such as 3D Studio, Maya, and Sketchup, have enabled realistic 3D models of Maya structures (Remondino and Rizzi 2010). The MayaArch3D project further supports this by providing a 3D WebGIS platform for analysing ancient Maya architecture and landscapes (von Schwerin et al. 2013). Mazzaglia (2021) discussed the Information System of the Pompeii Sustainable Preservation Project, which plays a key role in preserving cultural heritage through effective data management and knowledge sharing. Additionally, Sbrogiò (2022) proposed a parametric approach for reconstructing timber structures in Campanian Roman houses, offering insights into the architectural elements of ancient Roman buildings in Pompeii. Advanced technologies, such as 3D laser recording, photogrammetry, and virtual reality,

have been pivotal in reconstructing and preserving the heritage of Bamiyan Buddhas. Historical photography has also been crucial for providing archival images for virtual reconstruction projects (Spallone et al. 2022; Toubekis et al. 2017; Maiwald et al. 2017). The use of photogrammetry from archival imagery combined with 3D models of the current state underscores the importance of historical images in reconstruction efforts (Bevilacqua et al. 2019; Heikkinen 2009). The reconstruction of the Ancient City of Nimrud was significantly enhanced by the application of 3D GIS to archaeology. This tool is essential for urban reconstruction, modelling archaeological 3D objects, managing excavations, and analysing site development over time (Biljecki et al. 2015). In addition, CityGML supports the creation of interoperable semantic 3D city models that are vital for accurately depicting architectural elements and spatial relationships within ancient cities (Gröger and Plümer 2012). Photogrammetry and 3D scanning tools have also been integral to heritage recording and 3D modelling (Remondino 2011). This table highlights the evolution of technological applications in heritage reconstruction, showcasing both the advancements and existing gaps that AI technologies can bridge. This strategic integration of AI aligns with the current technological trends, ensuring that the study's results are innovative and grounded in proven practices.

The introduction of AI into this domain has been identified as a significant development, offering new possibilities for expediting the restoration process through predictive modelling and conceptual design ideation. This fusion of historical data with predictive AI capabilities promises to refine and accelerate the restoration workflow, facilitating a more efficient path for conserving cultural heritage (Rahim et al. 2021). Traditional architectural design, grounded in the rich tapestry of cultural and historical significance, emphasises the sustainability and artistic excellence cultivated over centuries (Liu et al. 2019). Such methods are pivotal in the context of modern architectural innovation, as they provide a sustainable framework for incorporating heritage values into contemporary designs (Hosseini et al. 2016; Mohammed and Haruna 2021). Conversely, AI-based architectural design represents a departure from conventional methods by, leveraging the power of AI to foster a more adaptable and superior architectural planning process (Li et al. 2023). Despite its transformative potential, this approach prompts critical ethical debates, particularly concerning its influence on human creativity and preservation of traditional design ethics (Hegazy and Saleh 2023). Furthermore, the role of AI in architectural education is emerging as a field of study, offering insights into how contemporary pedagogical theories can be integrated with cutting-edge technological advancements (Sadek 2023).

The AI-generated images, derived from detailed textual descriptions, provide critical insights into the original appearance of heritage sites that are significantly damaged by conflicts and natural disasters. These images function as visual reconstructions and interpretative tools, offering perspectives on sites' historical and cultural contexts that are often inaccessible through traditional architectural methods alone. For instance, the Palmyra images (Fig. 4) demonstrate AI capabilities to maintain historical accuracy, focusing on significant elements such as the Temple of Bel, the Baalshamin Temple, and ancient theatre. The photographs captured by Ko Hon Chiu Vincent and provided by UNESCO (Fig. 3) establish a baseline for the reconstruction process, ensuring that the AI models accurately represent the architectural details. Similarly, the AI-generated images of the Maya Sites (Figs. 6 and 7) highlight AI's role of AI in understanding the architectural layout and individual features of ancient cities. The prompts for these images were designed to showcase the architectural and archaeological precision of sites like Chichen Itza, thereby enhancing our knowledge and appreciation of Mayan civilisation. The Pompeii reconstruction images (Fig. 9) illustrate AI's utility in the restoration of specific historical sections, focusing on the accurate reconstruction of Roman buildings. This approach contributes significantly to the overall preservation and comprehension of the site. The AI-driven reconstruction of the Buddha of Bamiyan (Fig. 10) exemplifies the integration of deep historical research with advanced AI technologies. Fig. 10(a) provides a foundational visual reference that is essential for accurate digital reconstruction, whereas Figs. 10(b) and 10(c) illustrate the advanced capabilities of AI in recreating this cultural monument with precise detail and historical accuracy. The process of generating images using AI is rooted in extensive academic research that draws from a variety of sources including historical texts, scholarly articles, and journal publications. This approach ensures that each image produced by AI is not simply a general representation but a detailed and accurate reconstruction that is steeped in a deep understanding of the site's historical and cultural context. These reconstructions serve several objectives, including bridging the gap between the past and the present, providing educational material that enhances the understanding of the site's cultural context, and offering visual simulations for restoration projects. The use of AI in this way supports the preservation of a site's visual heritage while also contributing to the ongoing development of historical scholarship. The application of AI to interpreting and visualising historical data represents a significant advancement in the fields of digital architecture, archaeology, and heritage conservation. This demonstrates the potential of combining technological innovation with traditional historical research, thereby opening new possibilities for the preservation and presentation of heritage sites impacted by time and human conflict.

In the initial stages of this study, we used AI tools to generate prompts, and subsequently used these prompts to create images. However, the initial results were not as accurate or detailed as expected. This prompted us to delve deeper into historical records and journal articles to gather more precise information about heritage sites. For example, in the case of Bamiyan Buddhas, we discovered that the original statues were constructed using mud on rock, covered with lime plaster, and often painted with molten metal. These statues combined Indian, Persian, and Greek artistic styles, and some of the

oldest Buddhist manuscripts, such as the Kharosthi scripts, were found in the surrounding caves. The evaluation metrics for AI-generated images in this study involved a multifaceted approach to ensure accuracy and alignment with historical and cultural contexts. Initially, the images were subjected to internal validation, in which prompt engineering played a critical role. This involved refining textual prompts to enhance AI's capability to produce images that closely resemble the intended architectural designs and cultural nuances. The methodology emphasises the iterative refinement process, in which prompts are continuously adjusted based on the initial outputs, leading to progressively accurate visual representations. This approach ensured that the generated images were not only realistic but also contextually relevant, accurately reflecting the architectural intent and historical context. The AI-generated reconstructions of Palmyra and Pompeii were compared with historical records and visual references, focusing on key elements such as the Temple of Bel and specific Roman buildings. Using this detailed historical information, we refined our prompts to include specific keywords and contextual information. This approach significantly improves the quality and accuracy of AI-generated images. For instance, Figs. 10(b) and 10(c) of Bamiyan Buddhas exhibit a higher degree of similarity to the original statues compared to earlier attempts.

3.1. Palmyra (Syria)

Prompt:

- A newly reconstructed Palmyra, where the essence of its ancient glory is captured in a structure that stands proud and unblemished under the clear sky. At its heart, a grand edifice, inspired by the Temple of Bel, showcases a symmetrical front view with a grand entrance. The architecture boasts complete and pristine columns rising to support a perfectly restored entablature, capped with a pediment that marries timeless artistry with contemporary innovation. This masterpiece gleams in the sunlight, reflecting a blend of historical reverence with the pinnacle of modern reconstruction. The surrounding environment is meticulously maintained, featuring a well-kept street leading to the temple's imposing steps, inviting visitors into a space where history and the present are seamlessly intertwined. Capture the essence of both ancient grandeur and modern architectural achievements, highlighting the harmony between past and future (Figs. 3 and 4).

Fig. 3. Photographs of the existing ruins of Palmyra, showcasing the Temple of Bel, the Baalshamin Temple, and the ancient theatre, taken by Ko Hon Chiu Vincent and provided by UNESCO.

Fig. 4. Midjourney and DALL-E, AI-generated reconstructions of different sections of the ancient city of Palmyra.

3.2. Maya Sites (Mexico)

Prompts:

- Chichen Itza in its heyday, focusing on the Pyramid of Kukulcan and the Great Ball Court. Show the precise architectural and astronomical alignment of the pyramid, the ornate carvings, and the surrounding temples and sacred cenotes. The lush Yucatan jungle should frame the site, highlighting the Maya's connection with their environmental, realistic, architectural design (Fig. 5).
- A detailed 3D model description of the complete architectural layout of Chichen Itza, focusing on the overall arrangement of the ancient Maya city's buildings and structures. Describe the spatial relationships

between the step-pyramids, temples, ball courts, observatory, and other key architectural features, providing information on their relative sizes, orientations, and distances from one another. Emphasize the architectural aesthetics and the visual impact of Chichen Itza's layout, allowing for a comprehensive representation of this ancient Maya city's architectural grandeur (Fig. 6).

Fig. 5. Photographs of ancient Maya archaeological sites in Mexico, captured by Community Tours Sian Ka'an and Ko Hon Chiu Vincent under UNESCO's recognition of these historical treasures.

Fig. 6. Midjourney AI-generated complete architectural layout of Chichen Itza of the ancient Maya city.

- The intricate architectural features of Chichen Itza, emphasizing the design and construction of the ancient Maya city's iconic buildings and structures. Highlight the specific elements of architecture, such as the step-pyramids, temples, ball courts, and observatory, and provide insights into their unique architectural styles, ornamentation, and any notable construction techniques or materials used. Capture the essence of Chichen Itza's architectural marvels in their prime, showcasing the cultural and artistic achievements of the ancient Maya civilization (Fig. 7).

Fig. 7. Midjourney AI-generated representations of distinctive features of Chichen Itza.

3.3. Pompeii (Italy)

Prompt:

- Create a hyper-realistic image reconstructing the specific section of the ancient Roman building in Pompeii, Italy. The reconstruction should focus only on the visible section in the original image, maintaining the same perspective and architectural elements. The mosaic patterns, column details, and architectural style should match the original as closely as possible, restored to how they might have appeared before any damage. The setting remains the same with the surrounding ruins still visible, but the specific section should appear fully restored with accurate colours and details (Figs. 8 and 9).

Fig. 8. Photographs showing the ruins of Pompeii, including detailed architectural remnants and structures. Images captured by J. Frias Velatti and Limes.Media/Tim Schnarr, as featured on the UNESCO website.

Fig. 9. Midjourney and DALL-E, AI-generated reconstructions of ancient Pompeii, showcasing its historic architecture and interiors.

3.4. Buddhas of Bamiyan (Afghanistan)

Prompt:

- Reconstruct the standing Buddha of Bamiyan, standing 180 feet tall and carved into a sandstone cliff. The Buddha is depicted in a standing posture with intricate, layered robes that showcase a blend of Hellenistic and Indian artistic influences. The statue's face reflects a serene, meditative expression typical of Indian Buddhist art. The materials used are traditional mud, straw, and lime plaster, giving it an aged yet restored look. The rugged mountainous terrain of the Bamiyan Valley surrounds the Buddha, emphasizing its monumental scale and cultural significance. Side architectures include detailed carvings and Kharosthi scripts to enhance historical accuracy (Fig. 10).

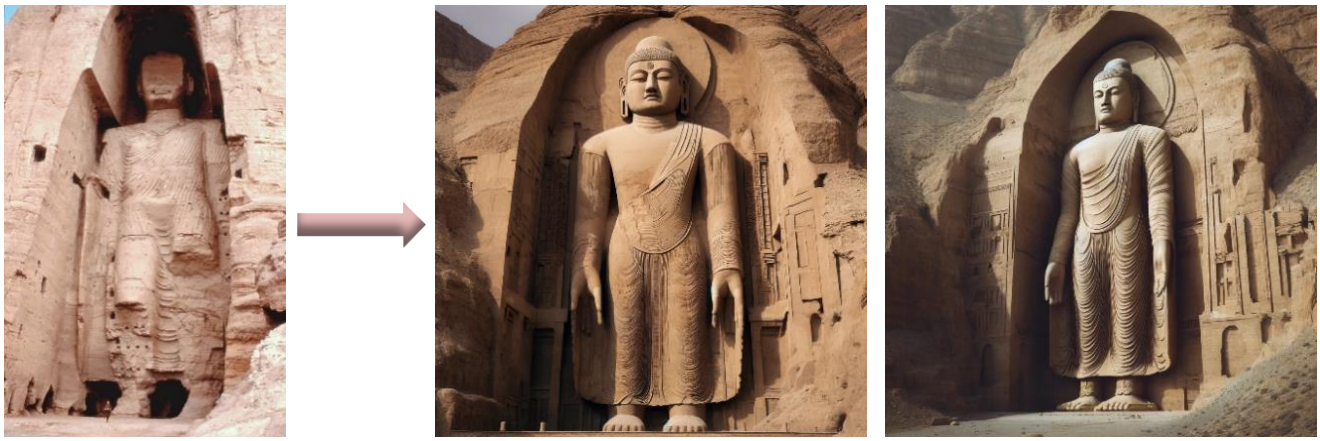

Fig. 10. Transformation of the Buddha of Bamiyan: The left image shows the original state of the statue following its destruction, while the centre and right images represent AI-generated reconstructions.

A comprehensive set of image quality metrics was employed to assess the quality and accuracy of AI-generated images. These metrics included the Structural Similarity Index Measure (SSIM), Mean Squared Error (MSE), Peak Signal-to-Noise Ratio (PSNR), and Mean Absolute Error (MAE). Each of these metrics offers unique insights into different aspects of image fidelity and similarity.

- SSIM is a perceptual metric that quantifies the image quality by comparing the luminance, contrast, and structure between the generated and original images. SSIM values range from 0 to 1, with values closer to 1 indicating higher similarity. During the evaluation, the SSIM values ranged from 0.083 to 0.125. Fig. 13 achieved the highest SSIM value of 0.125, suggesting that it closely matches the structural characteristics of the original image. This indicates that the AI-generated image effectively preserved the structural integrity and visual information of the original heritage site.
- MSE measures the average squared difference between the pixel values of the original and generated images. Lower MSE values indicate fewer errors and better image quality. In our study, MSE values ranged from approximately 7,568,117 to 12,674,829. Fig. 13 exhibited the lowest MSE value of 7,568,117, demonstrating the smallest deviation from the original image in terms of pixel intensity, thereby indicating a high degree of similarity and reduced error.
- The Peak Signal-to-Noise Ratio (PSNR) is an engineering metric that measures the ratio of the maximum possible power of a signal to the power of corrupting noise and is usually expressed in decibels (dB). Higher PSNR values indicate a better image quality and less distortion. In our evaluation, the PSNR values ranged from 7.101 to 9.341 dB, with Fig. 13 attaining the highest PSNR value of 9.341 dB. This high PSNR value suggests that Fig. 13 has minimal noise and high fidelity, closely resembling the original image in terms of quality.
- The Mean Absolute Error (MAE) evaluates the average absolute difference between the pixel values of the original and generated images. Lower MAE values indicated better image quality and fewer absolute errors. In our study, the MAE values ranged from approximately 135.359 to 148.749, with Fig. 12 having the lowest MAE value of 135.359, indicating the least average deviation from the original image. This highlights the accuracy of the AI-generated image in maintaining the pixel-intensity distribution of the original image.

To evaluate the performance of the AI-generated reconstructions, we selected ten images of the giant Buddha statue. The choice of the Buddha statue allowed us to conduct a detailed and focused analysis utilising the metrics described above to evaluate the quality of the generated images. For other AI-generated images, such as those of the Maya, Pompeii, and Palmyra sites, our approach was primarily exploratory. We tested the AI tool to determine whether it could produce results consistent with historical records and keywords derived from journal articles and historical sources. However, our detailed metric evaluation specifically focused on the Buddha statue, allowing us to thoroughly validate one heritage site before extending the same level of evaluation to others in future research (Figs. 11–13).

Fig. 13 consistently performed well across all metrics, achieving the highest SSIM, lowest MSE, highest PSNR, and relatively low MAE values. This indicates that Fig. 13 is one of the best reconstructions, offering high structural similarity, minimal error, and high overall quality compared to the original image.

4. Limitations and Future Directions

This research highlights several limitations that impact the accuracy and authenticity of AI-generated reconstructions of heritage sites. Addressing these limitations can refine current methodologies and suggest future research directions to enhance the precision and reliability of digital reconstructions.

Lack of Original Visual References: One of the major obstacles in rebuilding damaged cultural heritage sites is the absence of original photographs or visual references, which prevents direct comparison and calculation of similarity metrics. To overcome this, evaluations rely on historical records, descriptions, and expert opinion. Future research should address this limitation by collaborating with academics and experts, whose feedback will be essential for validating reconstructions and ensuring their accuracy and validity in the absence of visual data.

Image Index	SSIM	MSE	PSNR	MAE
0	0.101	9,017.881	8.580	141.976
1	0.121	9,608.402	8.304	137.411
2	0.112	8,831.041	8.671	138.425
3	0.097	9,949.898	8.153	142.216
4	0.112	12,674.829	7.101	135.359
5	0.116	11,257.832	7.616	138.810
6	0.083	12,496.312	7.163	137.126
7	0.108	11,429.549	7.551	136.209
8	0.112	8,340.277	8.919	143.173
9	0.125	7,568.117	9.341	148.749

Fig. 11. Comparison of AI-generated images of the Giant Buddha Statue using evaluation metrics.

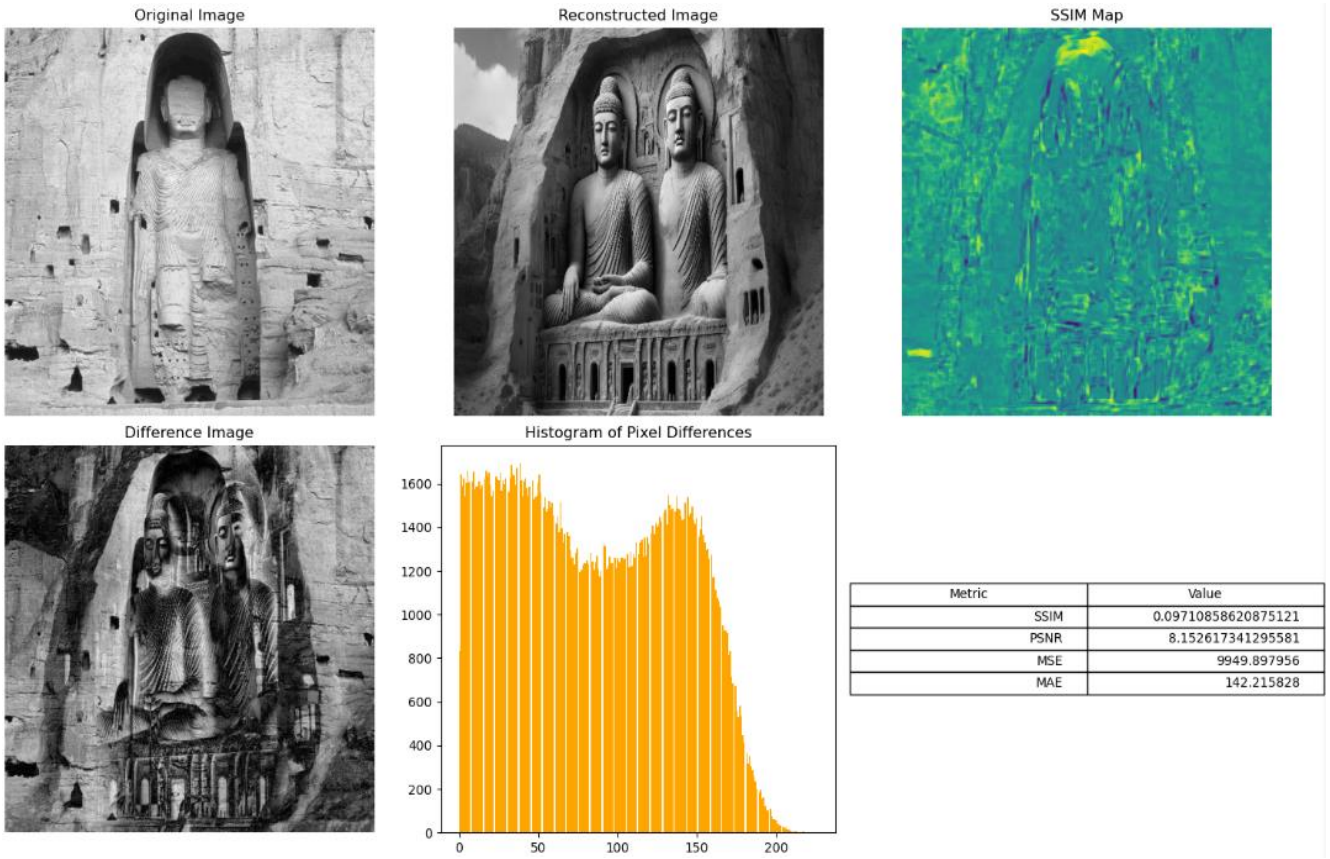

Metric	Value
SSIM	0.09710858620875121
PSNR	8.152617341295581
MSE	9949.897956
MAE	142.215828

Fig. 12. First figure displaying the evaluation of AI-generated images of the Giant Buddha statue using several comparison metrics.

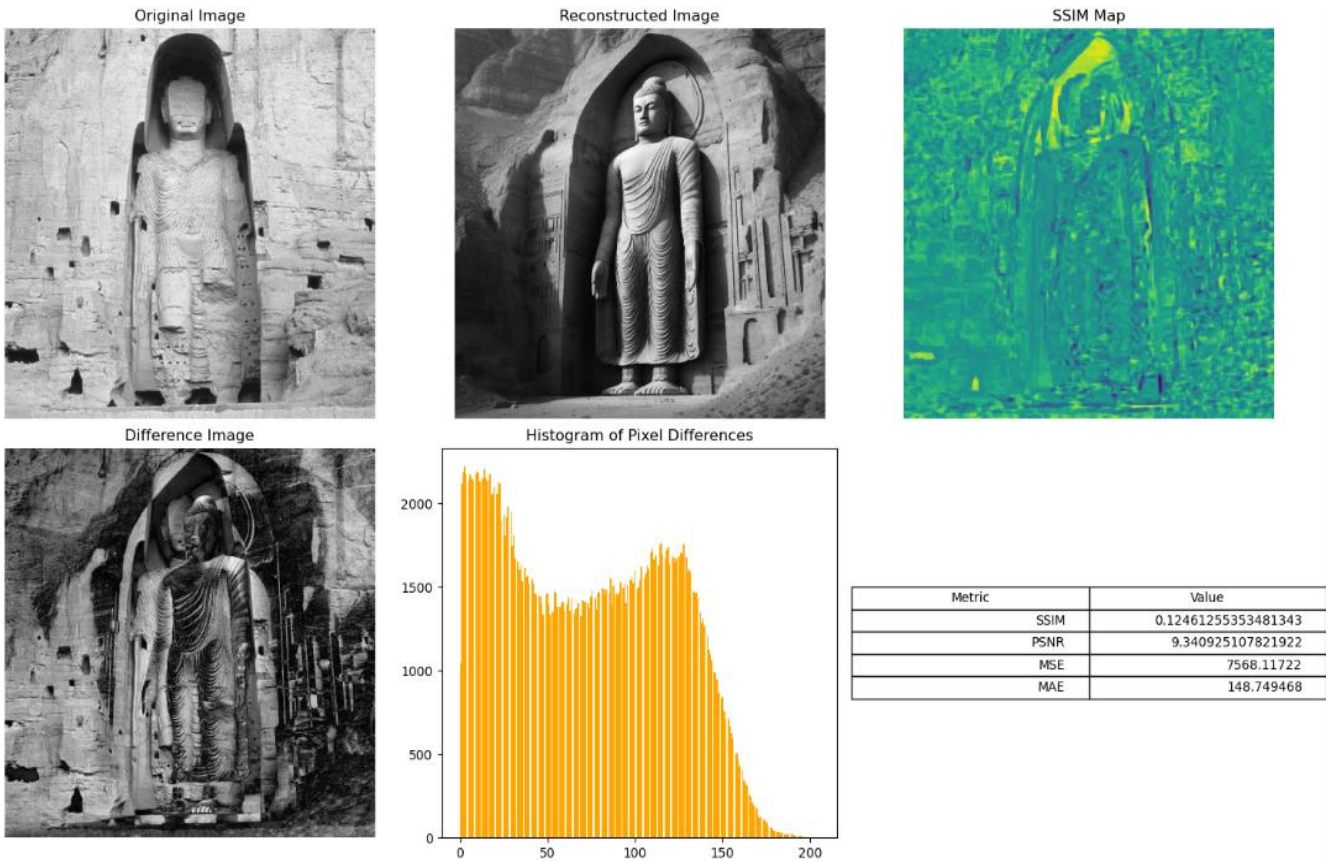

Metric	Value
SSIM	0.12461255353481343
PSNR	9.340925107821922
MSE	7568.11722
MAE	148.749468

Fig. 13. Second figure displaying the evaluation of AI-generated images of the Giant Buddha statue using several comparison metrics.

Automated Information Extraction and Prompt Engineering: AI's role in reconstructing heritage sites involves challenges such as the lack of comprehensive photographic records, necessitating reliance on textual descriptions and expert insights. The dependence of the current methodology on manually curated prompts from historical documents and academic sources limits the comprehensiveness and accuracy of AI-generated images. Future research will explore automating this process using advanced AI to autonomously search, extract, and summarise relevant information, aiming to generate more detailed and precise prompts. This development could refine theoretical understanding of AI's capabilities in interpreting complex historical data and contribute to the discourse on AI's role in digital archaeology and heritage reconstruction.

Consistency and Reproducibility in AI Outputs: Variability in AI-generated images remains a significant challenge, complicating the process of achieving consistent reconstructions from multiple angles. Future research will focus on integrating advanced generative AI models, such as stable diffusion algorithms, to improve the consistency and reproducibility of AI outputs. Enhancing these aspects will make AI reconstructions more reliable for educational, cultural, and research purposes.

Enhancement of Detail-oriented Reconstructions: The accuracy of AI-generated images depends on detailed input data. Current models require explicit details regarding dimensions, materials, and spatial configurations, which are often lacking in textual descriptions. To address this, ongoing research must improve data collection methods and prompt formulation to include detailed and complex architectural and archaeological specifics. Developing AI systems capable of effectively interpreting detailed descriptive data will refine AI's ability to render accurate images, encouraging deeper integration of AI models with archaeological and architectural theories.

Acknowledged Methodological Constraints: The interpretative nature of AI reconstructions, based on incomplete data and potential biases in expert interpretations, highlights the existing methodological constraints. Continuous enhancements in AI technology and collaborative efforts with domain experts are essential to ensure that digital reconstructions closely adhere to historical accuracy and cultural authenticity. As AI technologies become more integrated into heritage preservation, they can inform policy decisions and strategies at both national and international levels, leading to the development of new guidelines for ethical and effective digital reconstruction and preservation.

This study lays the foundation for the use of AI in the digital reconstruction of heritage sites. The limitations and future directions outlined suggest a pathway for methodological evolution, aiming for more nuanced, accurate, and culturally respectful digital preservation practices.

5. Conclusions

This study highlights the significant potential of artificial intelligence (AI) in the preservation of cultural heritage, particularly through the digital reconstruction of sites impacted by conflicts and natural disasters. Utilising AI-generated imagery, derived from detailed textual descriptions and historical analyses, this research has provided new perspectives on the original appearance of heritage sites, thereby introducing innovative methodologies for architectural conceptualisation and heritage conservation. The evaluation process we conducted was comprehensive and focused on assessing the AI-generated reconstructions of the Giant Buddha statue, using key performance indicators such as the Structural Similarity Index Measure (SSIM), Mean Squared Error (MSE), Peak Signal-to-Noise Ratio (PSNR), and Mean Absolute Error (MAE). Among the images that were tested, Fig. 13 consistently performed the best, achieving the highest SSIM score (0.125), lowest MSE value (7,568,117), highest PSNR (9.341 dB), and low MAE (148.749). These metrics indicate that Fig. 13 closely aligns with the structural characteristics, pixel intensity, and overall quality of the original image, thereby making it one of the most accurate AI reconstructions. By integrating AI with traditional preservation practices, this research advocates a balanced approach to conserving cultural legacies, ensuring that they are both preserved and revitalised for future generations. We evaluated the performance of AI tools in generating results that align with historical records and keywords derived from journal articles and historical sources for architectural heritages such as Maya sites, Pompeii, and Palmyra. These findings underscore the need to address the ethical, technical, and collaborative challenges. Specifically, our analysis revealed that the precision of AI-generated reconstructions can be limited by the quality of the input data, underscoring the need for advanced algorithms that are capable of handling incomplete data with greater accuracy. Future research should focus on refining AI algorithms and expanding methodological frameworks to enhance the precision, reliability, and applicability of AI technologies in the cultural heritage field. This requires advancing the capability of AI systems to process and interpret complex and often incomplete data with greater accuracy and detail. The application of AI to heritage conservation presents critical interdisciplinary challenges that require collaborative approaches. Integrating the capabilities of AI with the expertise of historians, archaeologists, and architects is essential to ensure that digital reconstructions are not only technically accurate, but also culturally and historically nuanced. This collaboration is important for developing ethical standards and frameworks that guide the responsible application of AI, emphasising sustainability, and respect for the validity and integrity of cultural heritage. Furthermore, the integration of AI into heritage conservation practices has revolutionised the ways in which we interact with and understand our cultural past. By enhancing the accessibility of heritage through digital means, AI enables broader engagement and educational opportunities, thus making cultural heritage more accessible and relatable to a

global audience. This transformative potential of AI not only supports preservation efforts but also enriches our collective cultural understanding. In conclusion, this research contributes to the foundational work employing AI for the digital reconstruction of heritage sites and suggests a pathway for substantial methodological evolution. By progressively addressing the outlined challenges and leveraging documented improvements in reconstruction accuracy and data handling, the field can advance towards more nuanced, accurate, and culturally respectful digital preservation practices. The continuous refinement of AI technologies and their integration into heritage conservation will be pivotal in ensuring that this new era of digital engagement with our past is marked by both innovation and respect for historical accuracy and cultural significance.

Acknowledgements

This research has previously been presented at the 2nd International Summit on Civil, Structural and Environmental Engineering (ISCSEE2024) held in Florence, Italy, on March 18-20, 2024. Extended version of the research has been submitted to Challenge Journal of Structural Mechanics and has been peer-reviewed prior to the publication.

Funding

The authors received no financial support for the research, authorship, and/or publication of this manuscript.

Conflict of Interest

The authors declared no potential conflicts of interest with respect to the research, authorship, and/or publication of this manuscript.

Author Contributions

All of the authors made substantial contributions to conception and design, or acquisition of data, or analysis and interpretation of data; were involved in drafting the manuscript or revising it critically for important intellectual content; and gave final approval of the version to be published.

Data Availability

The datasets created and/or analyzed during the current study are not publicly available, but are available from the corresponding author upon reasonable request.

REFERENCES

Adetayo AJ (2024). Reimagining Learning through AI Art: The Promise of DALL-E and MidJourney for Education and Libraries. *Library Hi Tech News*.

Angouri J, Paraskevaidi M, Wodak R (2017). Discourses of cultural heritage in times of crisis: the case of the Parthenon Marbles. *Journal of Sociolinguistics*, 21(2), 208–237.

Asal V, Avdan N, Ackerman G (2023). Breaking taboos: Why insurgents pursue and use CBRN weapons. *Journal of Peace Research*, 60(2), 193–208.

Aubry M, Berggren WA, Dupuis C, Ghaly H, Ward D, King C, Knox RWO, Ouda K, Youssef M, Galal WF (2009). Pharaonic Necrostratigraphy: A review of geological and archaeological studies in the Theban Necropolis, Luxor, West Bank, Egypt. *Terra Nova*, 21(4), 237–256.

Bassier M, Yousefzadeh M, Vergauwen M (2020). Comparison of 2D and 3D wall reconstruction algorithms from point cloud data for as-built BIM. *Journal of Information Technology in Construction*, 25, 173–192.

Bayram B, Nemli G, Özkan T, Oflaz OE, Kankotan B, Çetin İ (2015). Comparison of laser scanning and photogrammetry and their use for digital recording of cultural monument case study: Byzantine Land Walls-Istanbul. *Isprs Annals of the Photogrammetry Remote Sensing and Spatial Information Sciences*, II-5(W3), 17–24.

Becker C, Laycock R (2023). Embracing deepfakes and AI-generated images in neuroscience research. *European Journal of Neuroscience*, 58(3), 2657–2661.

Bennoui-Ladraa B, Chennaoui Y (2018). Use of photogrammetry for digital surveying, documentation and communication of the cultural heritage. Example regarding virtual reconstruction of the access doors for the Nameless Temple of Tipasa (Algeria). *Studies in Digital Heritage*, 2(2), 121–137.

Berto S, Demetrescu E, Fanini B, Bonetto J, Salemi G (2021). Analysis and validation of the 3D reconstructive process through the extended matrix framework of the Temple of the Roman Forum of Nora (Sardinia, CA), in: *ArcheoFOSS XIII Workshop—Open Software, Hardware, Processes, Data and Formats in Archaeological Research*, Basel, Switzerland, 18.

Bevilacqua MG, Caroti G, Piemonte A, Ulivieri D (2019). Reconstruction of lost architectural volumes by integration of photogrammetry from archive imagery with 3-D models of the Status Quo. *The International Archives of the Photogrammetry, Remote Sensing and Spatial Information Sciences*, XLII-2/W9, 119–125.

Bharati P (2023). Leveraging AI for archaeological insights: generating visual representations of historical events - a case study of the Hastinapur Flood during the Reign of King Nichakshu. *International Journal for Research in Applied Science and Engineering Technology*, 11(10), 142–145.

Biljecki F, Stoter J, Ledoux H, Zlatanova S, Çöltekin A (2015). Applications of 3D City models: state of the art review. *ISPRS International Journal of Geo-Information*, 4(4), 2842–2889.

Brisco R, Hay L, Dhami S (2023). Exploring the role of text-to-image AI In concept generation. *Proceedings of the Design Society*, 3, 1835–1844.

Cao Y, Bowker MA, Delgado-Baquerizo M, Xiao B (2023). Biocrusts protect the Great Wall of China from erosion. *Science Advances*, 9(49).

Carter AK, Stark MT, Quintus S, Zhuang Y, Wang H, Heng P, Chhay R (2019). Temple occupation and the tempo of collapse at Angkor Wat, Cambodia. *Proceedings of the National Academy of Sciences*, 116(25), 12226–12231.

Chase AF, Chase DZ, Weishampel JF, Drake JB, Shrestha RL, Slatton KC, Awe JJ, Carter WE (2011). Airborne LiDAR, archaeology, and the ancient Maya landscape at Caracol, Belize. *Journal of Archaeological Science*, 38(2), 387–398.

Chen C (2021). Angkor Wat: a transcultural history of heritages. *Journal of Southeast Asian Studies*, 52(1), 133–140.

Chen C, Leask A, Phou S (2016). Symbolic, experiential and functional consumptions of heritage tourism destinations: The case of Angkor World Heritage Site, Cambodia. *International Journal of Tourism Research*, 18(6), 602–611.

Cobb PJ (2023). Large language models and generative AI, oh my! *Advances in Archaeological Practice*, 11(3), 363–369.

Debevec P (2004). The Parthenon, in: *ACM SIGGRAPH 2004 Computer animation festival on - SIGGRAPH '04*, (p. 188). New York, New York, USA: ACM Press.

Denker A (2017). 3d visualization and photo-realistic reconstruction of the Great Temple of Bel. *The International Archives of the Photogrammetry, Remote Sensing and Spatial Information Sciences*, XLII-2(W3), 225–229.

Elcheikh Z (2019). Palmyra: A story of ruins, struggle(s) and beyond. *Chronos*, 39, 105–123.

Evans DH, Fletcher RJ, Pottier C, Chevance J-B, Soutif D, Tan BS, Im S, Ea D, Tin T, Kim S, Cromarty C, De Greef S, Hanus K, Bâty P, Kuszinger R, Shimoda I, Boornazian G (2013). Uncovering archaeological landscapes at Angkor using lidar. *Proceedings of the National Academy of Sciences*, 110(31), 12595–12600.

Fincham D (2012). The Parthenon sculptures and cultural justice. *Fordham Intellectual Property, Media & Entertainment Law Journal,* 23, 943.

Fulford M, Wallace-Hadrill A (1999). Towards a history of pre-Roman Pompeii: Excavations beneath the house of Amarantus (I.9.11–12), 1995–8. *Papers of the British School at Rome*, 67, 37–144.

George P (2022). AI *Trends in Digital Humanities Research*. *Trends in Computer Science and Information Technology*, 7(2), 026–034.

Gröger G, Plümer L (2012). CityGML – *Interoperable Semantic* 3D *City Models*. *ISPRS Journal of Photogrammetry and Remote Sensing*, 71, 12–33.

Grün A, Remondino F, Zhang L. (2004). Photogrammetric *Reconstruction of the* Great Buddha of Bamiyan, Afghanistan. *The Photogrammetric Record*, 19(107), 177–199.

Gualandi ML, Gattiglia G, Anichini F (2021). An *Open System for Collection and Automatic Recognition of Pottery through Neural Network Algorithms*. *Heritage*, 4(1), 140–159.

Hamilakis Y (2002). The *Other* 'Parthenon': *Antiquity and National Memory* at Makronisos. *Journal of Modern Greek Studies*, 20(2), 307–338.

Hammer E, Seifried R, Franklin K, Lauricella A (2018). Remote *Assessments of the Archaeological Heritage Situation* in Afghanistan. *Journal of Cultural Heritage*, 33, 125–144.

Heikkinen J (2009). Close-*Range Constrained Image Sequences*. *ISPRS Journal of Photogrammetry and Remote Sensing*, 64(3), 267–274.

Horn C, Ivarsson O, Lindhé C, Potter R, Green A, Ling J (2022). Artificial *Intelligence*, 3D *Documentation*, and *Rock Art—Approaching and Reflecting on the Automation of Identification and Classification of Rock Art Images*. *Journal of Archaeological Method and Theory*, 29(1), 188–213.

Hsu Y-C, Yang Z, Buehler MJ (2022). Generative *Design, Manufacturing, and Molecular Modeling* of 3D *Architected Materials Based on Natural Language Input*. *APL Materials*, 10(4).

Hu G, Mortazavian P, Kittler J, Christmas W (2013). A *Facial Symmetry Prior for Improved Illumination Fitting of* 3D *Morphable Model*, *International Conference on Biometrics (ICB)*, 1–6.

Huang C-T, Geng T, Liu J (2023). Capturing the characteristics of mis/disinformation propagation over the internet. *Proceedings Volume 12542, Disruptive Technologies in Information Sciences VII*, 125420P.

Kadhim I, Abed FM (2023). A critical review of remote sensing approaches and deep learning techniques in archaeology. *Sensors*, 23(6), 2918.

Kenig N, Monton Echeverria J, Muntaner Vives A (2023). Human beauty according to artificial intelligence. *Plastic and Reconstructive Surgery - Global Open*, 11(7), e5153.

Keyvanfar A, Shafaghat A, Rosley MS (2022). Performance comparison analysis of 3D reconstruction modeling software in construction site visualization and mapping. *International Journal of Architectural Computing*, 20(2), 453–475.

Knell S (2022). Experimental museology: institutions, representations, users. *Museum Management and Curatorship*, 37(3), 330–332.

Ko J, Ajibefun J, Yan W (2023). Experiments on generative AI-powered parametric modeling and BIM for architectural design. *arXiv*, 2308.00227.

Lee H-H, Chang AX (2022). Understanding pure CLIP guidance for Voxel grid NeRF models. *arXiv*, 2209.15172.

Liu V, Chilton LB (2021). Design guidelines for prompt engineering text-to-image generative models. *arXiv*, 2109.06977.

Lyu Y, Wang X, Lin R, Wu J (2022). Communication in human–AI cocreation: Perceptual analysis of paintings generated by text-to-image system. *Applied Sciences*, 12(22), 11312.

Mahmoud H, Alfons R, M Reffat R (2019). Analysis of the driving forces of urban expansion in Luxor City by remote sensing monitoring. *International Journal of Integrated Engineering*, 11(6).

Maiwald F, Vietze T, Schneider D, Henze F, Münster S, Niebling F (2017). Photogrammetric analysis of historical image repositories for virtual reconstruction in the field of digital humanities. *The International Archives of the Photogrammetry, Remote Sensing and Spatial Information Sciences*, XLII-2(W3), 447–452.

Manning J (2012). Thebes (Diospolis Magna), Ptolemaic and Roman Periods, in: *The Encyclopedia of Ancient History*. Wiley.

Mazzaglia A (2021). The information system of Pompeii sustainable preservation project. A tool for the collection, management and sharing of knowledge useful for conservation and renovation of archaeological monuments. *ArcheoFOSS XIII Workshop—Open Software, Hardware, Processes, Data and Formats in Archaeological Research*, Basel, Switzerland, 14.

Meister J, Garbe P, Trappe J, Ullmann T, Es-Senussi A, Baumhauer R, Lange-Athinodorou E, El-Raouf AA (2021). The sacred waterscape of the Temple of Bastet at Ancient Bubastis, Nile Delta (Egypt). *Geosciences*, 11(9), 385.

Natampally M (2014). Reconstrucción Visual (Gráfica, Ilustrada y Digital) Del Templo Hampi. *Virtual Archaeology Review*, 5(10), 117.

Navarro-Mateu D, Carrasco O, Cortes Nieves P (2021). Color-patterns to architecture conversion through conditional generative adversarial networks. *Biomimetics*, 6(1), 16.

Nayak R, Balabantaray BK (2021). Generative adversarial network for heritage image super resolution. *Computer Vision and Image Processing*, 161–173.

Newton A, Dhole K (2023). Is AI art another industrial revolution in the making? *arXiv*, 2301.05133.

Nichol A, Dhariwal P, Ramesh A, Shyam P, Mishkin P, Sutskever I, Chen M (2021). GLIDE: towards photorealistic image generation and editing with text-guided diffusion models. *arXiv*, 2112.10741.

Oppenlaender J (2022). The creativity of text-to-image generation. *Proceedings of the 25th International Academic Mindtrek Conference*, New York, USA, 192–202.

Orengo HA, Krahtopoulou A, Garcia-Molsosa A, Palaiochoritis K, Stamati A (2015). Photogrammetric re-discovery of the hidden long-term landscapes of Western Thessaly, Central Greece. *Journal of Archaeological Science*, 64, 100–109.

Pakkeerappa P, Thomas J (2006). Strategic role of Hampi development authority in promoting tourism in Karnataka: a study. *Atna - Journal of Tourism Studies*, 1(1), 86–95.

Pan J, Li L, Yamaguchi H, Hasegawa K, Thufail FI, Tanaka S (2020). Fused 3D transparent visualization for Large-scale cultural heritage using deep learning-based monocular reconstruction. *ISPRS Annals of the Photogrammetry, Remote Sensing and Spatial Information Sciences*, 2, 989–996.

Pierrot-Deseilligny M, De Luca L, Remondino F (2011). Automated image-based procedures for accurate artifacts 3D modeling and orthoimage generation. *Geoinformatics FCE CTU*, 6, 291–299.

Pollegioni P, Woeste KE, Chiocchini F, Del Lungo S, Olimpieri I, Tortolano V, Clark J, Hemery GE, Mapelli S, Malvolti ME (2015). Ancient humans influenced the current spatial genetic structure of common walnut populations in Asia. *PLOS ONE*, 10(9), e0135980.

Powell S (2018). Etched in stone: sixteenth-century visual and material evidence of Śaiva Ascetics and Yogis in complex non-seated Āsanas at Vijayanagara. *Journal of Yoga Studies*, 1, 45–106.

Raja R, Seland EH (2022). The Paradox of Palmyra: An ancient Anomalopolis in the desert. *Journal of Urban Archaeology*, 5, 177–189.

Rajangam K, Sundar A (2021). Reading the entanglements of nature-culture conservation and development in contemporary India. *Journal of South Asian Development*, 16(1), 7–32.

Ramesh A, Dhariwal P, Nichol A, Chu C, Chen M (2022). Hierarchical text-conditional image generation with clip latents. *arXiv*, 2204.06125.

Reade JE (2002). The Ziggurrat and Temples of Nimrud. *Iraq*, 64, 135–216.

Remondino F (2011). Heritage recording and 3D modeling with photogrammetry and 3D scanning. *Remote Sensing*, 3(6), 1104–1138.

Remondino F, Rizzi A (2010). Reality-based 3D documentation of natural and cultural heritage sites–techniques, problems, and examples. *Applied Geomatics*, 2(3), 85–100.

Rihani N (2023). Interactive immersive experience: Digital technologies for reconstruction and experiencing Temple of Bel using crowdsourced images and 3D photogrammetric processes. *International Journal of Architectural Computing*, 14, 396.

Rombach R, Blattmann A, Ommer B (2022). Text-guided synthesis of artistic images with retrieval-augmented diffusion models. *arXiv*, 2207.13038.

Sbrogiò L (2022). Parametric approach to the reconstruction of timber structures in campanian Roman houses. *Virtual Archaeology Review*, 13(26), 45–61.

Scherer AK (2007). Population structure of the classic period Maya. *American Journal of Physical Anthropology*, 132(3), 367–380.

Schettino P (2016). Successful strategies for dealing with new technology in museums: a case study of immersive technology at the Immigration Museum, Melbourne. *Museum International*, 68(1–2), 130–135.

von Schwerin J, Richards-Rissetto H, Remondino F, Agugiaro G, Girardi G (2013). The MayaArch3D project: a 3D WebGIS for analyzing ancient architecture and landscapes. *Literary and Linguistic Computing*, 28(4), 736–753.

Scorrano G, Viva S, Pinotti T, Fabbri PF, Rickards O, Macciardi F (2022). Bioarchaeological and palaeogenomic portrait of two Pompeians that died during the eruption of Vesuvius in 79 AD. *Scientific Reports*, 12(1), 6468.

Senatore MR, Ciarallo A, Stanley J (2014). Pompeii damaged by volcaniclastic debris flows triggered centuries prior to the 79 A.D. Vesuvius Eruption. *Geoarchaeology*, 29(1), 1–15.

Shelach-Lavi G, Wachtel I, Golan D, Batzorig O, Amartuvshin C, Ellenblum R, Honeychurch W (2020). Medieval long-wall construction on the Mongolian Steppe during the eleventh to thirteenth centuries AD. *Antiquity*, 94(375), 724–741.

Shishido H, Ito Y, Kawamura Y, Matsui T, Morishima A, Kitahara I (2017). Proactive preservation of world heritage by crowdsourcing and 3D reconstruction technology. *IEEE International Conference on Big Data*, 4426–4428.

Soto-Martín O, Fuentes-Porto A, Martín-Gutiérrez J (2020). A digital reconstruction of a historical building and virtual reintegration of mural paintings to create an interactive and immersive experience in virtual reality. *Applied Sciences*, 10(2), 597.

Spallone R, Lamberti F, Olivieri LM, Ronco F, Castagna L (2022). AR and VR for enhancing museums' heritage through 3D reconstruction of fragmented statue and architectural context. *The International Archives of the Photogrammetry, Remote Sensing and Spatial Information Sciences*, 2(W1), 473–480.

Steinfeld K (2023). Clever little tricks: a socio-technical history of text-to-image generative models. *International Journal of Architectural Computing*, 21(2), 211–241.

Taveekitworachai P, Abdullah F, Dewantoro MF, Thawonmas R, Togelius J, Renz J (2023). ChatGPT4PCG competition: character-like level generation for science birds. *arXiv*, 2303.15662.

Toubekis G, Jansen M, Jarke M (2017). Long-term preservation of the physical remains of the destroyed Buddha figures In Bamiyan (Afghanistan) using virtual reality technologies for preparation and evaluation of restoration measures. *ISPRS Annals of the Photogrammetry, Remote Sensing and Spatial Information Sciences*, 5(W2), 271–278.

Wahbeh W, Nebiker S, Fangi G (2016). Combining public domain and professional panoramic imagery for the accurate and dense 3D reconstruction of the destroyed Bel Temple in Palmyra. *ISPRS Annals of Photogrammetry, Remote Sensing and Spatial Information Sciences*, 3(5), 81–88.

Wang X, Lasaponara R, Luo L, Chen F, Wan H, Yang R, Zhen J (2020). Digital heritage. *Manual of Digital Earth*, Singapore, 565–591.

Wotzlaw J-F, Bastian L, Guillong M, Forni F, Laurent O, Neukampf J, Sulpizio R, Chelle-Michou C, Bachmann O (2022). Garnet petrochronology reveals the lifetime and dynamics of Phonolitic Magma chambers at Somma-Vesuvius. *Science Advances*, 8(2).

Xie Y, Pan Z, Ma J, Jie L, Mei Q (2023). A prompt log analysis of text-to-image generation systems. *Proceedings of the ACM Web Conference 2023*, New York, USA, 3892–3902.

Xu Z, Wu TH, Shen Y, Wu L (2016). Three dimentional reconstruction of large cultural heritage objects based on UAV video and TLS Data. *The International Archives of the Photogrammetry Remote Sensing and Spatial Information Sciences*, XLI(B5), 985–988.

Yang M (2017). Crossing between the Great Wall of China and the "Great" Trump Wall. *Palgrave Communications*, 3(1), 25.

Zeng X, Jin T (2023). 3D Reconstruction of buildings based on transformer-MVSNet. In: Chen X and Srivastava HM (Eds.), *3rd International Conference on Applied Mathematics, Modelling, and Intelligent Computing (CAMMIC 2023)*, 191.

Zhou Y, Li P, Ye Z, Yue L, Gui L, Jiang X, Li X, Liu Y (2022). Building information modeling-based 3D reconstruction and coverage planning enabled automatic painting of interior walls using a novel painting robot in construction. *Journal of Field Robotics*, 39(8), 1178–1204.